University of Windsor
Scholarship at UWindsor

Electronic Theses and Dissertations | Theses, Dissertations, and Major Papers

2016

Design and Analysis of an Interconnected Suspension for a Small Off-road Vehicle

Zheng Yao
University of Windsor

Follow this and additional works at: https://scholar.uwindsor.ca/etd

Recommended Citation

Yao, Zheng, "Design and Analysis of an Interconnected Suspension for a Small Off-road Vehicle" (2016). *Electronic Theses and Dissertations*. 5921.
https://scholar.uwindsor.ca/etd/5921

This online database contains the full-text of PhD dissertations and Masters' theses of University of Windsor students from 1954 forward. These documents are made available for personal study and research purposes only, in accordance with the Canadian Copyright Act and the Creative Commons license—CC BY-NC-ND (Attribution, Non-Commercial, No Derivative Works). Under this license, works must always be attributed to the copyright holder (original author), cannot be used for any commercial purposes, and may not be altered. Any other use would require the permission of the copyright holder. Students may inquire about withdrawing their dissertation and/or thesis from this database. For additional inquiries, please contact the repository administrator via email (scholarship@uwindsor.ca) or by telephone at 519-253-3000ext. 3208.

DESIGN AND ANALYSIS OF AN INTERCONNECTED SUSPENSION FOR A SMALL OFF-ROAD VEHICLE

by
Zheng Yao

A Thesis
Submitted to the Faculty of Graduate Studies
through Mechanical Engineering
in Partial Fulfilment of the Requirements for
the Degree of Master of Applied Science at the
University of Windsor

Windsor, Ontario, Canada

©2016 Zheng Yao

Design and Analysis of an Interconnected Suspension for a Small Off-road Vehicle

by

Zheng Yao

APPROVED BY

Dr. Ron Barron
Department of Mathematics and Statistics

Dr. Jeff Defoe
Department of Mechanical, Automotive, & Materials Engineering

---

Dr. Bruce Minaker, Advisor
Department of Mechanical, Automotive, & Materials Engineering

October 25, 2016

Author's Declaration of Originality

I hereby certify that I am the sole author of this thesis and that no part of this thesis has been published or submitted for publication.

I certify that, to the best of my knowledge, my thesis does not infringe upon anyone's copyright nor violate any proprietary rights and that any ideas, techniques, quotations, or any other material from the work of other people included in my thesis, published or otherwise, are fully acknowledged in accordance with the standard referencing practices. Furthermore, to the extent that I have included copyrighted material that surpasses the bounds of fair dealing within the meaning of the Canada Copyright Act, I certify that I have obtained a written permission from the copyright owner(s) to include such material(s) in my thesis and have included copies of such copyright clearances to my appendix.

I declare that this is a true copy of my thesis, including any final revisions, as approved by my thesis committee and the Graduate Studies office, and that this thesis has not been submitted for a higher degree to any other University or Institution.

Abstract

The suspension is an indispensable component of a vehicle that must be carefully designed to ensure good vehicle handling and safety. Over the years, many different kinds of suspension have been applied on vehicles. This thesis aims to develop a stable, comfortable and safe suspension for the University of Windsor SAE Baja off-road vehicle that improves performance by using an innovative interconnection in the suspension. A mechanism that connects the front and rear suspension on each side of the vehicle is mounted on the chassis. A virtual vehicle is designed in CATIA and a dynamic simulation is conducted using the software tools EoM and Altair Motionview®. Multiple randomly generated ISO class road profiles are used to excite the motion of the model. Several virtual sensors are installed in different positions of the vehicle to record motions of interest. MATLAB® is used to analyze the outputs of the simulation. Results obtained from the model show that the interconnected suspension does provide reduced roll motion with less comfort penalty when compared to an anti-roll bar system, with advantages primarily showing in the low frequency domain, suggesting that the suspension is more appropriate to an off-road vehicle. However, the merit of the proposed design is below expecations, suggesting that further study of alternate designs is warranted.

To my parents,
for their marvelous love and support.

Acknowledgements

Though only my name appears on the cover of this thesis, many people have given me support and made this work possible. My MSc career has been a valuable experience that I will cherish and remember forever. I can hardly thank all those people enough for their contributions and advice. I would never have thought it would be such a difficult and long journey.

First of all, my deepest gratitude to my advisor Dr. B.P. Minaker, for his excellent erudition, altruism and patience. I am amazingly fortunate to have an advisor who gave me the freedom to explore. Under his instruction, my insight was not limited to my own major, but also broadened to other areas that could be helpful to improve my entire accomplishment. His patience and guidance helped me to overcome many obstacles in our two years together. There is no doubt it was a fantastic experience working with him.

I would also like to thank my parents, and my wife Fang; they are always supporting and encouraging me to go further in the way I choose.

Moreover, I would like to express my appreciation to all my friends, for sharing both bliss and misfortune together. Without you, I would not have finished my degree so smoothly.

Contents

List of Tables

List of Figures

List of Abbreviations

All abbreviations used in this work are described in this section.

Abbreviations

Abbreviation	Meaning
CAE	Computer Aided Engineering
DAE	Differential Algebraic Equation
DOF	Degree of Freedom
EOM	Equation of Motion
FFT	Fast Fourier Transform
FHWA	United States Federal Highway Administration
GUI	Graphic User Interface
HIS	Hydraulic Interconnected Suspension
IRI	International Roughness Index
ISO	International Standard Organization
MATLAB®	Matrix Laboratory software
NCHRP	United States National Cooperative Highway Research Program
ODE	Ordinary Differential Equation
PSD	Power Spectral Density
SAE	Society of Automotive Engineers
VRML	Virtual Reality Modeling Language

Nomenclature

Mathematical notation throughout this work is listed below, separated by the chapter in which it first appears.

Background Review

Label	Description
A	Coefficient of road roughness
A_{a}	Area Matrix
A_{i}	Amplitude of sinusoidal wave
$B(C_{\mathrm{xyz}})$	Vehicle coordinate frame
B^T	Orthogonal Matrix
B_{h}	Holonomic constraint Jacobian matrix
B_{nh}	Nonholonomic constraint Jacobian matrix
b_{l}	Horizontal distance between vehicle mass center and left strut
b_{r}	Horizontal distance between vehicle mass center and right strut
C	Damping matrix
C_{u}	Degree of unevenness
C_{s}	Damping matrix of sprung mass
c_{ix}, c_{iy} and c_{iz}	Damping coefficient of ith damper along x, y, z direction,respectively
D_1	Linear transformation matrix
F	Applied force vector
F_{x}, F_{y} and F_{z}	Longitudinal, lateral and normal force, respectively
f	Force between wheel and ground
f_{a}	Actuator force
f_{c}	Constraint force
f_{h}	Absorber force
f_{x}	External force
G	Ramp gradient

$G(C_{XYZ})$	Ground coordinate frame
H	Ramp height
$hav(\theta)$	Angle of haversine ramp
I	Moment of inertia
K	Stiffness matrix
K_s, K_u	Stiffness matrix of spring and unsprung mass, respectively
k_{ix}, k_{iy}, k_{iz}	Spring stiffness of ith spring along x, y, z direction, respectively
L	Ramp length
l	Length of spring
M	Mass matrix
M_x, M_y, M_z	Roll moment, pitch moment and yaw moment, respectively
n	Angular spatial frequency
n_{SR}	Spatial frequency
P	Pressure vector
p, q, r	Roll rate, yaw rate and pitch rate, respectively
p_c	Compressive force in the spring
p_x	The global location and small angle orientations
R_{xx}	Autocorrelation function of random road signal
S_{xx}	Power spectral density of autocorrelation function of random road signal
S_y	Power spectral density of excitation
V	Longitudinal speed of vehicle
X	Displacement vector
X_s and X_u	Sprung mass and unsprung mass displacement, respectively
x_d	Deflection of the suspension
x	Center of mass
Y	Displacement vector
Y_t	Excitation
Z	Displacement along z direction
Z_R	Road profile signal
ψ, ϕ, θ	Yaw angle, roll angle and pitch angle, respectively
θ_R	Ramp angle
ω	Radial spatial frequency
ω_x	Angular velocity around x-axis
ω_y	Angular velocity around y-axis

ω_z	Angular velocity around z-axis
λ_R	wave length
Φ	Spatial frequency
Φ_i	Phase angle
$\Phi(n)$	Power spectral density based on the spatial frequency
$\Phi(\Omega)$	Power spectral density based on the angular spatial frequency
Ψ	Road input power spectral density
σ	Road roughness variance
ω_0	Fundamental temporal frequency

Vehicle Dynamic Modeling

Label	Description
F_{sij}	Spring force in ijth spring
F_{dij}	Damping force in ijth damper
I_α, I_β	Moment of interia about the x axis and y axis, respectively
m	Sprung mass
m_{ij}	Unsprung mass in the ijth location
x_d	Deflection of the suspension
z	Displacement

Simulation Results

Label	Description
a	Real part of eigenvalues
b	Imaginary part of eigenvalues
C	Damping matrix
F_0	Mean value of samples
K	Stiffness matrix
M_{sy}	Mass of system
N	Number of data samples

s	Laplace variable (complex)
t	Time
$u(t)$	Step signal
y	Logarithmic number
α	Polar coordinate
β	Cartesian coordinate
ζ	Damping ratio
σ_{sd}	Standard deviation
ϕ_{s}	Phase of sinusoidal signal
ω_{n}	Natural frequency
ω_{d}	Damped natural frequency

Chapter 1

Introduction

Since the Benz Velo, the world's first production car, came off the assembly line, the driving safety problem has been an ongoing concern. The suspension system, working to isolate the vehicle from rough road profiles, is no doubt a necessary component. Furthermore, the demands on the suspension of a racing vehicle are more strict; not only does it have to provide a comfortable driving condition, it should also improve the handling. This thesis aims to develop an innovative interconnected suspension to improve the performance of an off-road racing car.

In this chapter, the motivation, objective and structure of this thesis are described.

1.1 Motivation

In recent times, the number and variety of vehicles available is growing rapidly with technological advancement. Methods to improve vehicle quality and driving safety, to some extent, have become an important topic in our society. As an indispensable part in the vehicle, the suspension is not only supposed to isolate drivers from rough road conditions such as bumping and vibration, but should also provide good handling and braking performance for driving safety.

The conventional vehicle suspension system is primarily composed of a mechanical coil spring and hydraulic damper. Also, an anti-roll bar, commonly known as the sway bar, is a torsional spring that may be added between the right and left side of the front axle, or the rear axle, or both axles. While the conventional suspension provides a satisfactory solution, the interconnected suspension offers a potential performance improvement.

Unlike a conventional suspension, an interconnected suspension can help the vehicle distribute the normal load on the tires more evenly on rough roads without losing grip. Many different kinds of interconnected suspensions, e.g. mechanical, hydraulic and pneumatic, have been proposed. Among them, the mechanical type is utilized in this project because of its low cost and simplicity. While mechanical coupling may not prove practical on a

normal full-size passenger car, the small size of the target vehicle, an SAE Baja car, makes it a good choice.

1.2 Research Objectives

The first objective is to design and develop an interconnected suspension system for the vehicle. A CATIA model based on the 2013 UWindsor SAE Baja car is used, and an interconnection mechanism is added on both sides of the vehicle, to determine if the physical size and space constraints in the vehicle make a mechanical interconnection possible.

The second objective is to build a model in EoM, a software package that uses a description of a mechanical multibody system to generate its linearized equations of motion. Virtual sensors are mounted on the front part of the vehicle to measure the pitch-bounce-roll motions. A linear simulation is conducted using this model; resulting motions can also be visualized through animations.

The third objective is to develop a more complex model in Altair MotionView®. Both linear and nonlinear MotionView® simulation results are compared with those from EoM. Also, a random road profile is applied in the model to simulate severe loading.

The last objective is to compare the properties and simulation results of a conventional suspension, a suspension with an anti-roll bar, and an interconnected suspension. Advantages and disadvantages are identified.

1.3 Thesis Structure

This thesis proposes a innovative mechanical interconnected suspension design to potentially improve ride quality and handling performance. In this section, brief descriptions of each chapter will be given, to help in understanding the structure of the thesis.

Chapter 2 provides a brief background review of the literature relevant to the goal of this research. In this chapter, different kinds of interconnected suspensions are described, defined, and classified. The definitions of road profiles are given; the concepts of the fast Fourier transform and power spectral density are introduced as well. The ISO classifications of random road profiles, based on the power spectral density, are described. At last, two important vehicle coordinate systems are described. The equations of motion based on different vehicle models with varying numbers of degrees of freedom vehicle are listed.

Chapter 3 introduces a full-vehicle model and concretely describes the mechanical and dynamic structure of the model used in the different software tools. The differential-algebraic equation solver of Altair MotionView® is discussed.

Chapter 4 summarizes the results of both the linear and non-linear simulations of the Baja car model. The eigenvalues produced from EoM are listed. A sinusoidal road profile is applied on the right front wheel of the full-vehicle model. The steady state transfer function results are generated in EoM. The results of the modal analysis, the frequency response analysis, and the steady state gains are obtained from the linear model in EoM. Step and sinusoidal signals are applied on all vehicle configurations in Altair MotionView® to confirm the linear steady state gains and frequency response. Additionally, a small pertubation is applied on the right front wheel and the time history solutions from the linear and non-linear model are compared. Finally, different levels of random road are taken into consideration to test the performance of the different configurations of the vehicle. The standard deviation and mean value of the tire normal force are utilized to compare the three vehicle configurations.

Chapter 5 summarizes the work that has been done in this research, and draws some conclusions on the effectiveness of the interconnected suspension. Recommendations and suggested future work are also included.

Chapter 2

Background

2.1 Definition of Interconnected Suspension

The suspension is the system of springs, dampers and linkages that connects a vehicle to its wheels and allows relative motion between the two[?]. Any suspension system where displacements at one wheel station can give rise to forces at other wheel stations can be described as an *interconnected* suspension[?]. Similar to a conventional suspension, the purpose of the interconnected suspension is to improve the vehicle handling for safety and driving pleasure, and also to insulate the vehicle from road bumps and vibration, to provide the passengers with a comfortable ride. A suspension system with an anti-roll bar, as shown in Figure 2.1, is the most common and simple interconnected suspension. The anti-roll bar works as a torsional spring and is located underneath the chassis and mounted to the chassis by bushings. It is most commonly mounted to the front suspension, as this contributes to vehicle yaw stability.

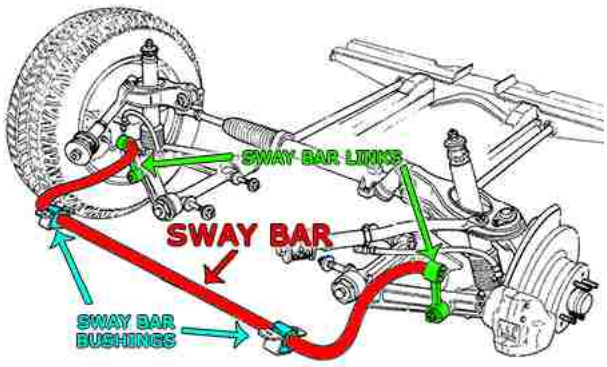

Figure 2.1: Anti-roll bar (reproduced from http://rareparts.com)

When a vehicle is cornering to the left and so leaning to the right, the left wheel suspensions will go into extension, or even lift the wheel from the ground, which in turn can cause the vehicle lose grip and control. The

anti-roll bar, working as a torsional spring, reduces the relative motion of the left and right wheels, to help prevent the roll-over phenomenon. As a result, the anti-roll bar increases the vehicle roll stiffness, but does so without any change in the bounce stiffness. Other more complex variations of the interconnected suspension can be divided into three classifications: mechanical (the anti-roll bar is an example), hydraulic, and pneumatic systems.

2.2 Classification of Interconnected Suspensions

2.2.1 Mechanical Interconnected Suspension

The Citroën 2CV, mass-produced from 1948 to 1990, was one of the few passenger cars employing front to rear mechanically interconnected suspensions[**?**]. As illustrated in Figure 2.2, a suspension cylinder C, including two springs B and D, are mounted on each side of the chassis in this system. This mechanism is connected by pull-rods to the front leading swinging arm A and the rear trailing swinging arm E, which act like bell-cranks. Through connections to spring seating cups in the middle of the cylinder, each spring can be compressed against the ends of the cylinder independently. The cylinder itself is also spring mounted to the chassis, allowing loads from one suspension to be transferred to the other. The long travel distance of the coil spring leads to softness of the suspension.

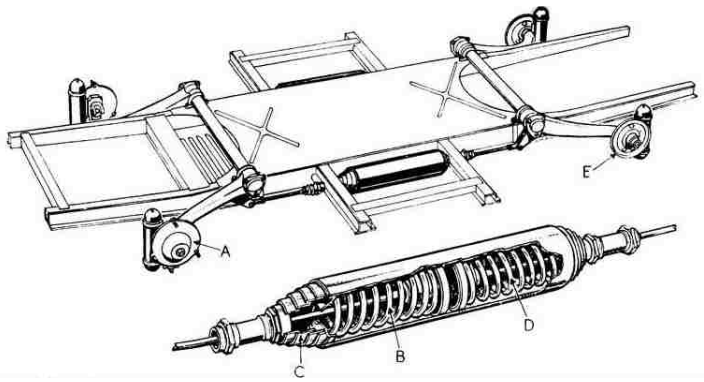

Figure 2.2: Interconnected suspension of the Citroën 2CV (reproduced from Edgar[**?**])

In 1968, an interconnected suspension using a rear trailing arm was invented by William Allison[**?**]. Figure 2.3 is a top view of a vehicle with this suspension in accordance with the design. The vehicle body is supported by a conventional independent suspension (14) and (16), while left and right torsion bars (22) and (24), fixed by mounting brackets (30) and (32), are employed to connected the chassis and front wheels together. At the rear of the vehicle, U-bolts (56) clamp the rear axle (36) to the trailing arm and a balancing lever is mounted on the trailing arm with an angle to the transverse line; this angle prevents wheels slipping caused by the unequal traction during accelerations.

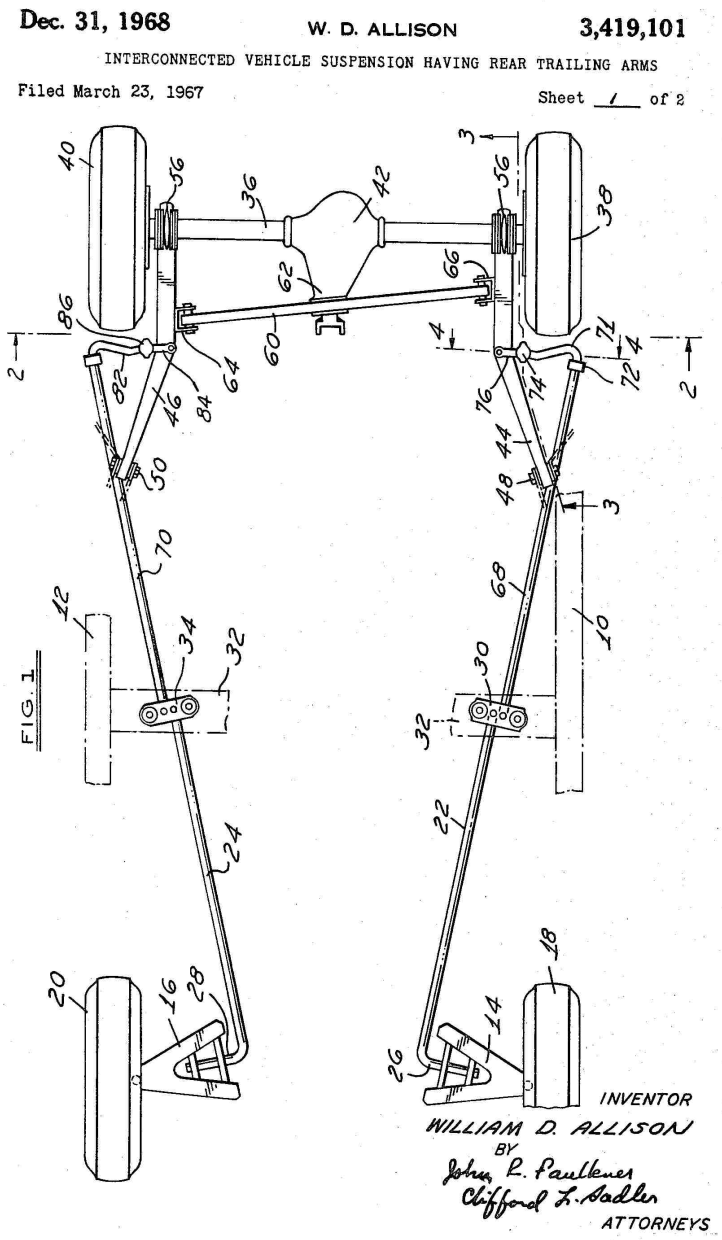

Figure 2.3: Allison's Interconnected suspension (reproduced from Allison[?])

2.2.2 Hydraulic Interconnected Suspension (HIS)

In the 1920s, Hawley illustrated a possible interconnected suspension consisting of four double-acting cylinders interconnected hydraulically[?]. The objective of this design was to improve the ride quality of the vehicle by absorbing the energy of road shocks. As shown in Figure 2.4, four identical shock absorbers are mounted on the vehicle, where the piston rod (17) is connected to the piston (15). When the vehicle goes over a bump or obstacle, the piston rod, connected to the wheel and moving in the bath of oil (19), changes the volume of air (20) in the upper portion of each plunger, so as to buffer the vertical motion of the vehicle with the help of the air pressure. The system allows the pressure applied on one corner to be distributed on the four wheels evenly.

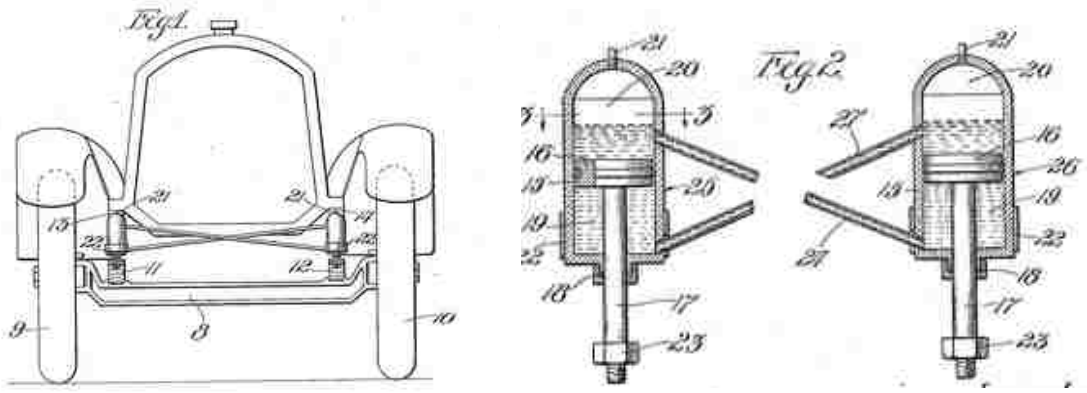

Figure 2.4: Shock absorber of Hawley's interconnected suspension (reproduced from Hawley[?])

In 2002, Fontdecaba proposed a novel four-wheel interconnected suspension model shown in Figure 2.5[?]. Fontdecaba's model had a central unit, but the components in the central unit were not illustrated explicitly. In addition, each wheel had its own spring and damper. The purpose of the central unit was to allow the reduction of the stiffness and damping of the individual wheel stations. Unfortunately, no attempt to build a theoretical model or to predict the behaviour was realized.

In 2000, a theoretical interconnected suspension model was presented by Erik Zapletal[?]. Based on a decoupled roll-bounce-pitch-twist dynamic model, Zapletal believed that this interconnected suspension could provide enough stiffness to resist the height variation, and pitch and roll attitude, but also be compliant enough to adapt to the twisting and undulations of the ground. The structure of this system is shown in Figure 2.6. Instead of an anti-roll bar installed in the front part of the vehicle body, a balance mechanism is located in the rear. The connections between front suspensions and balance mechanism 'cross over', meaning the left wheel is connected to the right corner of the balance mechanism, and vice versa.

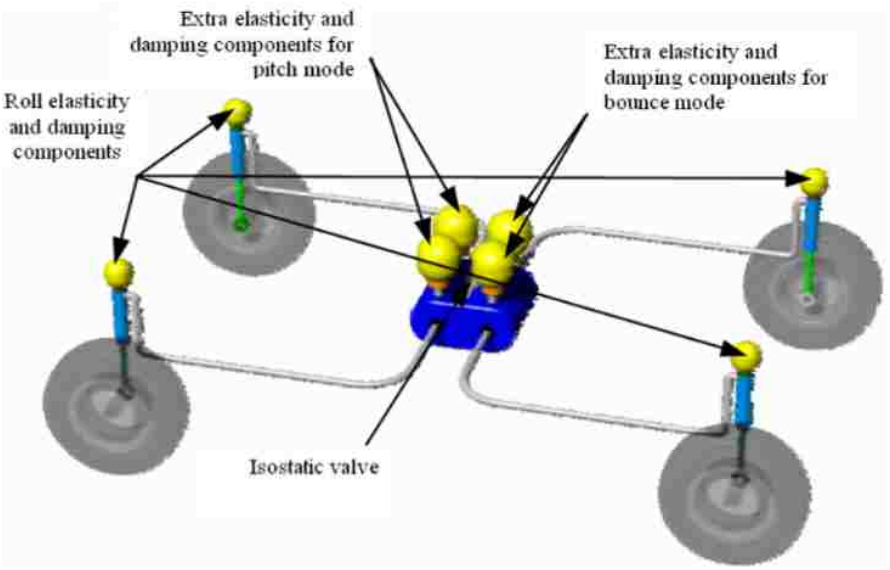

Figure 2.5: Fontdecaba's interconnected suspension (reproduced from Smith[**?**])

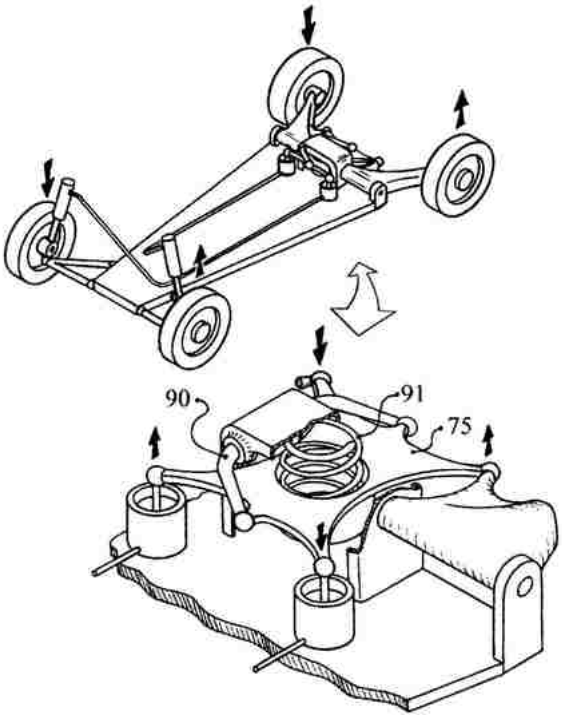

Figure 2.6: Zapletal's balanced suspension (reproduced from Zapletal[**?**])

In 2013, an hydraulic interconnected suspension concept was presented by Lifu Wang et al[**?**]. As illustrated in Figure 2.7, the conventional suspension is replaced by an interconnected fluid circuit around the vehicle; there

is an hydraulic chamber including a piston and cylinder on each corner. As the road profile causes the motion of the actuators, the pressure of the fluid that flows in the entire circuit leads to the motion of the pistons in the cylinders, and distributes the disturbance over all four wheels, to keep the vehicle stable and balanced. Based on the roll angle comparison, Wang et al prove that an HIS can provide larger roll stiffness to the vehicle body than an anti-roll bar with equivalent ride quality.

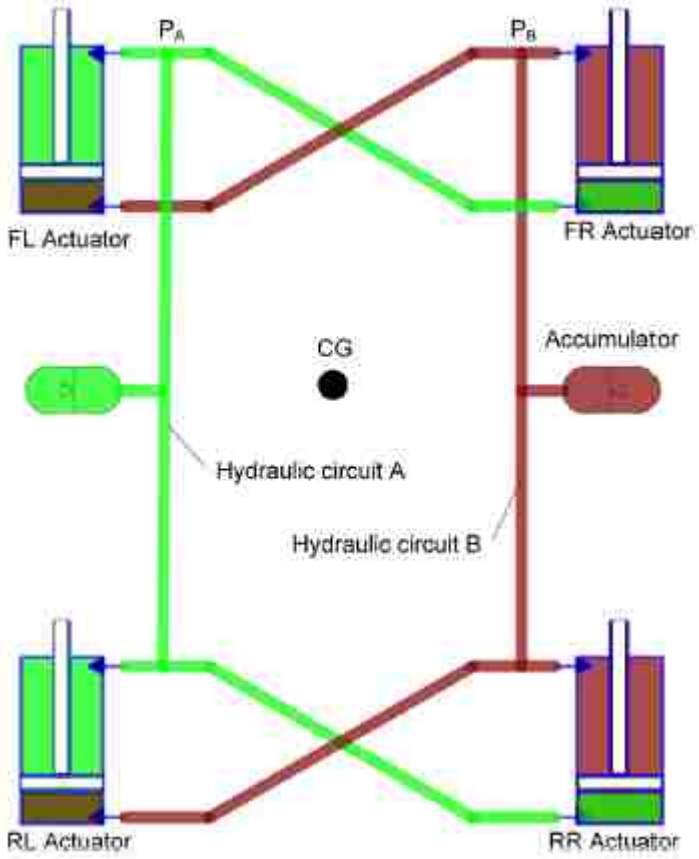

Figure 2.7: Schematic diagram of the HIS system (reproduced from Wang et al[?])

Another innovative hydraulic interconnected suspension was developed by Mavroudakis[?]. In his opinion, a holistic and comprehensive approach was supposed to be considered instead of addressing each corner independently. Mavroudakis proposed that various loading cases could be thought of as mode excitation, such as: the vertical accelerations excite the bounce mode, longitudinal accelerations excite the pitch mode and lateral accelerations excite the rolling mode. Road excitation such as bumps could be considered as combinations of different modes. To evaluate this idea, a simple model was built. As illustrated in Figure 2.8, four hydraulic rams were utilized to replace the conventional spring/damping elements. The four rams are connected to the main unit through an appropriate interconnection. In the central unit, there are four cylinders that are responsible for the twist-roll-pitch-bounce modes. Based on the analysis, it is clear that this decoupling approach is better than the

conventional suspension system. This HIS can provide a comfortable ride condition with soft bounce stiffness without sacrificing safety, which is determined by sufficient pitch and rolling stiffness.

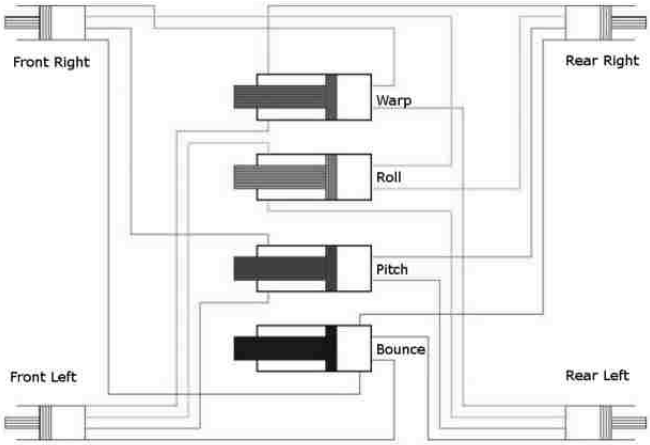

Figure 2.8: Hydraulic scheme of central unit (reproduced from Mavroudakis[?])

In 2009, Zhang et al[?] proposed a method to analyze the frequency response of a vehicle with an hydraulic interconnected suspension system. A 4-degree-of-freedom half-car model was used to illustrate this methodology. The right half of Figure 2.9 shows a conventional suspension system that consists of linear tyre damping/spring and suspension spring/damping, while the left one is an hydraulic suspension system that includes double-acting hydraulic cylinders. The resulting equation of motion is a second order linear differential equation (Equation 2.1):

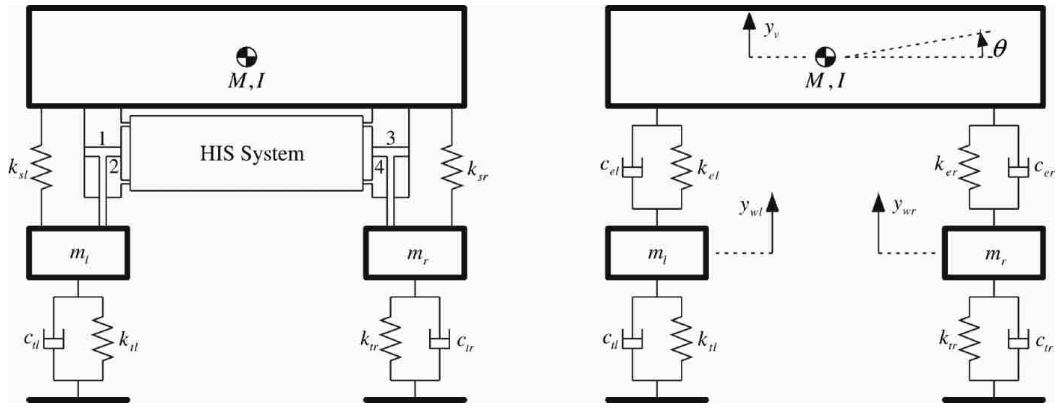

Figure 2.9: Schematic of a half-car with an HIS and a conventional independent suspension (reproduced from Zhang et al[?])

$$M\ddot{y} + C\dot{y} + Ky = f(t) \tag{2.1}$$

where the displacement vector consists of both wheel motions, and the chassis motion and roll angle: $y = \begin{bmatrix} y_{\mathrm{wl}} & y_{\mathrm{wr}} & y & \theta \end{bmatrix}^T$. The mechanism coupling the conventional suspension and fluid systems is treated as a

double-acting piston and cylinder. The applied forces $f(t)$ consists of the applied force caused by hydraulic pressure and other external forces f_{ex}, so it can be written as $f(t) = DAp(t) + f_{ex}(t)$, where p is a pressure vector and A_a is an area matrix. The matrix D is a linear transformation.

$$D_1 = \begin{bmatrix} -1 & 1 & 0 & 0 \\ 0 & 0 & -1 & 1 \\ 1 & -1 & 1 & -1 \\ -b_l & b_l & b_r & -b_r \end{bmatrix} \tag{2.2}$$

The values b_1 and b_r are the horizontal distances between the vehicle mass center and suspension struts in the left and right sides. The resulting equation of motion is given in Equation 2.3.

$$M\ddot{y} + C\dot{y} + Ky = D_1 Ap(t) + f_x(t) \tag{2.3}$$

The result of this analysis is the claim that interconnected suspensions offer much greater flexibility to independently specify model stiffness and damping parameters than conventional suspensions.

2.2.3 Hydro-pneumatic Interconnected Suspension

A hydro-pneumatic interconnected suspension concept was developed by Cao et al[**?**] in 2010. Two schematics of the hydro-pneumatic strut design are shown in Figure 2.10. The proposed single gas chamber strut (A) is illustrated in Figure 2.10(a); the gas chamber and damping valve are contained within the same unit to contribute to a compact design. The chambers (2) and (4) are separated by a piston; the fluid in chambers (1), (2), and (3) can flow through the orifices. Figure 2.10(b) presents the schematic of the proposed two gas chamber strut (B), which includes two gas chambers. The difference from the single gas chamber strut, is that the oil in chamber (3) is replaced by gas; only oil in chambers (1) and (2) is allowed to flow through the orifice. Using hydraulic, pneumatic and hydro-pneumatic connections, many different configurations are possible, through different linkages of struts A and B. Figure 2.11 shows a possible X-coupling interconnected suspension configuration among the four strut units, connected by hydraulic oil lines. The authors claim that based on the analysis, the simulation results show that this X-coupled interconnected suspension can increase roll and pitch stiffness without influence on bounce and twist performance, so this hydro-pneumatic suspension can offer better driving conditions and controllability.

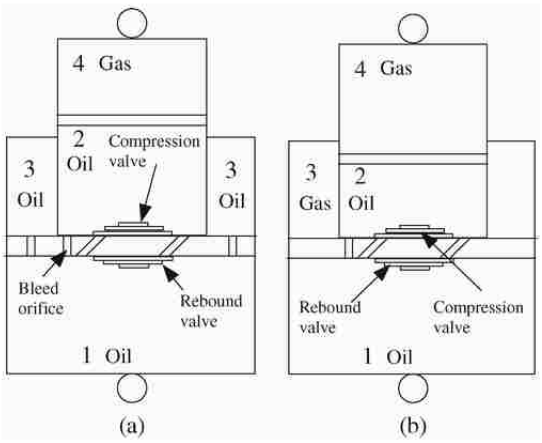

Figure 2.10: Strut units A and B of hydro-pneumatic interconnected suspension (reproduced from Cao et al[**?**])

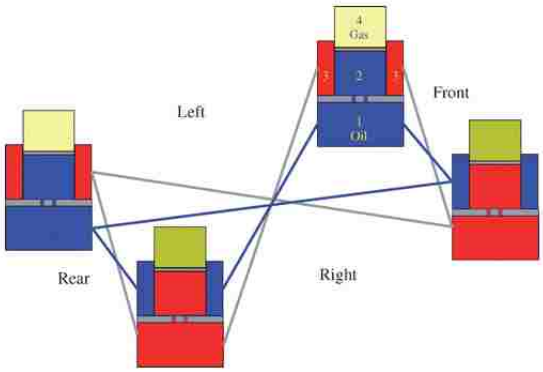

Figure 2.11: Hydro-pneumatic coupling (reproduced from Cao et al[**?**])

In 1979, a hydro-pneumatic suspension, referred to as a 'Hydragas' suspension, was developed by Moulton[**?**], to improve ride quality. In this system, nitrogen gas works as the spring medium and hydraulic fluid pressure provides damping. The damping fluid chambers of the front and rear wheels on each axle of the car are connected via a hydraulic line. When an input at the front wheel pumps fluid through the line to the rear wheel, the increasing fluid pressure produces an upward force on the sprung mass, so the difference in the suspension forces can be reduced in this way. Figure 2.12 is a cutaway of the Hydragas suspension, showing that when the piston has an upward motion, the area of the diaphragm against which the fluid pressure acts will vary with suspension travel. Figure 2.13 A shows the corresponding response of the Hydragas system to pitching motion, the front wheel is lifted relative to the vehicle body first, while the back wheel goes the opposite direction. Because of the upward motion of the front wheel, the diaphragm goes up and the fluid flows from the front to the rear units. As a result, the pitch stiffness is lower than it would be without the interconnected suspension. Figure 2.13 B shows the corresponding response of the Hydragas system to a bounce motion. In this solution, the fluid does not

flow through the lines, but rather only between the upper and lower chamber of the individual units through the damper valves. The high fluid pressure and increasing piston area leads to high bounce stiffness.

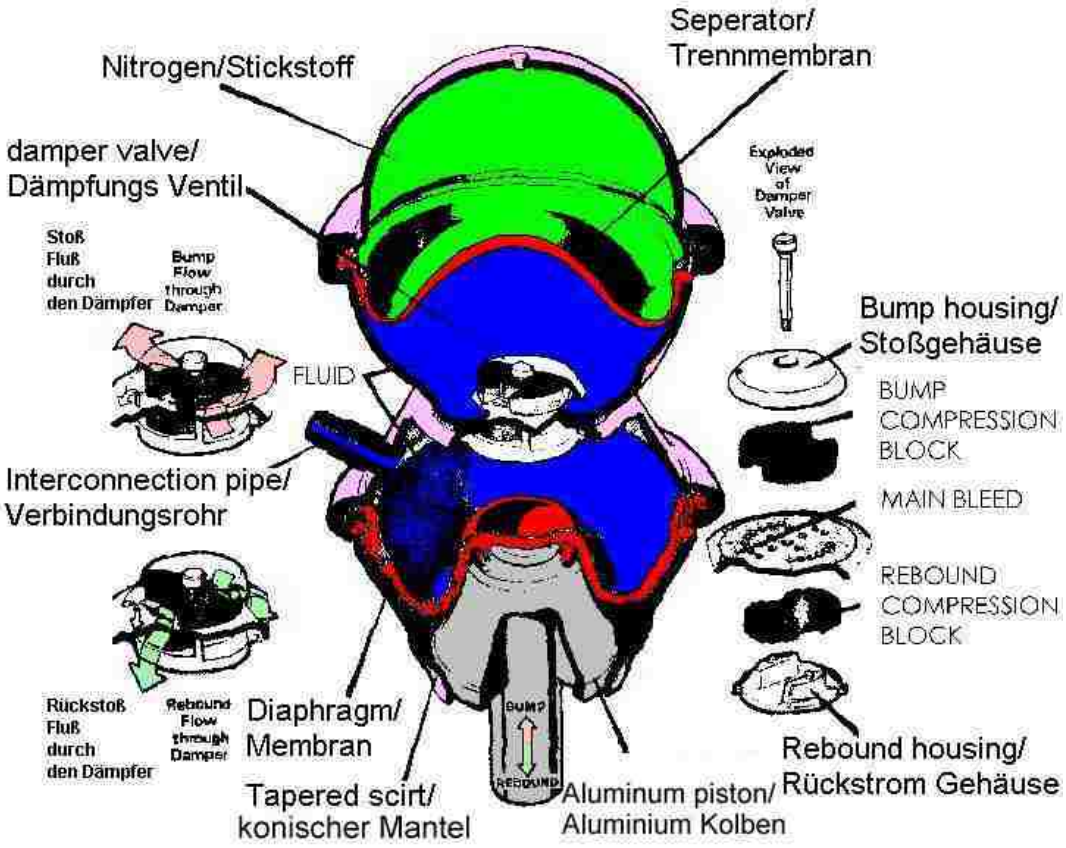

Figure 2.12: Cutaway of Hydragas suspension unit (reproduced from Moulton[?])

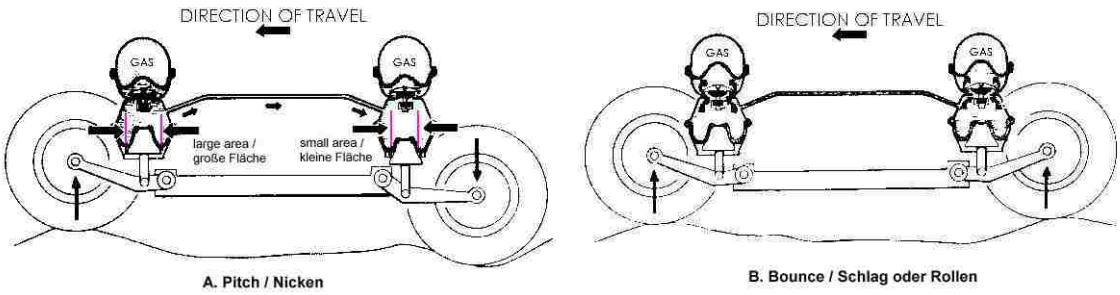

Figure 2.13: Moulton's hydro-pneumatic coupling (reproduced from Moulton[?])

2.3 Relationship with Current Work

There have been several kinds of interconnected suspensions proposed in the past, and most claim to offer improved performance. However, the method evaluated in the current work is novel. It uses an all mechanical implementation for the sake of simplicity and cost, rather than a hydraulic system. In addition, the proposed system has no influence on bounce or pitch stiffness, but aims to increase roll stiffness without the corresponding increase in twist stiffness that accompanies traditional anti-roll bars. According to Zapletal[**?**], roll stiffness is necessary to prevent excessive body motions during cornering, but twist motion of the suspension can only occur on uneven road surfaces, and so high twist stiffness only contributes to uneven tire loads, and is generally not desirable. The suspension displacement modes are illustrated in Figure 2.14.

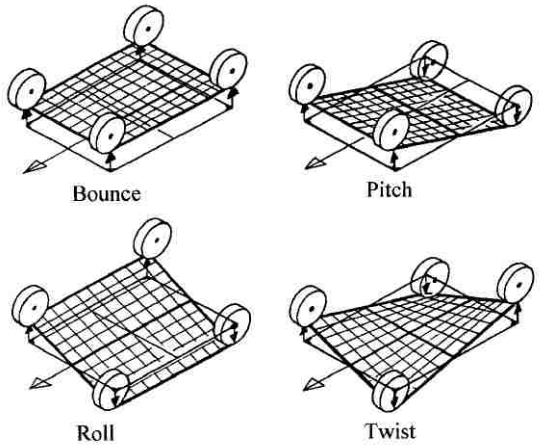

Figure 2.14: Suspension displacement modes (reproduced from Zapletal[**?**])

2.4 Road Profile

2.4.1 Definition of Road Profile

The road profile is a two-dimensional section of the road surface. There are two kinds of sections possible, along perpendicular axes. The first one is a lateral section, showing the superelevation and crown of road design, plus bumps and other undulations. The other is a longitudinal section, showing the design grade, roughness, and texture. In this thesis, the focus is on longitudinal profiles. Information on measuring road profiles can be found in Sayer and Karamihas[**?**]. Any particular track along a road has a longitudinal profile. In this project, two parallel tracks are considered, i.e., road profiles of different phases are applied on the wheels, and at the same time, the cornering condition is neglected. The roads can be classified into several types.

Isolated ramp

A disturbance with a residual change of road height can be categorized as a ramp, three types are shown in Figure 2.15. The first type is a simple ramp, where the transition between the different heights is almost vertical; it is used to simulate a curb. If a vehicle goes over a simple step at high speed, a severe shock is caused to the suspension system. The true linear ramp is a softened version of the step and can be specified by the height H and length L; the gradient of the ramp is described as $G = \frac{H}{L}$, and the ramp angle is $\theta_R = \tan^{-1}(H/L)$. The haversine ramp is the most smoothed version, and can be defined as:

$$\text{hav}(\theta) = \frac{1}{2}(1 - \cos\theta) \tag{2.4}$$

The haversine ramp has a sinusoidal profile from $\text{hav}(2N\pi) = 0$ to $\text{hav}((2N-1)\pi) = 1$, where N is an integer.

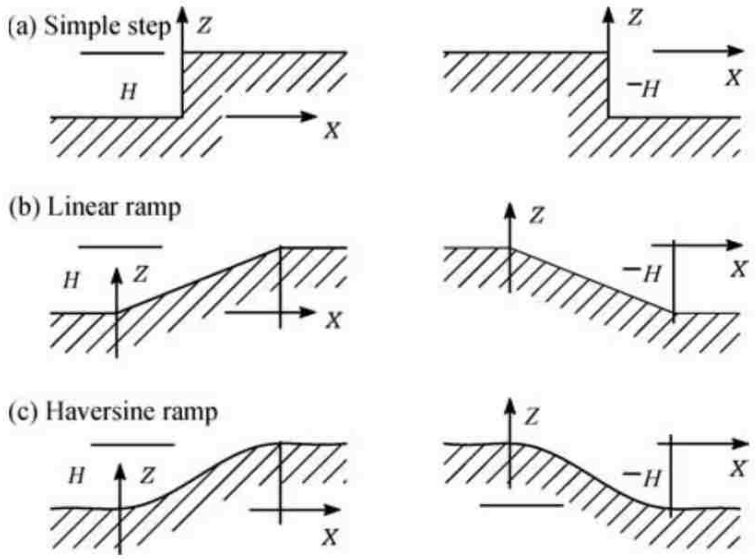

Figure 2.15: Types of isolated ramps (reproduced from Dixon[?])

Isolated bumps

Different from ramps, many different isolated bumps can also be used to simulate a road excitation. Several types are shown in Figure 2.16 .

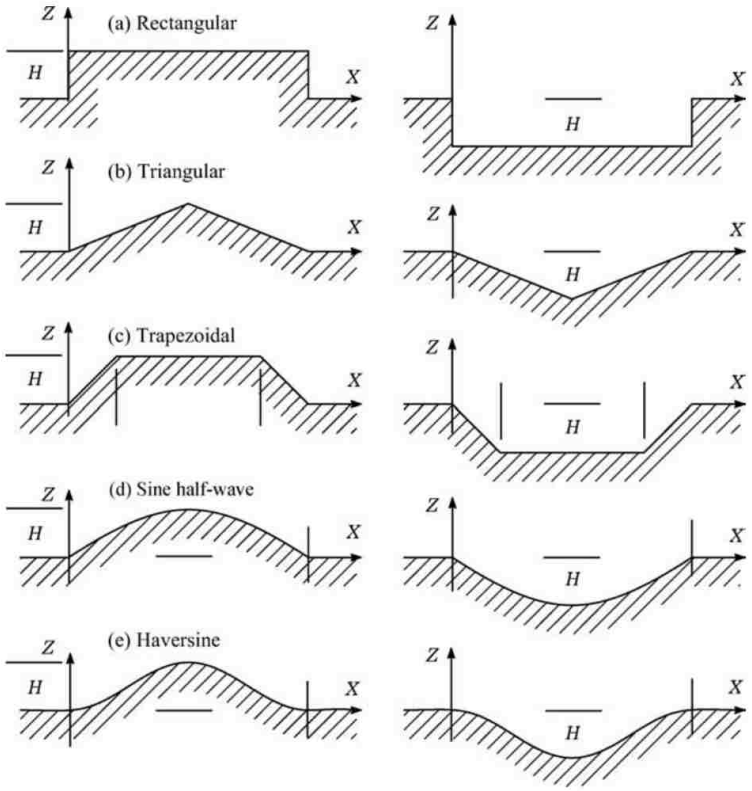

Figure 2.16: Types of isolated bumps (reproduced from Dixon[?])

Sinusoidal single path

The sinusoidal single path shown in Figure 2.17 has just one spatial frequency. It is known as a single-track, and is one with the operating width of a single vehicle[?]. The spatial frequency of the road n_{SR}, given in cycles per meter, and the radian spatial frequency of the road ω_{SR} in radians per meter are defined in Equations 2.5 and 2.6.

$$\omega_{SR} = 2\pi n_{SR} = \frac{2\pi}{\lambda_R} \tag{2.5}$$

$$n_{SR} = \frac{1}{\lambda} \tag{2.6}$$

where λ_R is a given wave length. The amplitude Z can be defined as:

$$Z = S\sin(\omega_{SR}X) + C\cos(\omega_{SR}X) \tag{2.7}$$

where S and C are the coefficients of the sinusoidal curves.

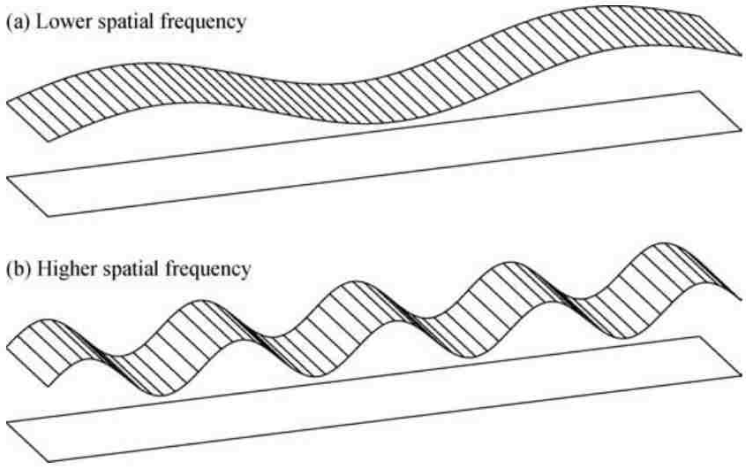

Figure 2.17: Types of isolated sinusoidal single path (reproduced from Dixon[?])

2.4.2 Power Spectral Density (PSD) and Fast Fourier Transform (FFT)

In engineering, sometimes signals need to be transferred from the time domain to the frequency domain with the fast Fourier transform (FFT). In the frequency domain, the features of the signal can be analyzed more clearly and comprehensively than in the time history. In some circumstances such as the measurement of energy of signals, the FFT can be replaced with the power spectral density (PSD), which describes the density of power in a random process. With the PSD, the strength of the variation of signals can be characterized. According to Davis[?], the PSD can be expressed as the Fourier transform of R_{xx}:

$$S_{ss}(f) = \int_{-\infty}^{\infty} R_{xx}(\tau) e^{j2\pi f \tau} d\tau \tag{2.8}$$

where f is the frequency variable in Hz (S_{ss} has units of m^2/Hz), and $R_{xx}(\tau)$ is the autocorrelation function of a random signal $x(t)$ in the time domain:

$$R_{xx}(\tau) = \langle x(t)x(t-\tau)\rangle = \lim_{T\to\infty} \frac{1}{T} \int_0^T x(t)x(t-\tau)dt \tag{2.9}$$

In this thesis, vertical displacements in the time domain from a random road surface profile are applied to the wheels of the vehicle model. The response curves of the different components are transferred into the frequency domain and the PSD is computed. The plot is produced with MATLAB® to analyze the driving performance; the MATLAB® code is attached in Appendix A.2.

2.4.3 Road Profile Classification in ISO 8086

To comprehensively specify a road condition, standards have been defined to classify a random road profile. In this thesis, the International Standards Organization (ISO) classification is utilized to produce the random road profile.

The ISO 8608 standard uses the PSD value to characterize the road profile. The PSD represents the magnitudes of a series of sinusoidal road profiles with different wave numbers. In Figure 2.18, the plot is defined as:

- 1 and 3 express power spectral density based on spatial frequency, $\Phi(n)$ [m^3/cycle] and angular spatial frequency, $\Phi(\Omega)$ [m^3/rad], respectively
- 4 and 5 are the spatial frequency, Ω [cycle/m] and angular spatial frequency, n [rad/m], respectively
- 2 is the wavelength with the unit λ [m].
- Letters A to H are the levels of random roads, where A is smooth road in new condition, and H is extremely poor, off-road conditions.

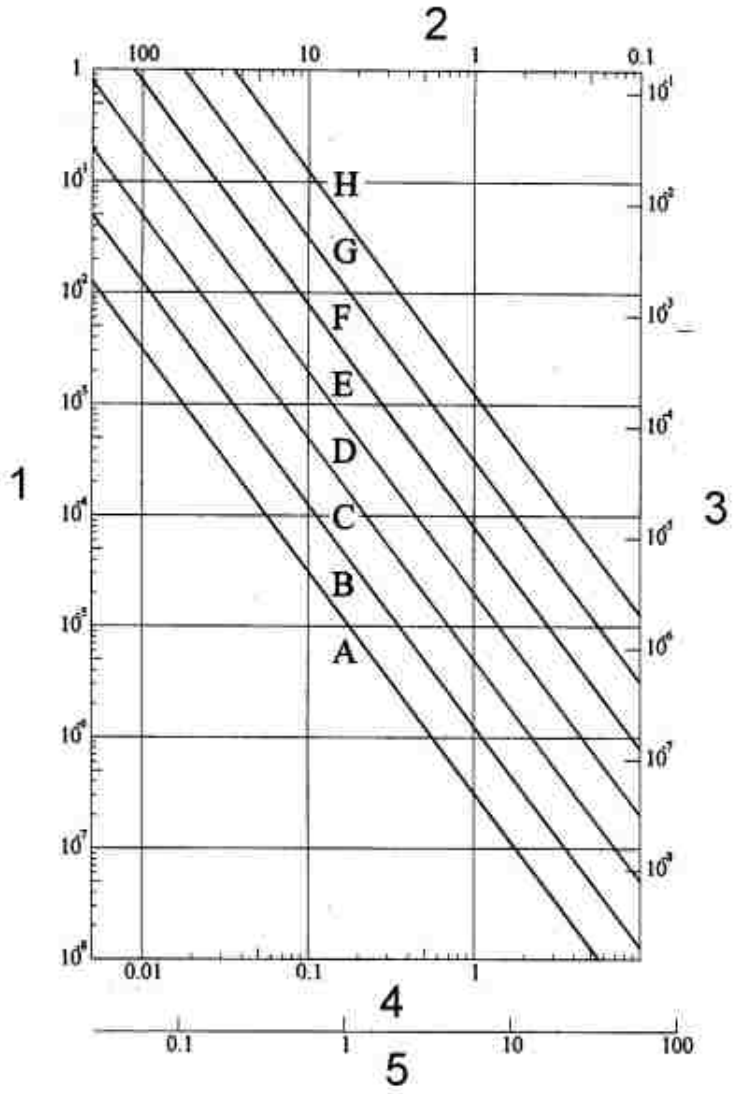

Figure 2.18: Road surface classification (ISO 8608) (reproduced from Tyan[?])

Table 2.1 and 2.2 show the road surface classification in terms of Ω and n. According to Tyan[?], the road input PSD in the frequency domain can be expressed as:

$$\Phi(\Omega) = \Phi(\Omega_0)(\frac{\Omega}{\Omega_0})^{-\omega} \tag{2.10}$$

$$\Phi(n) = \Phi(n0)(\frac{n}{n_0})^{-\omega} \tag{2.11}$$

where

- $\Omega = \frac{\pi}{L}$ is the radial spatial frequency, L is the wavelength in meters
- $\Phi_0 = \Phi(\Omega_0)$ in m_2/(rad/m) describes the value of the PSD at $\Omega_0 = 1$ rad/m

- ω, which is equal to 2 for most conditions, is the waviness
- $n = \frac{\Omega}{2\pi}$ is the spatial frequency and n_0 is equal to 0.1 cycle/m.

As there is only one parameter, Ω, the ISO 8608 can be used to easily classify large sets of diverse road profiles.

	degree of roughness $\Phi(n_0)(10^{-6}\mathrm{m}^2/(\mathrm{cycle/m}))$ where $n_0 = 0.1\mathrm{cycle/m}$		
road class	lower limit	geometric mean	upper limit
A (very good)	–	16	32
B (good)	32	64	128
C (average)	128	256	512
D (poor)	512	1,024	2,048
E (very poor)	2,048	4,096	8,192

Table 2.1: Degree of roughness in terms of n (reproduced from Tyan[?])

	degree of roughness $\Phi(n_0)(10^{-6}\mathrm{m}^2/(\mathrm{cycle/m}))$ where $n_0 = 0.1\mathrm{cycle/m}$		
road class	lower limit	geometric mean	upper limit
A (very good)	–	16	32
B (good)	32	64	128
C (average)	128	256	512
D (poor)	512	1,024	2,048
E (very poor)	2,048	4,096	8,192

Table 2.2: Degree of roughness in terms of Ω (reproduced from Tyan[?])

At the same time, a sinusoidal approximation of the road profile is given by Tyan[**?**]. If the vehicle is assumed to travel with a constant speed V over a road segment with length L, this random road profile can be approximated by a superposition of N sinusoidal waves expressed as:

$$z_{\mathrm{R}}(s) = \sum_{n=1}^{N} A_i \sin(\Omega_i s - \phi_i) \tag{2.12}$$

where the amplitude A_i is defined as follows:

$$A_i = \sqrt{\Phi(\Omega_i)\frac{\Delta\Omega}{\pi}} \tag{2.13}$$

in which $\Delta\Omega = \frac{\Omega_N - \Omega_1}{N-1}$ (rad/sec), and the phase angles $\phi_i, i = 1, ..., N$ are treated as random variables, following a uniform distribution in the the range from 0 to 2π. Also the road profile can also be generated in the time domain as:

$$z_{\mathrm{R}}(t) = \sum_{n=1}^{N} A_n \sin(n\omega_0 t - \phi_n) \tag{2.14}$$

where the fundamental temporal frequency $\omega_0 = V\Delta\Omega$, $\Delta\Omega = \frac{2\pi}{L}$ and $A_n = \sqrt{\Phi(\Omega_n)\frac{\Delta\Omega}{\pi}}, n = 1, ..., N$.

In this project, the ISO classification for random roads is used. Class A through D random roads are selected to test the small off-road vehicle.

2.5 Vehicle Dynamics

Vehicle dynamics is a field of engineering primarily based on classical mechanics. It is used to explore and understand the response of a vehicle in various in-motion situations. Vehicle dynamics plays an important role to determine the safety, handling response, and ride quality of many different kinds of vehicles.

2.5.1 Coordinate Frame

Before the analysis of the kinematics and dynamics of vehicle motion, an appropriate coordinate frame must be selected first for expressing the equations of motion. A vehicle coordinate frame $B(C_{xyz})$, of which the origin is attached to the mass centre of the vehicle, is shown in Figure 2.19. The longitudinal axis that passes through C in the forward direction is considered as the x-axis. The y-axis is in the lateral direction from right to left in the viewpoint of the driver. The z axis is in the vertical direction, perpendicular to the ground and opposite to the gravitational acceleration.

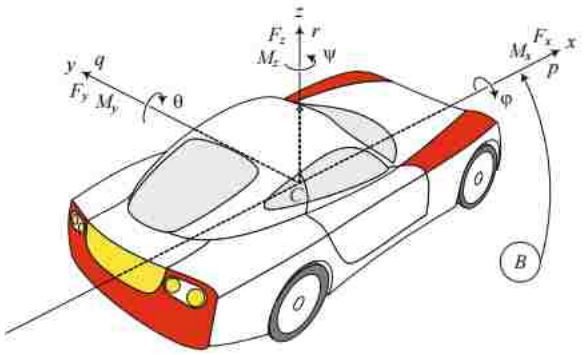

Figure 2.19: Vehicle coordinate frame $B(C_{xyz})$ (reproduced from Jazar[**?**])

Three angles, the roll angle ψ about the x-axis, the pitch angle θ about the y-axis, and the yaw angle ϕ about the z-axis, are employed to express the orientation of the vehicle coordinate frame. Another three motion variables are introduced, and called roll rate , pitch rate and yaw rate. These are the components of the angular velocity vector in the x, y, and z directions, respectively.

The relationship between the angular velocity and the orientation angles is a referred to as the kinematic differential equations.

$$\begin{pmatrix} \dot{\phi} \\ \dot{\theta} \\ \dot{\psi} \end{pmatrix} = \frac{1}{cos\theta} \begin{bmatrix} cos\theta & sin\phi sin\theta & cos\phi sin\theta \\ 0 & cos\phi cos\theta & -sin\phi cos\theta \\ 0 & sin\phi & cos\phi \end{bmatrix} \begin{pmatrix} p \\ q \\ r \end{pmatrix} \tag{2.15}$$

If the orientation angles are all close to zero, then a simplified relationship exists.

$$\dot{\phi} \approx p \tag{2.16}$$

$$\dot{\theta} \approx q \tag{2.17}$$

$$\dot{\psi} \approx r \tag{2.18}$$

The force system including the external force and moment received from the ground and environment can also be expressed in the vehicle coordinate frame:

$$B_{\mathrm{F}} = F_{\mathrm{x}}\hat{\mathbf{i}} + F_{\mathrm{y}}\hat{\mathbf{j}} + F_{\mathrm{y}}\hat{\mathbf{z}} \tag{2.19}$$

$$B_{\mathrm{M}} = M_{\mathrm{x}}\hat{\mathbf{i}} + M_{\mathrm{y}}\hat{\mathbf{j}} + M_{\mathrm{y}}\hat{\mathbf{z}} \tag{2.20}$$

All the individual components are shown in Figure 2.20.

- Longitudinal force F_{x} acts along the x-axis. $F_{\mathrm{x}} > 0$ means the vehicle is accelerating and $F_{\mathrm{x}} < 0$ braking. Longitudinal force is also sometimes called the forward force or traction force.
- Lateral force F_{y} acts along the y-axis, is sometimes called cornering force, and is a result of steering input.
- Normal force F_{z} acts in the vertical direction, and is often called the vertical force or vehicle load.
- Roll moment M_{x} is a longitudinal moment about the x-axis, often resulting from application of cornering force. It is also called the bank moment, tilting torque or overturning moment.
- Pitch moment M_{y}, is a moment about the y-axis, usually caused by application of traction force.
- Yaw moment M_{z} acts around the z axis, and is also a result of steering input. The yaw moment is also sometimes called the aligning moment.

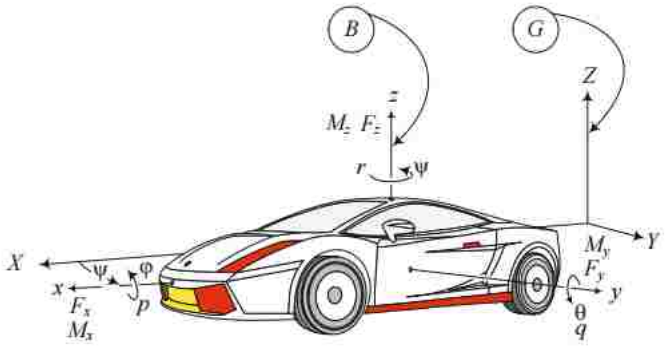

Figure 2.20: Vehicle coordinate frame $B(C_{xyz})$ and global coordinate frame $G(C_{xyz})$ (reproduced from Jazar[?])

2.5.2 Equations of Motion

In mathematical physics, the equations of motion are used to describe the behavior of a physical system in terms of its motion over time. The equations of motion can be simply classified under some main categories such as translations, rotations, or some combinations of these. According to Liu[?], the equations of motion can be used for rigid body analysis, such as vibration analysis, frequency domain analysis, and time domain analysis. Based on Liu's method, some vehicle models with varying number of degrees of freedom (DOFs) are built to generate the equations of motion.

6-Degree-of-Freedom (DOF) System

A 6-DOF model shown in Figure 2.21 is described first. A vehicle cab body is connected to the ground through four mounts, each of the mounts has three springs and dampers along x, y and z directions. All the stiffness and damping in the same direction are assumed to be the same. The three translational motions and three rotational motions are the 6-DOF of the vehicle. According to Newton's second law, the equations of motion can be derived as following:

$$m\ddot{x} + (k_{1x} + k_{2x} + k_{3x} + k_{4x})x + c(-k_{1x} - k_{3x} + k_{2x} + k_{4x})\psi + (c_{1x} + c_{2x} + c_{3x} + c_{4x})\dot{x} + c(-c_{1x} - c_{3x} + c_{2x} + c_{4x})\dot{\psi} = 0 \quad (2.21)$$

$$m\ddot{y} - (k_{1y} + k_{2y} + k_{3y} + k_{4y})y - c(k_{1y} - k_{3y} + k_{2y} - k_{4y})\psi + (c_{1y} + c_{2y} + c_{3y} + c_{4y})\dot{y} + c(-c_{1y} - c_{3y} + c_{2y} - c_{4y})\dot{\psi} = 0 \quad (2.22)$$

$$m\ddot{z} + (k_{1z} + k_{2z} + k_{3z} + k_{4z})z + (-ak_{1z} - ak_{2z} + bk_{3z} + bk_{4z})\theta + c(k_{1z} + k_{2z} - k_{3z} - k_{4z})\phi + (c_{1z} + c_{3z} + c_{2z} + c_{4z})\dot{z} + (-ac_{1z} - ac_{2z} + bc_{3z} + bc_{4z})\dot{\theta} + c(c_{1z} - c_{2z} + c_{3z} - c_{4z})\dot{\phi} = 0 \quad (2.23)$$

$$I_{xx}\ddot{\phi} + (ck_{1z} - dk_{2z} + ck_{3z} - 4k_{4x})z + c(-ak_{1z} + ak_{2z} + bk_{3z} - bk_{4z})\theta + c^2(k_{1z} + k_{2z} + k_{3z} + k_{4z})\phi + c(c_{1z} - c_{2z} + cc_{3z} - c_{4z})\dot{z} + c(-ac_{1z} + ac_{2z} + bc_{3z} - bc_{4z})\dot{\theta} + c^2(c_{1z} + c_{2z} + c_{3z} + c_{4z})\dot{\phi} = 0 \quad (2.24)$$

$$I_{yy}\ddot{\theta} + (-ak_{1z} - ak_{2z} + bk_{3z} + bk_{4z})z + (a^2k_{1z} + a^2k_{2z} + b^2k_{3z} + b^2k_{4z})\theta + c(-ak_{1z} + ak_{2z} + bk_{3z} - bk_{4z})\phi + (-ac_{1z} - ac_{2z} + bc_{3z} + bc_{4z})\dot{z} + (a^2c_{1z} + a^2c_{2z} + b^2c_{3z} + b^2c_{4z})\dot{\theta} + c(-ac_{1z} + ac_{2z} + bc_{3z} - bk_{4z})\dot{\phi} = 0 \quad (2.25)$$

$$I_{zz}\ddot{\psi} + (ak_{1y} + ak_{2y} - bk_{3y} - bk_{4y})y + (ac_{1y} + ac_{2y} - bc_{3y} - bc_{4y})\dot{y} + (a^2k_{1y} + a^2k_{2y} + b^2k_{3y} + b^2k_{4y} + c^2k_{1x} + c^2k_{2x} + c^2k_{3x} + c^2k_{4x})\psi + (a^2c_{1y} + a^2c_{2y} + b^2c_{3y} + b^2c_{4y} + c^2c_{1x} + c^2c_{2x} + c^2c_{3x} + c^2c_{4x})\dot{\psi} + c(-k_{1x} - k_{3x} + k_{2x} + k_{4x})x + c(-c_{1x} - c_{3x} + c_{2x} + c_{4x})\dot{x} = 0 \quad (2.26)$$

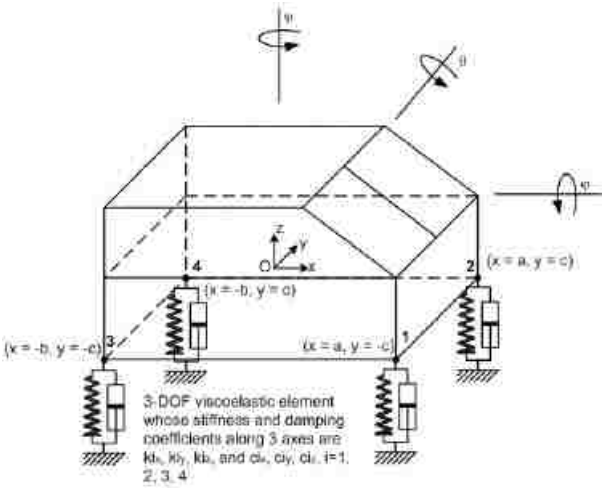

Figure 2.21: Liu's 6-DOF vehicle model (reproduced from Liu[?])

Assume the coordinate of the ith spring is (x_i, y_i, z_i), and $(k_{ix}, k_{iy}, k_{iz}, c_{ix}, c_m iy, c_{iz})$ are its stiffness and damping coefficients along the x, y, and z directions. From Equations 2.21–2.26, the system stiffness and damping

matrices can be written as below.

$$K_i = \begin{bmatrix} k_{ix} & 0 & 0 & 0 & 0 & -k_{ix}y_i \\ 0 & k_{iy} & 0 & 0 & 0 & k_{iy}x_i \\ 0 & 0 & k_{iz} & -k_{iz}x_i & k_{iz}y_i & 0 \\ 0 & 0 & -k_{iz}x_i & k_{iz}x_i^2 & -k_{iz}x_iy_i & 0 \\ 0 & 0 & k_{iz}y_i & -k_{iz}x_iy_i & k_{iz}y_i^2 & 0 \\ -k_{ix}y_i & k_{iy}x_i & 0 & 0 & 0 & k_{ix}y_i^2 + k_{iy}x_i^2 \end{bmatrix} \tag{2.27}$$

$$C_i = \begin{bmatrix} c_{ix} & 0 & 0 & 0 & 0 & -c_{ix}y_i \\ 0 & c_{iy} & 0 & 0 & 0 & c_{iy}x_i \\ 0 & 0 & c_{iz} & -c_{iz}x_i & c_{iz}y_i & 0 \\ 0 & 0 & -c_{iz}x_i & c_{iz}x_i^2 & -c_{iz}x_iy_i & 0 \\ 0 & 0 & c_{iz}y_i & -c_{iz}x_iy_i & c_{iz}y_i^2 & 0 \\ -c_{ix}y_i & c_{iy}x_i & 0 & 0 & 0 & c_{ix}y_i^2 + c_{iy}x_i^2 \end{bmatrix} \tag{2.28}$$

Correspondingly, the mass matrix of the system can be included as:

$$\left[M\right] = \begin{bmatrix} m & 0 & 0 & 0 & 0 & 0 \\ 0 & m & 0 & 0 & 0 & 0 \\ 0 & 0 & m & 0 & 0 & 0 \\ 0 & 0 & 0 & I_{xx} & I_{xy} & I_{xz} \\ 0 & 0 & 0 & I_{yx} & I_{yy} & I_{yz} \\ 0 & 0 & 0 & I_{zx} & I_{zy} & I_{zz} \end{bmatrix} \tag{2.29}$$

Based on the mass matrix M, stiffness matrix K and damping matrix C, the equation of motion for the entire system can be easily expressed as:

$$M\ddot{x} + C\dot{x} + Kx = f \tag{2.30}$$

where x is the system's displacement vector, and f is the applied force vector.

7-DOF system

Shown in Figure 2.22, a 7-DOF vehicle model including four vertical motions of the unsprung masses and vertical motions, roll, and pitch motions of the sprung masses are also produced by Feng et al[**?**].

According to Feng, each corner of the vehicle is identified with an i,j index, in which left/right is defined by l,r and front/rear by f,r, so the corners can be expressed as:

$$z_{\mathrm{fl}} = z - \alpha l_{\mathrm{f}} + \beta w - z_{\mathrm{tfl}} \tag{2.31}$$

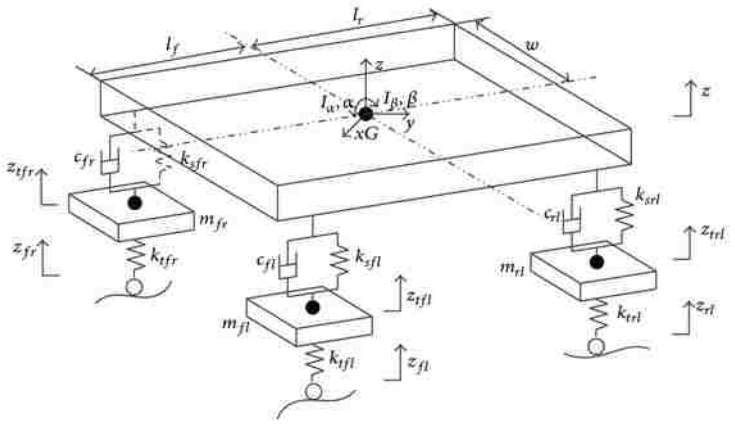

Figure 2.22: 7-DOF Full vehicle model (reproduced from Feng et al[?])

$$z_{\mathrm{fr}} = z - \alpha l_{\mathrm{f}} + \beta w - z_{\mathrm{tfr}} \tag{2.32}$$

$$z_{\mathrm{rl}} = z + \alpha l_{\mathrm{r}} + \beta w - z_{\mathrm{trl}} \tag{2.33}$$

$$z_{\mathrm{rr}} = z + \alpha l_{\mathrm{r}} - \beta w - z_{\mathrm{trr}} \tag{2.34}$$

So the full vehicle model can be described by the following equations of motion:

$$m_{\mathrm{fl}}\ddot{z}_{\mathrm{tfl}} + k_{\mathrm{tfl}}(z_{\mathrm{tfl}} - z_{\mathrm{fl}}) - F_{\mathrm{sfl}} - F_{\mathrm{dfl}} = 0 \tag{2.35}$$

$$m_{\mathrm{fr}}\ddot{z}_{\mathrm{tfr}} + k_{\mathrm{tfr}}(z_{\mathrm{tfr}} - z_{\mathrm{fr}}) - F_{\mathrm{sfr}} - F_{\mathrm{dfr}} = 0 \tag{2.36}$$

$$m_{\mathrm{rl}}\ddot{z}_{\mathrm{trl}} + k_{\mathrm{trl}}(z_{\mathrm{trl}} - z_{\mathrm{rl}}) - F_{\mathrm{srl}} - F_{\mathrm{drl}} = 0 \tag{2.37}$$

$$m_{\mathrm{rr}}\ddot{z}_{\mathrm{trr}} + k_{\mathrm{trr}}(z_{\mathrm{trr}} - z_{\mathrm{rr}}) - F_{\mathrm{srr}} - F_{\mathrm{drr}} = 0 \tag{2.38}$$

$$\sum m\ddot{z} + F_{\mathrm{s}ij} + F_{\mathrm{d}ij} = 0 \tag{2.39}$$

$$\sum I_\alpha \ddot{\alpha} - F_{\mathrm{sf}j} l_{\mathrm{f}} + F_{\mathrm{sr}j} l_{\mathrm{r}} - F_{\mathrm{df}j} l_{\mathrm{f}} + F_{\mathrm{dr}j} l_{\mathrm{r}} = 0 \tag{2.40}$$

$$\sum I_\beta \ddot{\beta} + wlF_{\mathrm{s}il} - wF_{\mathrm{s}ir} + wF_{\mathrm{d}il} - wF_{\mathrm{d}ir} = 0 \tag{2.41}$$

where m and m_{ij} are defined as spring and unsprung mass, respectively. The moment of inertia about the y-axis and x-axis are defined as I_α and I_β, respectively. The spring and damper forces are $F_{\mathrm{s}ij}$ and $F_{\mathrm{d}ij}$, respectively. The stiffness $k_{\mathrm{s}ij}$ and damping c_{ij} are utilized to express $F_{\mathrm{s}ij}$ and $F_{\mathrm{d}ij}$ by:

$$F_{\mathrm{s}ij} = k_{\mathrm{s}ij} z_{ij} \tag{2.42}$$

$$F_{dij} = c_{ij}\dot{z}_{ij} \tag{2.43}$$

12-DOF system

Shown in Figure 2.23, a 12-DOF system describing a cab and a frame can be considered as two 6-DOF systems. The cab is connected to the frame through four mounts in which the stiffness and damping in the same direction are the same.

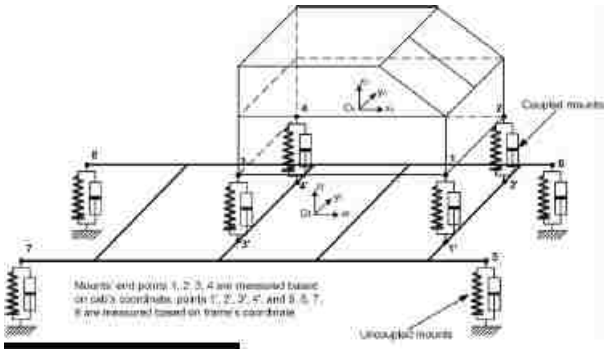

Figure 2.23: Liu's 12-DOF cab-frame system (reproduced from Liu[?])

The vertical displacements, rolling, pitching, lateral displacement and yawing between the cab and the frame can be considered as coupled together. Based on the coupling characteristic, the 12-DOF system's equations of motion can be represented as two coupled sets of differential equations. In this system, two different coordinates are required; one of them is the coordinate between the frame and the ground, the other one is the coordinate between the cab and frame.

Full vehicle model

A concept vehicle model presented by Liu[**?**] is used to analyze the equations of motion of the full vehicle. Shown in Figure 2.24, this model includes one cab, one frame, two suspensions, and four wheels. The cab is connected to the frame with four 3-DOF viscoelastic elements, the frame is connected to the two suspensions with four viscoelastic elements, and each wheel is connected to the ground through one viscoelastic element. As all the major components are assumed to be 6-DOF rigid bodies, therefore, the number of DOF is 48 in total. However, there is no direct relationship of the relative motion between unconnected components, so the whole vehicle model can be considered as a group of 6-DOF systems and coupled 12-DOF systems. The equations of motion of the full vehicle model can be obtained by assembling the appropriate submatrices together.

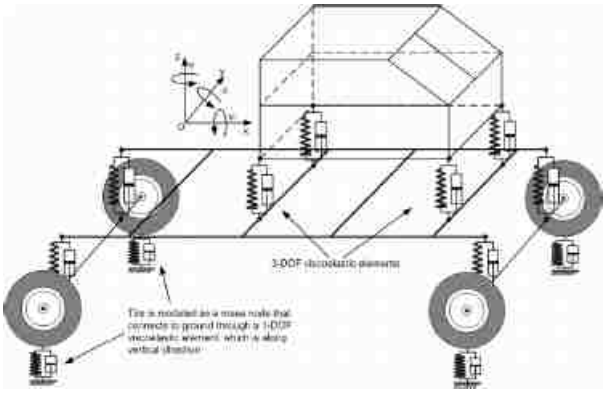

Figure 2.24: Full vehicle model (reproduced from Liu[?])

2.6 Comparisons of Simulations and Experiment

In this project, no experimental measurements have been conducted for validation of the simulation results. When working in simulation alone, it is always a question if the results are trustworthy. However, in the area of vehicle dynamics, the precision and consistency between computer aided simulation and experiment has been well documented. For example, in 2014, using the software Altair MotionView®, Ardiri et al[?] designed a 10-DOF mechanical model of a Paiggio scooter incorporating fifteen rigid bodies. The numerical analysis result from MotionView® is compared with the result based on a roller test bench, which is a severe test designed for reliability studies of the scooter suspension components. As shown in Figure 2.25, the suspension stroke time histories in the numerical analysis and experimental results agree quite well, in particular the two points corresponding to the maximum compression and the maximum extension of the suspension. Also, due to the nonlinear asymmetric damping used in the model, when cycled, the suspension exhibits a 'jacking down' phenomenon, where its oscillation is not centered about the static equilibrium point. The agreement of the results concerning this effect are fairly good too, with a reported discrepancy between experimental and simulation results of less than 5%.

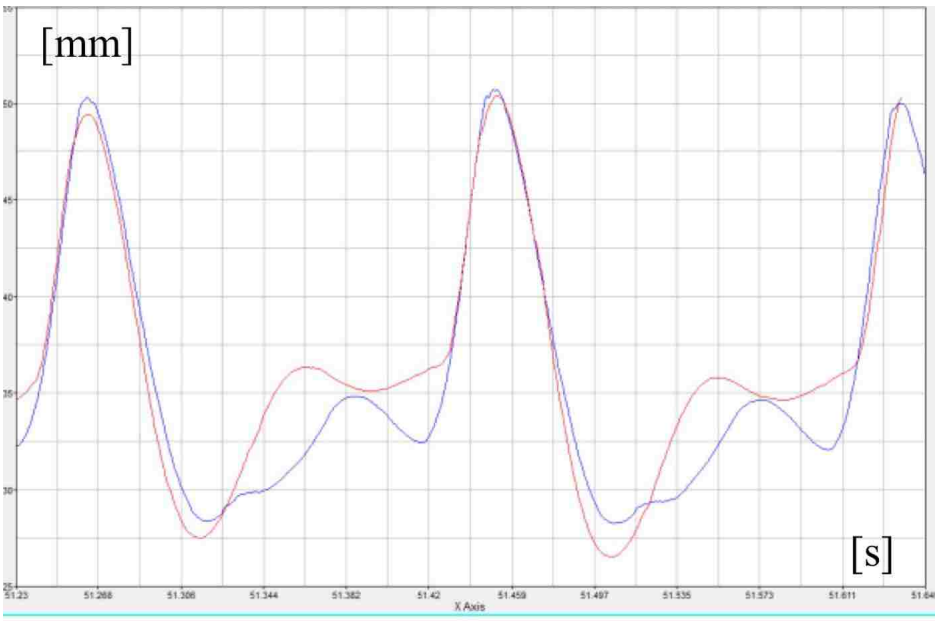

Figure 2.25: Model validation (reproduced from Ardiri[?])

While the author does not discount the value of experimental results, it was decided that in this case, the time and expense associated with the experiments required to validate the simulation results were not warranted. Secondly, even in light of some small discrepancy between the simulation and experiment, the author is confident that the simulation tools would be capable to accurately predict the trends and relative merit of the various suspension configurations. The decision was made to proceed based on simulation results alone.

Chapter 3

Dynamic Model

3.1 Interconnected Suspension Design

3.1.1 SAE Baja

The SAE Baja is an annual design challenge event hosted by SAE International, as a part of their Collegiate Design Series, where teams of undergraduate and graduate engineering students design, analyze, build, test and compete in small off-road style race cars. Since 2000, the University of Windsor has taken part in this competition. The University of Windsor Baja 2013 model has been chosen as the platform to implement the proposed interconnected suspension in this project.

The computer aided engineering software CATIA, by Dassault Systèmes, was utilized to design three variations of the suspension system:

conventional as designed by the 2013 UWindsor SAE Baja team, used a double A-arm style front suspension and independent trailing arms for the rear suspension

anti-roll identical to the conventional suspension, but with an anti-roll bar added to the front suspension to increase roll stiffness

interconnected modified from the anti-roll bar configuration such that the anti-roll bar is now supported in a mechanism that releases some deflection from the bar during suspension twist motions

The CATIA model is shown in Figure 3.1.

3.1.2 Motivation and Novelty

For a traditional suspension, an increase in roll stiffness is always accompanied with changes in the twist stiffness. This interconnected structure aims to increase the roll stiffness with minimal influence on the twist stiffness of

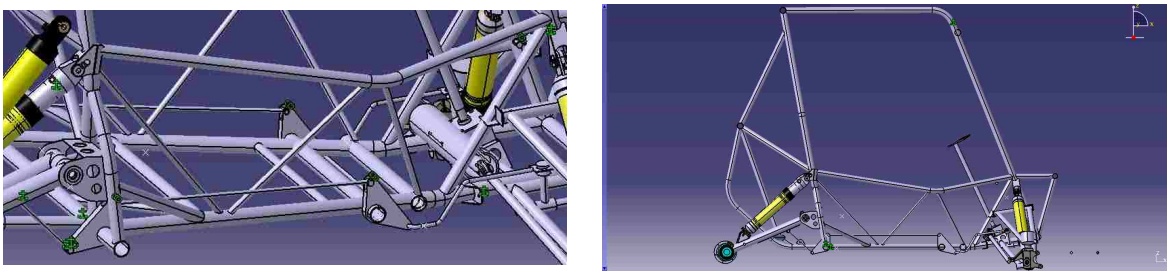

Figure 3.1: Interconnected suspension applied on the University of Windsor Baja car

the vehicle. This lightweight and compact suspension structure with four bell-cranks can fit in this small off-road vehicle appropriately, and maintains compatibility with the current suspension design. Potential negative effects, such as collisions between the bell-cranks and the ground or tires, can be avoided. Also, the low cost of this all mechanical design is attractive when considering the budget concerns for Baja vehicle.

The bell-cranks on each side of the vehicle are linked by a bar with negligible mass, modeled as a link constraint. The two rear bell-cranks and the trailing arms are also linked, such that the rotation of rear bell-cranks is driven by the rear suspension motion. The interconnection works like so: the deflection of one rear suspension results in motion of the rear bell-crank, which in turn drives the motion of the front bell-crank. The front bell-crank carries the anti-roll bar, in place of the typical mounts fixed to the chassis. As a result, opposing motions at either of the rear suspension or the front suspension will result in twist in the anti-roll bar. If opposing motions occur at both the front and rear suspensions, the amount of anti-roll bar twist depends on the relative directions. For a rolling motion, where both front and rear suspensions move in the same direction, the anti-roll bar twist is increased. For a warping motion, where the front and rear suspension move in opposing directions, the anti-roll bar twist is minimized or eliminated.

It is important to note that the basic properties of the vehicle, such as the type of suspension mechanism, and the associated geometry, were chosen by the 2013 SAE Baja team, and represents a baseline vehicle design on which the interconnection mechanism is to be fitted. The CATIA model was utilized to determine a set of feasible dimensions for the anti-roll bar, and the interconnection mechanism. No attempts were made to optimize the properties of the suspension or the interconnection mechanism. In fact, there is significant design freedom in the geometry of the mechanism such that it is possible to achieve a mathematically equivalent dynamic model of the vehicle for many different physical configurations. The properties chosen were based on advice and the previous practical experience of the team advisor.

3.2 Multibody Model

In this work, a 13-DOF vehicle model is employed to simulate and analyze the interconnected suspension system. Six of the degrees of freedom are the chassis motions, i.e., the three translations, and three rotations. The other degrees of freedom are the relative motions of each of the four suspensions, and the three rotating motions of wheels (note that the rear wheels must be rotated together with the same angular velocity due to the rear axle). Clearly, from the examples in the literature, assembling the equations of motion for a full vehicle with many components in a suitable software is a challenging task, even more so when constraints are imposed on the motion. In this work the software tools EoM and Altair MotionView® are used to automatically build the vehicle equations of motion, and analyze the linear and non-linear results.

The equations of motion are constructed based on the properties of the multibody model. Fourteen rigid bodies are included in the models of all three configurations; the chassis, four wheels, the front suspension consisting of an upper A-arm, a lower A-arm, and an upright on each side of the vehicle, the rear suspension consisting of left and right trailing arms and the rear axle. In the anti-roll bar variation, two small rigid bodies are added to represent the arms of the anti-roll bar, with a torsional spring connecting them. In the interconnected model, four bell-cranks are added to connect the suspensions. With this structure, the roll stiffness is expected to increase with no change to the pitch and bounce stiffness, and minimal change to twist stiffness.

There are thirty nine constraints in the conventional model. The upper and lower A-arms are connected to the uprights by ball (or spherical) joints, and are both mounted to the chassis by hinge (or revolute) joints. A revolute joint added between the front wheel and the upright represents the wheel bearing. In the rear, each trailing arm is connected to the chassis with a revolute joint, and each rear wheel is connected to a trailing arm with a revolute joint. The two wheels are connected to the rear axle by constant velocity joints, (similar in function to a universal joint). With the additional torsional anti-bar mounted in the front of vehicle, the basic mechanical design is unchanged, but there two additional rigid bodies, two additional revolute joints, and two additional massless links to model the bar and its connections. In the interconnected model, four bell-cranks are mounted on the chassis with revolute joints. The linkage connecting the front and rear bell-cranks is modelled as a massless link. The rear bell-crank is connected to the trailing arm with another massless link, and the front bell-crank now carries the front anti-roll bar. Note that each type of joint has differing numbers of constraints, e.g., a spherical joint imposes three constraints, while a revolute joint adds five. In the end, regardless of the interconnection mechanism, all three variations have thirteen degrees of freedom.

For all three configurations, four coil springs appear as the shock absorbers, offering translational stiffness and damping between the wheels and chassis. The stiffness of the springs is set at 20000 N/m and damping is 100 Ns/m. In the anti-roll bar model, a torsional spring with 4000 Nm/rad runs across the chassis laterally to play the role of anti-roll bar. In the interconnected model, the torsional stiffness is modified to be 2000 Nm/rad. The

stiffness alteration between the anti-roll bar and interconnected configuration aims to maintain a fair comparison of total roll stiffness, and focus on the impact of the interconnected suspension system. Meanwhile, each tire contact is simulated as a bushing (or spring with zero free length), a vertical stiffness with a value of 75000 N/m is used; also each tire has lateral and longitudinal damping with a coefficient of 2000 Ns/m. In reality, the tire *slip ratio* and *slip angle* are the primary factors that determine tire longitudinal and lateral force, respectively. However, for small values of slip, the behaviour is well approximated by linear relationships, and are effectively equivalent to a linear damper in each direction. Note that all the parameters are consistent with the real values of an SAE Baja vehicle.

3.3 Model in EoM Software

EoM, an open source software developed by University of Windsor Vehicle Dynamics and Control research group, can be used to generate linear or linearized equations of motion for multibody mechanical system[?]. It runs under MATLAB® or Octave, an open source code using nearly identical syntax. EoM conducts several analyses on the linear equations, including modal analysis, frequency response, steady state sensitivity, static loads and deflections, and linear time history. The mass, damping, stiffness and constraint Jacobian matrices can be built by reading the information in the input file when EoM analyzes a multibody system. EoM forms the equations of motion in a series of steps. First, the kinematic differential equations, combined with the Newton-Euler equations of motion, are combined in a first order linear differential equation:

$$\begin{bmatrix} I & 0 \\ 0 & M \end{bmatrix} \begin{Bmatrix} \dot{p}_x \\ \dot{w}_x \end{Bmatrix} + \begin{bmatrix} V & -I \\ K & C \end{bmatrix} \begin{Bmatrix} p_x \\ w_x \end{Bmatrix} = \begin{Bmatrix} 0 \\ f_c + f_a \end{Bmatrix} \tag{3.1}$$

where the V matrix results from the linearization of the kinematic differential equations, and the C matrix contains the traditional viscous damping matrix, plus terms due to the inertia forces, i.e., centripetal forces and gyroscopic moments. The stiffness matrix K is the sum of terms resulting from deflection of elastic elements, and additional tangent stifness matrix terms. The mass matrix M results from the Newton-Euler equations, and is tri-diagonal as is typical. The p_x vector represents the global locations and small angle orientations, and the w_x represents the body fixed linear and angular velocities. The forces acting are the actuator forces f_a, and the constraint force f_c; however, the constraint forces are eliminated through a coordinate reduction.

The linearized constraint equations are written as:

$$\begin{bmatrix} B_h & 0 \\ -B_h V & B_h \\ 0 & B_{nh} \end{bmatrix} \begin{bmatrix} \dot{p}_x & p_x \\ \dot{w}_x & w_x \end{bmatrix} = \begin{bmatrix} 0 & 0 \\ 0 & 0 \\ 0 & 0 \end{bmatrix} \tag{3.2}$$

where the B_h and B_{nh} matrices represent holonomic and nonholonomic constraint equations, respectively. Using

an orthogonal complement to the constraint Jacobian, the set of differential equations can reduced to a minimal coordinate set, shown in standard descriptor state space form.

$$\begin{bmatrix} E & 0 \\ 0 & I \end{bmatrix} \begin{Bmatrix} \dot{x} \\ y \end{Bmatrix} = \begin{bmatrix} A & B \\ C & D \end{bmatrix} \begin{Bmatrix} x \\ u \end{Bmatrix} \tag{3.3}$$

3.3.1 System Elements in EoM

The EoM software describes a mechanical system in its input file by breaking it into a series of items of various types, e.g., rigid bodies, springs, bushings, sensors, etc. Each item type serves a specific purpose and has a number of attributes. These item types are listed and described in detail in Appendix C.

3.3.2 Tangent Stiffness Matrix

One interesting feature of the EoM software is its inclusion of the tangent stiffness matrix. According to Minaker[?], the tangent stiffness matrix is used to refer to the terms in the stiffness matrix that depend on the preloads in the system, and not on any physical flexibility. Ellis[?] derives the relationship between the suspension spring stiffness and the vehicle motion by taking into consideration the preload of the weight of the vehicle. By an energy balance, Equation 3.4 can be derived:

$$f\ dx = p\ dl \tag{3.4}$$

or

$$f = p\frac{dl}{dx} \tag{3.5}$$

where f represents the force between the wheel and ground and x represents the deflection of the suspension. Similarly, the compressive force in the spring is p and the length of the spring is l. The term $\frac{dl}{dx}$ is known as the *motion ratio*. Equation 3.6 can be differentiated by x to find the stiffness:

$$\frac{df}{dx} = \frac{dp}{dx}\frac{dl}{dx} + p\frac{d^2l}{dx^2} \tag{3.6}$$

where the term $\frac{df}{dx}$ is defined as the *wheel rate* and can also be expressed as:

$$\frac{df}{dx} = \frac{dp}{dl}\left(\frac{dl}{dx}\right)^2 + p\frac{d}{dx}\left(\frac{dl}{dx}\right) \tag{3.7}$$

The wheel rate is the spring rate times the square of the motion ratio, plus the spring preload times the rate of change of motion ratio. The second term can be considered as a tangent stiffness. If the motion ratio is constant, this term tends to be zero, but if the suspension has a rising rate, the tangent stiffness term should contribute to the wheel rate calculation.

In order to maximize the accuracy of the results in this project, the influence of the tangent stiffness matrix

should be included in the EoM simulation. However, the Altair MotionView® software is a commercial code, and it is unclear how the stiffness matrix is calculated there. In some experiments, the addition or deletion of gravity induced preload shows no effect on the modal results computed by MotionView®, yet it does show a noticeable effect in the non-linear transient solutions that are produced. This leads to challenges when comparing results from the two software tools. Gravity preload effects must be turned off in EoM to when comparing eigenvalue results to MotionView®, but are otherwise included for maximum fidelity.

3.3.3 Model Properties

In the EoM multibody model, the structures of the three configurations are as described. The interconnected configuration as animated by EoM is shown in Figure 3.2. The stiffness and damping, and the locations of connection and links in the interconnected suspension are listed in Tables 3.1 and 3.2. The locations of the bodies are shown in Table 3.3.

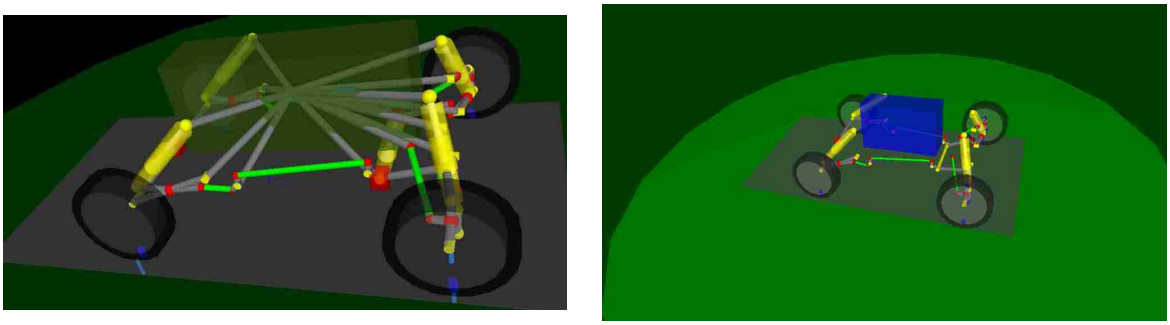

Figure 3.2: Baja structure model in EoM

Table 3.1: Stiffness and dampings

No.	Connection Name	Stiffness [N/m]	Damping [Ns/m]
1	Left rear tire	75,000	0.0000×10^0
2	Right rear tire	75,000	0.0000×10^0
3	Left front tire	75,000	0.0000×10^0
4	Right front tire	75,000	0.0000×10^0
5	Left rear tire	0	5.0000×10^3
6	Right rear tire	0	5.0000×10^3
7	Left front tire	0	5.0000×10^3
8	Right front tire	0	5.0000×10^3
1	Left rear shock	20,000	1.0000×10^3
2	Right rear shock	20,000	1.0000×10^3
3	Left front shock	20,000	1.0000×10^3
4	Right front shock	20,000	1.0000×10^3
5	Anti roll bar	2,000	0.0000×10^0

Table 3.2: Connection Locations

No.	Connection Name	Location [m]	Location [m]
1	Left rear shock	−0.087, 0.445, 0.672	−0.507, 0.445, 0.316
2	Right rear shock	−0.087, −0.445, 0.672	−0.507, −0.445, 0.316
3	Left front shock	0.947, 0.252, 0.652	1.048, 0.467, 0.243
4	Right front shock	0.947, −0.252, 0.652	1.048, −0.467, 0.243
5	Anti roll bar	0.700, 0.255, 0.240	0.700, −0.255, 0.240
6	Left tie-rod	0.840, 0.206, 0.376	0.960, 0.564, 0.274
7	Right tie-rod	0.840, −0.206, 0.376	0.960, −0.564, 0.274
8	Left rear link	−0.021, 0.360, 0.240	−0.140, 0.434, 0.310
9	Right rear link	−0.021, −0.360, 0.240	−0.140, −0.434, 0.310
10	Left link	0.651, 0.255, 0.328	0.028, 0.360, 0.328
11	Right link	0.651, −0.255, 0.328	0.028, −0.360, 0.328
12	Left front drop link	0.970, 0.270, 0.304	0.970, 0.270, 0.240
13	Right front drop link	0.970, −0.270, 0.304	0.970, −0.270, 0.240

Table 3.3: Body Location and Properties

Body Name	Location	Mass	Inertia (I_{xx}, I_{yy}, I_{zz})	Inertia (I_{xy}, I_{yz}, I_{zx})
Chassis	0.260, 0.000, 0.568	200.000	27.000, 61.000, 61.000	0.000, 0.000, 0.000
Left upper A-arm	0.994, 0.318, 0.435	0.683	0.008, 0.005, 0.010	0.001, −0.003, 0.000
Right upper A-arm	0.994, −0.318, 0.435	0.683	0.008, 0.005, 0.010	−0.001, 0.003, 0.000
Left lower A-arm	1.041, 0.378, 0.268	1.538	0.036, 0.014, 0.039	0.004, −0.012, 0.000
Right lower A-arm	1.041, −0.378, 0.268	1.538	0.036, 0.014, 0.039	−0.004, 0.012, 0.000
Left upright	1.039, 0.578, 0.279	0.640	0.001, 0.001, 0.001	0.000, 0.000, 0.000
Right upright	1.039, −0.578, 0.279	0.640	0.001, 0.001, 0.001	0.000, 0.000, 0.000
Left front wheel	1.041, 0.658, 0.253	5.556	0.134, 0.236, 0.134	0.000, 0.000, 0.000
Right front wheel	1.041, −0.658, 0.253	5.556	0.134, 0.236, 0.134	0.000, 0.000, 0.000
Left trailing arm	−0.321, 0.434, 0.291	3.133	0.020, 0.112, 0.104	−0.003, 0.000, 0.031
Right trailing arm	−0.321, −0.434, 0.291	3.133	0.020, 0.112, 0.104	0.003, 0.000, 0.031
Left rear wheel	−0.524, 0.600, 0.253	5.556	0.134, 0.236, 0.134	0.000, 0.000, 0.000
Right rear wheel	−0.524, −0.600, 0.253	5.556	0.134, 0.236, 0.134	0.000, 0.000, 0.000
Axle	−0.524, 0.000, 0.253	5.000	0.338, 0.010, 0.338	0.000, 0.000, 0.000
Left front arb bellcrank	0.651, 0.255, 0.279	0.090	0.000, 0.000, 0.000	0.000, 0.000, 0.000
Right front arb bellcrank	0.651, −0.255, 0.279	0.090	0.000, 0.000, 0.000	0.000, 0.000, 0.000
Left front arb	0.700, 0.255, 0.240	0.090	0.000, 0.000, 0.000	0.000, 0.000, 0.000
Right front arb	0.700, −0.255, 0.240	0.090	0.000, 0.000, 0.000	0.000, 0.000, 0.000
Left rear arb bellcrank	0.028, 0.360, 0.279	0.090	0.000, 0.000, 0.000	0.000, 0.000, 0.000
Right rear arb bellcrank	0.028, −0.360, 0.279	0.090	0.000, 0.000, 0.000	0.000, 0.000, 0.000

Note: all values are given in standard metric units, i.e., [m], [kg], [kg·m^2], and inertias are defined as the positive integral over the body, e.g., $I_{xy} = +\int r_x r_y dm$

The locations and directions of components are shown in Table 3.4.

Table 3.4: Connection Location and Direction

No.	Connection Name	Location [m]	Unit Axis
1	Left CV	−0.524, 0.450, 0.253	0.000, 1.000, 0.000
2	Right CV	−0.524, −0.450, 0.253	0.000, 1.000, 0.000
3	Left upper A-arm hinge	0.976, 0.212, 0.476	1.000, 0.000, 0.000
4	Left lower A-arm hinge	1.018, 0.185, 0.309	1.000, 0.000, 0.000
5	Left upper ball-joint	1.040, 0.539, 0.350	1.000, 0.000, 0.000
6	Left lower ball-joint	1.060, 0.568, 0.207	1.000, 0.000, 0.000
7	Left front wheel bearing	1.041, 0.686, 0.253	0.000, 1.000, 0.000
8	Right upper A-arm hinge	0.976, −0.212, 0.476	1.000, 0.000, 0.000
9	Right lower A-arm hinge	1.018, −0.185, 0.309	1.000, 0.000, 0.000
10	Right upper ball-joint	1.040, −0.539, 0.350	1.000, 0.000, 0.000
11	Right lower ball-joint	1.060, −0.568, 0.207	1.000, 0.000, 0.000
12	Right front wheel bearing	1.041, −0.686, 0.253	0.000, 1.000, 0.000
13	Left trailing arm bearing	−0.092, 0.429, 0.368	0.000, 1.000, 0.000
14	Right trailing arm bearing	−0.092, −0.429, 0.368	0.000, 1.000, 0.000
15	Left rear wheel bearing	−0.524, 0.492, 0.253	0.000, 1.000, 0.000
16	Right rear wheel bearing	−0.524, −0.492, 0.253	0.000, 1.000, 0.000
17	Left front arb bellcrank mount	0.651, 0.255, 0.279	0.000, 1.000, 0.000
18	Right front arb bellcrank mount	0.651, −0.255, 0.279	0.000, 1.000, 0.000
19	Left rear arb bellcrank mount	0.028, 0.360, 0.279	0.000, 1.000, 0.000
20	Right rear arb bellcrank mount	0.028, −0.360, 0.279	0.000, 1.000, 0.000
21	Left arb mount	0.700, 0.255, 0.240	0.000, 1.000, 0.000
22	Right arb mount	0.700, −0.255, 0.240	0.000, 1.000, 0.000
23	Left rear tire	−0.524, 0.600, 0.000	0.000, 0.000, 1.000
24	Right rear tire	−0.524, −0.600, 0.000	0.000, 0.000, 1.000
25	Left front tire	1.041, 0.658, 0.000	0.000, 0.000, 1.000
26	Right front tire	1.041, −0.658, 0.000	0.000, 0.000, 1.000
27	Left rear tire	−0.524, 0.600, 0.000	0.000, 0.000, 1.000
28	Right rear tire	−0.524, −0.600, 0.000	0.000, 0.000, 1.000
29	Left front tire	1.041, 0.658, 0.000	0.000, 0.000, 1.000
30	Right front tire	1.041, −0.658, 0.000	0.000, 0.000, 1.000
31	Constant Speed	0.260, 0.000, 0.568	1.000, 0.000, 0.000

The results of the EoM analysis are discussed in Chapter 4.

3.4 Model in Altair MotionView®

While the linear time-invariant multibody model has been built and analyzed in the software EoM, a non-linear model that is closer to reality is also used in this project. The standard computer aided engineering (CAE) software Altair Hyperworks® is employed, specifically the MotionView® multibody dynamics tool. Not only does MotionView® have the advantage of a graphical user interface (GUI), but also the response from different parts of the model can be easily shown and animated for a comprehensive understanding based on the kind of the input actuator.

Among the different solvers available, MotionView® supplies linear (modal analysis), transient (non-linear time history), and static. A three dimensional multibody model of a full vehicle is built to extend the EoM result of linear simulation and explore the performance of the non-linear simulation based on different types of road. Based on this structure, three variations of the suspension are modeled and compared: conventional suspension,

anti-roll bar suspension and interconnected suspension. The advantages and disadvantages are determined by their driving comfort and grip with the ground.

In Altair MotionView®, the algorithms used to solve the equations of motion are based on the differential-algebraic equation (DAE) method. There are four integrator types available. A DAE is an equation involving an unknown function and its derivatives. A first order DAE in its most general form is given by Campbell et al[**?**] as:

$$F(t, x, x') = 0, \quad t_0 \leq t \leq t_f \tag{3.8}$$

where $x = x(t)$, the unknown function, and $F = F(t, x, x')$ have N components, denoted by x_i and F_i, $i = 1, 2, ..., N$, respectively. Every DAE can be written as a first order DAE. The term DAE is usually reserved for the case when the highest derivative x' cannot be solved for in terms of t, x, when Equation 3.8 is viewed as an algebraic relationship between the variables t, x, x', i.e., the Jacobian $\partial F/\partial x'$ along a particular solution of the DAE may be singular. Systems of equations like Equation 3.8 are also called implicit systems, generalized systems, or descriptor systems. The DAE may be an initial value problem where x is specified at the initial time, $x(t_0) = x_0$, or a boundary value problem, where the solution is subjected to N two-point boundary conditions $g(x(t_0), x(t_f)) = 0$.

The method of solution of a DAE depends on its structure. A special but important class of DAEs of the form Equation 3.9 is the semi-explicit DAE or ordinary differential equation (ODE) with constraints:

$$\begin{aligned} y' &= f(t, y, z) \\ 0 &= g(t, y, z) \end{aligned} \tag{3.9}$$

which appear frequently in engineering applications, notably multibody dynamics. Here $g(t, y, z) = 0$ are the explicit constraints used to model the connecting elements such as hinges and ball joints.

3.4.1 Linear Model

The interconnected suspension model is selected as an example of the basic structure, and is shown in Figure 3.3. The three configurations were built and simulated in MotionView®. There are three noteworthy points:

In the MotionView model, in all three configurations, the rear axle is modeled as two small half-axles, the lengths of which are the same. They are each connected to a rear wheel by a constant velocity joint, and to each other with a telescopic joint. This allows for the change in length of the axle as the suspensions actuate in opposite directions with large deflections, to ensure the appropriate number of degrees of freedom in the rear suspension.

The damping and stiffness between the tires and the ground are challenging to model. As opposed to the case for the interface between tire and ground in the linear model, the vertical tire stiffness in MotionView® is located

at the centre of wheel. While this introduces a small error in the influence of camber change on roll moment, it is necessary to avoid the case where the wheel simply rolls forward and falls off the support, i.e., the vehicle 'falls down' as a result of misalignment between the weight and the internal vertical reaction load. In this case, the vehicle is effectively suspended from the top of the tire rather than resting on it. To avoid this problem entirely, the tire would have to be treated as a surface-to-surface contact, rather than a point-to-point contact, which significantly complicates the analysis. The damping in the lateral and longitudinal direction remains located at the ground surface.

All the 'link' items in EoM are reclassified as massless bodies in MotionView®, as there are no link constraints available. The effective motion of the mechanism is exactly the same, but additional equations of motion and additional constraint equations are required by the solver as a result. Where the link is represented as a single constraint equation, the massless body requires six differential equations, and seven constraints.

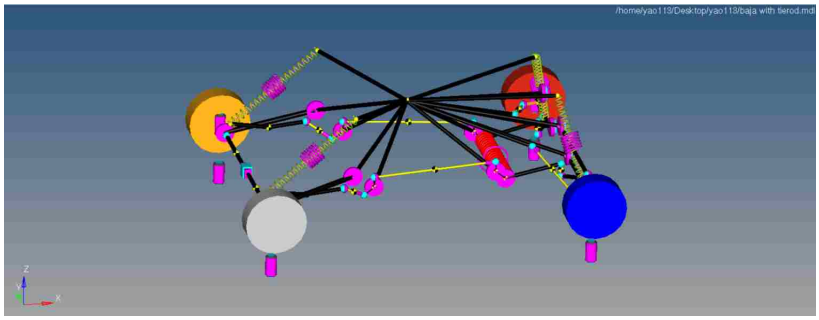

Figure 3.3: Baja MotionView® linear model

The linear modal analysis results from MotionView® are compared with those generated by EoM. The stability properties, natural frequency, and damping ratio can be determined in those models based on an analysis of the eigenvalues.

In the case of linear simulation, the software EoM has notable advantages over MotionView®:

- It is incorporated directly into the MATLAB® environment, offering convenient access to all the associated data processing tools.
- The open source nature of EoM ensures that the analyst has full access to and knowledge of the algorithms in use.
- Construction of the Altair model is more complex than EoM, e.g., the rigid point and link items in EoM simplify the model construction.
- The outputs in EoM are more detailed. While the eigenvalue analysis can be obtained in MotionView®, EoM also includes frequency response and steady state sensitivity by default, while these are not easily

generated in MotionView®. Additionally, the actual equations of motion are returned in EoM, as opposed to MotionView®, which returns only the solution to the equation of motion.

- As previously mentioned, the handling of the tangent stiffness matrix is unclear in MotionView®.

3.4.2 Non-linear Model

Of course, the strength of MotionView® is its non-linear transient solver. In the non-linear model, four imaginary ground bodies, instead of the global ground, are added to support the vehicle. As shown in Figure 3.4, a three-level structure is utilized. The stiffness and damping between the chassis and the tires are realized by the suspension, and each tire is driven by an imaginary ground, to simulate the up-and-down disturbance of the road. The imaginary ground is connected to the global ground with a translational joint, where one can apply any road disturbance desired.

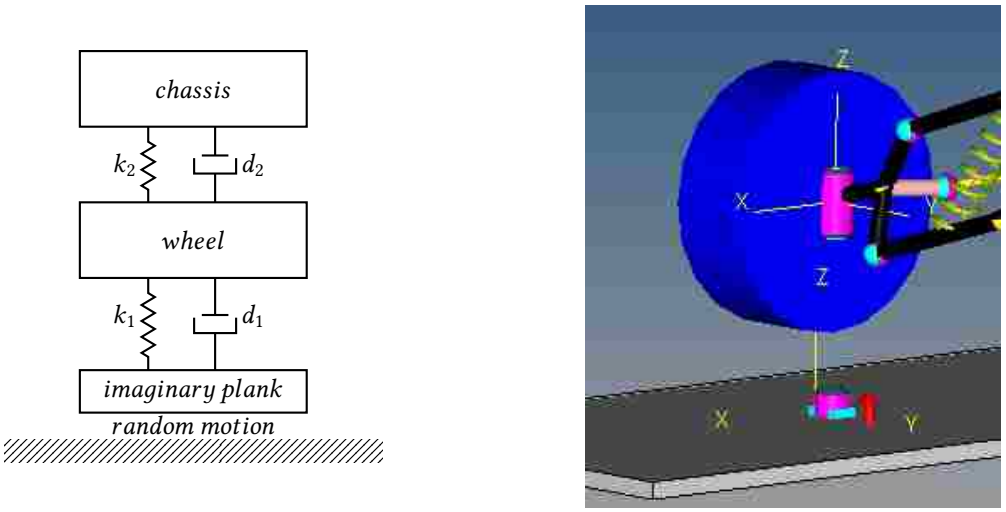

Figure 3.4: Structure of the Baja non-linear model

The non-linear tire vertical stiffness plot is shown as Figure 3.5; it clearly shows that when the tire leaves the ground, the stiffness becomes zero. When in contact, the tire force has a linear relationship with the tire compression. This model is closer to the reality than the simple linear model, as it can properly simulate the case when the vehicle leaves the ground.

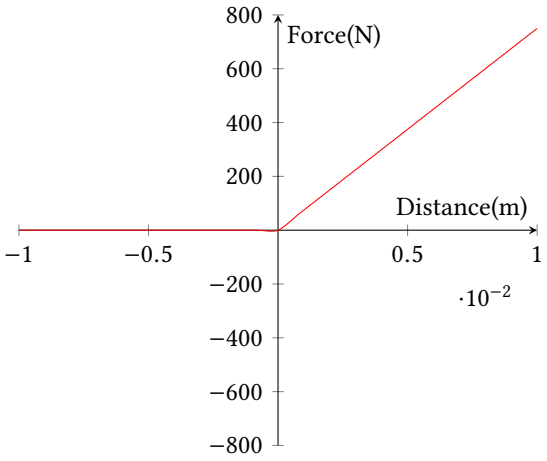

Figure 3.5: Vertical contact force between the tires and ground

The model with conventional suspension configuration is shown in Figure 3.6. In this model, the anti-roll bar and coupling structure are removed and all the suspension stiffness is supplied by the coil springs.

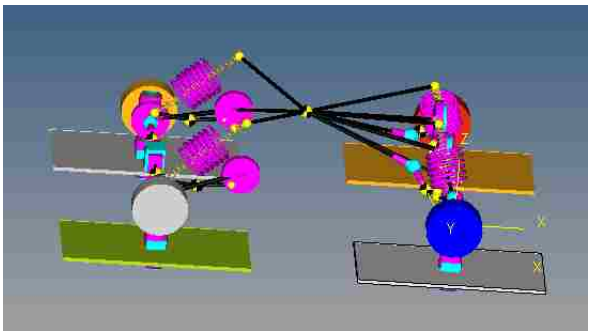

Figure 3.6: Baja model with conventional suspension

Shown in Figure 3.7, an anti-roll bar with stiffness of 4000 Nm/rad is added. The anti-roll bar aims to increase the roll stiffness for reduced roll when the vehicle is cornering.

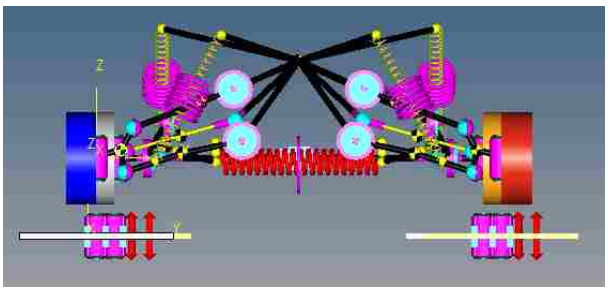

Figure 3.7: Baja model with anti-roll bar suspension

The interconnected suspension model is shown in Figure 3.8. Two bell-cranks are mounted on each side of the chassis to connected the front lower A-arm and rear trailing arm to build the coupling structure. In an additional change from the anti-roll bar configuration, the torsional stiffness of the anti-roll bar, now going through the front bell-cranks, is modified to 2000 Nm/rad to provide a fair comparison with equivalent overall roll stiffness to the anti-roll bar configuration.

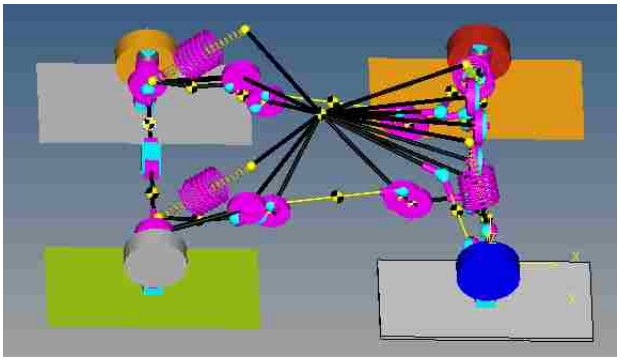

Figure 3.8: Baja model with interconnected suspension

The performance of the three configurations can be compared by exciting the vehicle with different road disturbance. These results are discussed in Chapter 4.

Chapter 4

Simulation Results

4.1 Linear Simulation

In the area of multibody vehicle dynamics, several crucial parameters, such as time constants, natural frequencies and damping ratios allow the design engineer to obtain a comprehensive and substantial view into the characteristics of the vehicle design, to ensure handling control and driving comfort.

In this project, linear simulations are implemented in the software EoM. Besides the stability and natural frequencies which are determined by the eigenvalues, the frequency response is obtained for the three vehicle configurations. The inputs to the vehicle are a roll moment applied to the chassis and a road displacement beneath the right front tire. The outputs are the chassis vertical displacement measured at the wheel, the suspension travel, and the tire compression. In addition to the frequency response, the the steady state gain, or the sensitivity relating each output to each input can be found. The results determined in EoM will also be compared with those from Altair MotionView®. It is noticeable that the gravity effect is not present within linear simulations in MotionView®, implying that the tangent stiffness matrix is not included in the equations of motion. As a result, gravity effects are not included in the models used in the comparison.

4.1.1 Dynamic Stability

The second order differential equation of motion can be expressed as:

$$M\ddot{x} + C\dot{x} + Kx = f(t) \tag{4.1}$$

where M is the mass matrix of the system, C denotes the damping matrix, and K represents the stiffness matrix. When there is no perturbation force applied to the system (i.e., $f(t) = 0$), the differential equation becomes

homogeneous and its solution can be written:

$$x = \beta e^{\alpha t} \tag{4.2}$$

where α represents the eigenvalues of the system. Note that β and α can be expressed as:

$$\alpha = a + bi \tag{4.3}$$

$$\beta = |D|e^{i\phi_s} \tag{4.4}$$

Substitute Equations 4.3and 4.4 into 4.2, and the solution of the differential equation can be written as:

$$x = |D|e^{i\phi_s}e^{(a+bi)t} \tag{4.5}$$

According to the Euler's formula, this can be expressed as:

$$x = |D|e^{at}[\cos(bt + \phi_s) + i\sin(bt + \phi_s)] \tag{4.6}$$

The stability of the system depends on the value of a; different cases of a are shown in Figure 4.1.

To illustrate the result more explicitly, the frequency of the sinusoidal signal and power of the exponential signal, in this instance, are set to be 25 Hz and 0.5 /sec, respectively. From the figure, only when $a < 0$, the system is stable, and the motion tends to zero. On the other hand, the rate of oscillation is determined by the imaginary part b, which is the so-called damped natural frequency, of the corresponding eigenvalues.

The natural frequency ω_n and damped natural frequency ω_d can be written:

$$\omega_n = \sqrt{a^2 + b^2} \tag{4.7}$$

$$\omega_d = \sqrt{1 - \zeta^2}\omega_n \tag{4.8}$$

where ζ is defined as the damping ratio:

$$\zeta = \frac{-a}{\sqrt{a^2 + b^2}} \tag{4.9}$$

A damping ratio of zero implies an undamped system that oscillates forever, while a damping ratio of one represents the transition between an oscillatory decay and an exponential decay, and is called critical damping.

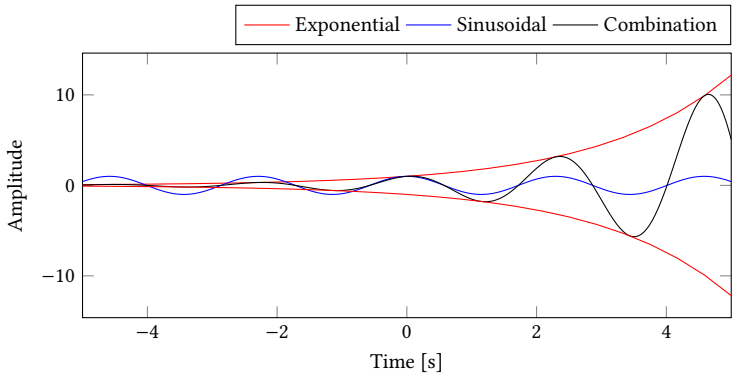

(a) $a > 0$

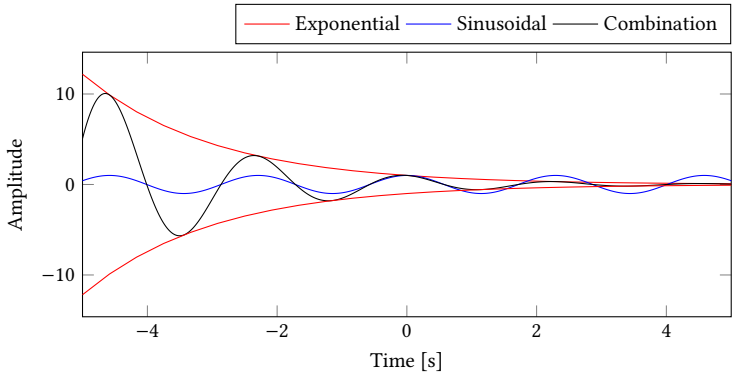

(b) $a < 0$

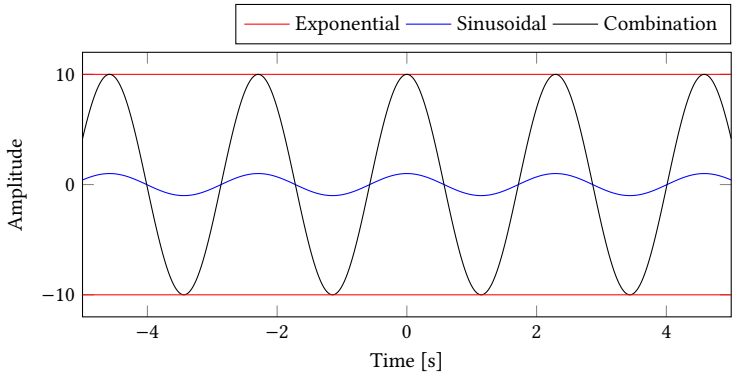

(c) $a = 0$

Figure 4.1: Stablity dependence on the value of a

4.1.2 Results in EoM

The results computed by EoM can be divided into three categories: a modal analysis, a frequency response analysis and a steady state analysis.

Modal Analysis

The first step is to determine the eigenvalues, natural frequencies, damping ratios and time constants. A simple summary is generated to describe the basic condition of the motions. As introduced in Chapter 3, there are thirteen degrees of freedom existing in each model. According to the second order differential equation, a pair of conjugate solutions can be obtained from a free motion. Therefore, twenty six eigenvalues should be generated. However, the addition of a fixed forward speed constraint adds an additional nonholonomic constraint that results in one fewer equation, and one less eigenvalue.

As shown in Tables 4.1, 4.2, and 4.3, amongst the motions, seven are oscillatory, and the rest, where the imaginary parts of the roots are zero, can be considered as overdamped motions. All the motions are predicted to be stable, with negative real parts. Any motions where the eigenvalues are zero show no response to initial conditions, and are referred to as rigid body modes. The EoM software also generates Virtual Reality Modeling Language (VRML) animations, providing a convenient method to display the mode shapes corresponding to the specific eigenvalues. According to the analysis, the rigid body motions are a combination of lateral displacement, longitudinal displacement, yaw displacement, and wheel angular displacement.

Table 4.1: Eigenvalues of conventional suspension

No.	Real [rad/s]	Imaginary [rad/s]	Real [Hz]	Imaginary [Hz]
1	-1.4079×10^{3}	0.0000×10^{0}	-2.2407×10^{2}	0.0000×10^{0}
2	-1.3792×10^{3}	0.0000×10^{0}	-2.1950×10^{2}	0.0000×10^{0}
3	-1.3652×10^{3}	0.0000×10^{0}	-2.1727×10^{2}	0.0000×10^{0}
4	-2.6610×10^{2}	0.0000×10^{0}	-4.2352×10^{1}	0.0000×10^{0}
5	-1.6598×10^{2}	0.0000×10^{0}	-2.6416×10^{1}	0.0000×10^{0}
6	-1.4493×10^{1}	8.8065×10^{1}	-2.3066×10^{0}	1.4016×10^{1}
7	-1.4493×10^{1}	-8.8065×10^{1}	-2.3066×10^{0}	-1.4016×10^{1}
8	-3.2128×10^{1}	9.2357×10^{1}	-5.1134×10^{0}	1.4699×10^{1}
9	-3.2128×10^{1}	-9.2357×10^{1}	-5.1134×10^{0}	-1.4699×10^{1}
10	-2.3432×10^{1}	9.4464×10^{1}	-3.7293×10^{0}	1.5034×10^{1}
11	-2.3432×10^{1}	-9.4464×10^{1}	-3.7293×10^{0}	-1.5034×10^{1}
12	-2.3261×10^{1}	9.7212×10^{1}	-3.7020×10^{0}	1.5472×10^{1}
13	-2.3261×10^{1}	-9.7212×10^{1}	-3.7020×10^{0}	-1.5472×10^{1}
14	-4.4828×10^{0}	1.5984×10^{1}	-7.1346×10^{-1}	2.5439×10^{0}
15	-4.4828×10^{0}	-1.5984×10^{1}	-7.1346×10^{-1}	-2.5439×10^{0}
16	0.0000×10^{0}	0.0000×10^{0}	0.0000×10^{0}	0.0000×10^{0}
17	0.0000×10^{0}	0.0000×10^{0}	0.0000×10^{0}	0.0000×10^{0}
18	-3.4587×10^{0}	1.1232×10^{1}	-5.5047×10^{-1}	1.7877×10^{0}
19	-3.4587×10^{0}	-1.1232×10^{1}	-5.5047×10^{-1}	-1.7877×10^{0}
20	-3.5820×10^{0}	1.0594×10^{1}	-5.7009×10^{-1}	1.6861×10^{0}
21	-3.5820×10^{0}	-1.0594×10^{1}	-5.7009×10^{-1}	-1.6861×10^{0}
22	0.0000×10^{0}	0.0000×10^{0}	0.0000×10^{0}	0.0000×10^{0}
23	0.0000×10^{0}	0.0000×10^{0}	0.0000×10^{0}	0.0000×10^{0}
24	0.0000×10^{0}	0.0000×10^{0}	0.0000×10^{0}	0.0000×10^{0}
25	0.0000×10^{0}	0.0000×10^{0}	0.0000×10^{0}	0.0000×10^{0}

Note: oscillatory roots appear as complex conjugates.

Shown as the imaginary part of Tables 4.1,4.2, and 4.3, three low frequency motions between 1.5 Hz and 3 Hz and four high frequency motions between 14 Hz and 17 Hz are obtained. The characteristics can be compared by

the natural frequencies in Table 4.4.

Table 4.2: Eigenvalues of anti-roll bar suspension

No.	Real [rad/s]	Imaginary [rad/s]	Real [Hz]	Imaginary [Hz]
1	-1.4079×10^3	0.0000×10^0	-2.2407×10^2	0.0000×10^0
2	-1.3792×10^3	0.0000×10^0	-2.1950×10^2	0.0000×10^0
3	-1.3652×10^3	0.0000×10^0	-2.1727×10^2	0.0000×10^0
4	-2.6567×10^2	0.0000×10^0	-4.2282×10^1	0.0000×10^0
5	-1.6599×10^2	0.0000×10^0	-2.6417×10^1	0.0000×10^0
6	-3.1989×10^1	9.2426×10^1	-5.0912×10^0	1.4710×10^1
7	-3.1989×10^1	-9.2426×10^1	-5.0912×10^0	-1.4710×10^1
8	-1.4497×10^1	8.8079×10^1	-2.3072×10^0	1.4018×10^1
9	-1.4497×10^1	-8.8079×10^1	-2.3072×10^0	-1.4018×10^1
10	-2.3709×10^1	1.0121×10^2	-3.7734×10^0	1.6109×10^1
11	-2.3709×10^1	-1.0121×10^2	-3.7734×10^0	-1.6109×10^1
12	-2.3432×10^1	9.4465×10^1	-3.7294×10^0	1.5035×10^1
13	-2.3432×10^1	-9.4465×10^1	-3.7294×10^0	-1.5035×10^1
14	-4.4805×10^0	1.5982×10^1	-7.1309×10^{-1}	2.5436×10^0
15	-4.4805×10^0	-1.5982×10^1	-7.1309×10^{-1}	-2.5436×10^0
16	0.0000×10^0	0.0000×10^0	0.0000×10^0	0.0000×10^0
17	0.0000×10^0	0.0000×10^0	0.0000×10^0	0.0000×10^0
18	-3.5492×10^0	1.2547×10^1	-5.6487×10^{-1}	1.9969×10^0
19	-3.5492×10^0	-1.2547×10^1	-5.6487×10^{-1}	-1.9969×10^0
20	-3.4599×10^0	1.1233×10^1	-5.5066×10^{-1}	1.7878×10^0
21	-3.4599×10^0	-1.1233×10^1	-5.5066×10^{-1}	-1.7878×10^0
22	0.0000×10^0	0.0000×10^0	0.0000×10^0	0.0000×10^0
23	0.0000×10^0	0.0000×10^0	0.0000×10^0	0.0000×10^0
24	0.0000×10^0	0.0000×10^0	0.0000×10^0	0.0000×10^0
25	0.0000×10^0	0.0000×10^0	0.0000×10^0	0.0000×10^0

Note: oscillatory roots appear as complex conjugates.

In Tables 4.1,4.2, and 4.3, the first five motions, of which the imaginary parts of eigenvalues are zero, can be considered as overdamped motion, confirmed with the support of the VRML animations. The damped modes consist of yaw velocity, wheel angular velocity and lateral velocity. The parts of the tables showing the oscillatory motions are of the primary interest, particularly the low frequency motions, as the are associated with chassis motion.

Table 4.3: Eigenvalues of interconnected suspension

No.	Real [rad/s]	Imaginary [rad/s]	Real [Hz]	Imaginary [Hz]
1	-1.4079×10^{3}	0.0000×10^{0}	-2.2407×10^{2}	0.0000×10^{0}
2	-1.3792×10^{3}	0.0000×10^{0}	-2.1950×10^{2}	0.0000×10^{0}
3	-1.3652×10^{3}	0.0000×10^{0}	-2.1727×10^{2}	0.0000×10^{0}
4	-2.6544×10^{2}	0.0000×10^{0}	-4.2247×10^{1}	0.0000×10^{0}
5	-1.6597×10^{2}	0.0000×10^{0}	-2.6414×10^{1}	0.0000×10^{0}
6	-1.4493×10^{1}	8.8065×10^{1}	-2.3066×10^{0}	1.4016×10^{1}
7	-1.4493×10^{1}	-8.8065×10^{1}	-2.3066×10^{0}	-1.4016×10^{1}
8	-3.2253×10^{1}	9.2602×10^{1}	-5.1333×10^{0}	1.4738×10^{1}
9	-3.2253×10^{1}	-9.2602×10^{1}	-5.1333×10^{0}	-1.4738×10^{1}
10	-2.3529×10^{1}	9.9627×10^{1}	-3.7447×10^{0}	1.5856×10^{1}
11	-2.3529×10^{1}	-9.9627×10^{1}	-3.7447×10^{0}	-1.5856×10^{1}
12	-2.3432×10^{1}	9.4464×10^{1}	-3.7293×10^{0}	1.5034×10^{1}
13	-2.3432×10^{1}	-9.4464×10^{1}	-3.7293×10^{0}	-1.5034×10^{1}
14	0.0000×10^{0}	0.0000×10^{0}	0.0000×10^{0}	0.0000×10^{0}
15	0.0000×10^{0}	0.0000×10^{0}	0.0000×10^{0}	0.0000×10^{0}
16	-4.4828×10^{0}	1.5984×10^{1}	-7.1346×10^{-1}	2.5439×10^{0}
17	-4.4828×10^{0}	-1.5984×10^{1}	-7.1346×10^{-1}	-2.5439×10^{0}
18	-3.4587×10^{0}	1.1232×10^{1}	-5.5047×10^{-1}	1.7877×10^{0}
19	-3.4587×10^{0}	-1.1232×10^{1}	-5.5047×10^{-1}	-1.7877×10^{0}
20	-3.5257×10^{0}	1.2897×10^{1}	-5.6113×10^{-1}	2.0526×10^{0}
21	-3.5257×10^{0}	-1.2897×10^{1}	-5.6113×10^{-1}	-2.0526×10^{0}
22	0.0000×10^{0}	0.0000×10^{0}	0.0000×10^{0}	0.0000×10^{0}
23	0.0000×10^{0}	0.0000×10^{0}	0.0000×10^{0}	0.0000×10^{0}
24	0.0000×10^{0}	0.0000×10^{0}	0.0000×10^{0}	0.0000×10^{0}
25	0.0000×10^{0}	0.0000×10^{0}	0.0000×10^{0}	0.0000×10^{0}

Note: oscillatory roots appear as complex conjugates.

As shown in Table 4.4, the low frequencies of the conventional suspension are 2.54 Hz for pitch, 1.78 Hz for bounce and 1.54 Hz for roll. The motions associated with the various frequencies are determined by observation of the modal animations. The results of the other two configurations are almost identical. It is noticeable that the roll frequencies increase to 1.99 Hz and 2.05 Hz in anti-roll bar and interconnected suspension configurations, respectively. This is expected, as the anti-roll bar does not affect the pitch and bounce motions, while it does have an obvious influence on roll motion.

The four high frequency motions correspond to ‘wheel hop’. An in phase wheel hop, and and out of phase wheel hop mode is predicted for each axle. All the high frequencies are in the range between 13 Hz and 17 Hz. Because the wheel hop frequencies are primarily determined by the much higher stiffness between the tires and ground rather than that of suspension, the high frequencies remain relatively constant for the three configurations. As the warp motion of the suspension only appears in the wheel hop modes, the distinction between the two configurations with modification is not apparent in the natural frequency results.

Table 4.4: Natural frequency

No.	Conventional	Anti-roll bar	Interconnected
1	–	–	–
2	–	–	–
3	–	–	–
4	–	–	–
5	–	–	–
6	1.4204×10^1	1.5566×10^1	1.4204×10^1
7	1.4204×10^1	1.5566×10^1	1.4204×10^1
8	1.5563×10^1	1.4207×10^1	1.5606×10^1
9	1.5563×10^1	1.4207×10^1	1.5606×10^1
10	1.5490×10^1	1.6545×10^1	1.6292×10^1
11	1.5490×10^1	1.6545×10^1	1.6292×10^1
12	1.5909×10^1	1.5490×10^1	1.5490×10^1
13	1.5909×10^1	1.5490×10^1	1.5490×10^1
14	2.6421×10^0	2.6417×10^0	–
15	2.6421×10^0	2.6417×10^0	–
16	–	–	2.6421×10^0
17	–	–	2.6421×10^0
18	1.8705×10^0	2.0752×10^0	1.8705×10^0
19	1.8705×10^0	2.0752×10^0	1.8705×10^0
20	1.7798×10^0	1.8707×10^0	2.1279×10^0
21	1.7798×10^0	1.8707×10^0	2.1279×10^0
22	–	–	–
23	–	–	–
24	–	–	–
25	–	–	–

Frequency Response

The frequency response of the three configurations is also analyzed. Results from the right front wheel of the conventional suspension model are shown in Figure 4.2; one noteworthy point is that the y-axis is 20 times the base 10 logarithm of the ratio of the vertical displacement of the vehicle part to the road vertical motion i.e., it is expressed in units of decibels. The frequency domain can be divided into three ranges: (1) low frequency, below the natural frequency of chassis bounce, (2) midrange frequency, between the natural frequency of chassis and wheel hop, (3) high frequency, beyond the natural frequency of wheel hop.

The logarithmic plot shows the perturbation of road is almost entirely absorbed by the chassis in the low frequency domain. At the beginning of the midrange, the chassis motion reaches its peak and is even larger than the displacement of the road; this can be explained by a resonance. In the midrange between approximately 1 Hz to 10 Hz, the suspension takes charge of absorbing the disturbance, while the chassis motion decreases. The resonance phenomenon of the suspension appears in the range between 11 Hz to 16 Hz, and then an obvious increase of tire deflection is shown in the high frequency domain.

In the ideal condition, the wider the midrange is, the better the vehicle performs. If the energy is primarily absorbed by chassis motion, driving comfort of the passengers is deteriorated. However, a balance has to be struck between reducing the chassis motion frequencies, and controlling chassis motion under cornering and

braking loads. Meanwhile, road grip is lost if the tire is employed to absorb the disturbance. The interconnected suspension aims to improve driving comfort while avoiding the penalty of lost grip.

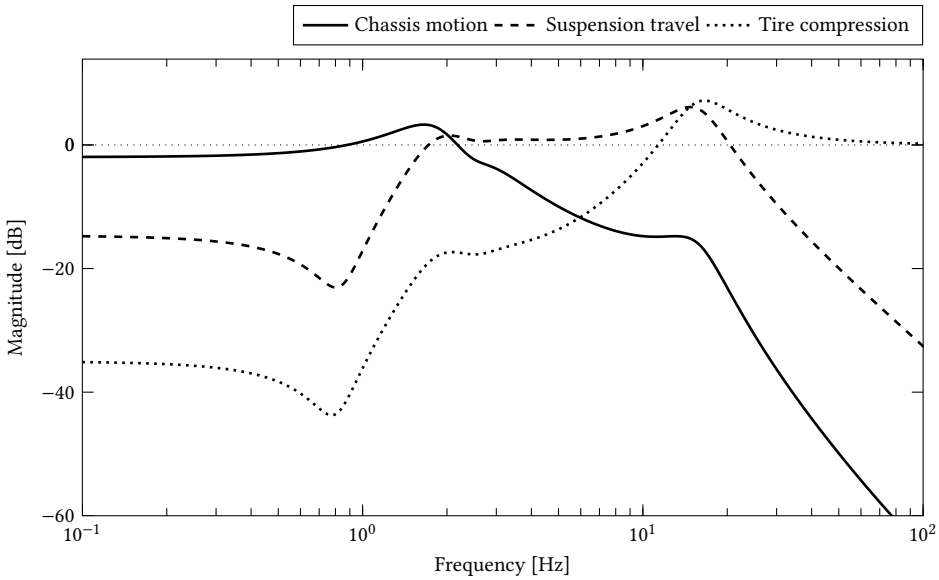

Figure 4.2: Frequency response of baseline vehicle at right front corner to road displacement

Figure 4.3 shows the chassis motion of the three configurations in response to the road disturbance applied on the right front wheel, where the sensor of the chassis is located adjacent to the wheel. The logarithmic plot can illustrate the distinctions among the three configurations. The difference primarily appears in the midrange and it clearly shows that both anti-roll bar and interconnected suspension perform worse than the conventional suspension, especially in the 2 Hz to 3 Hz band. This is reasonable because both the anti-roll bar and interconnected structure increase the roll stiffness, which leads to the driving comfort penalty. The three curves tend to be identical when they reach the high frequency range.

Figure 4.4 shows the comparison of the suspension travel of the three configurations in response to the road disturbance. The difference primarily exists in the low and midrange frequencies, where both the interconnected and conventional suspension perform better than the anti-roll bar. This means that the interconnected suspension is relatively more capable of reducing chassis motion without driver discomfort. The results also show strong similarity in the high frequency domain.

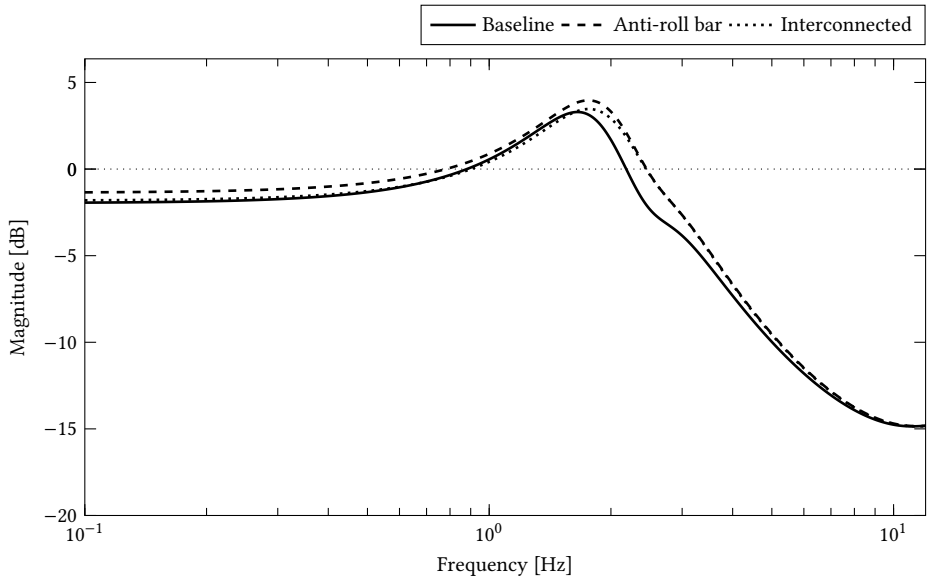

Figure 4.3: Frequency response showing chassis motion of vehicle at right front corner in response to road displacement

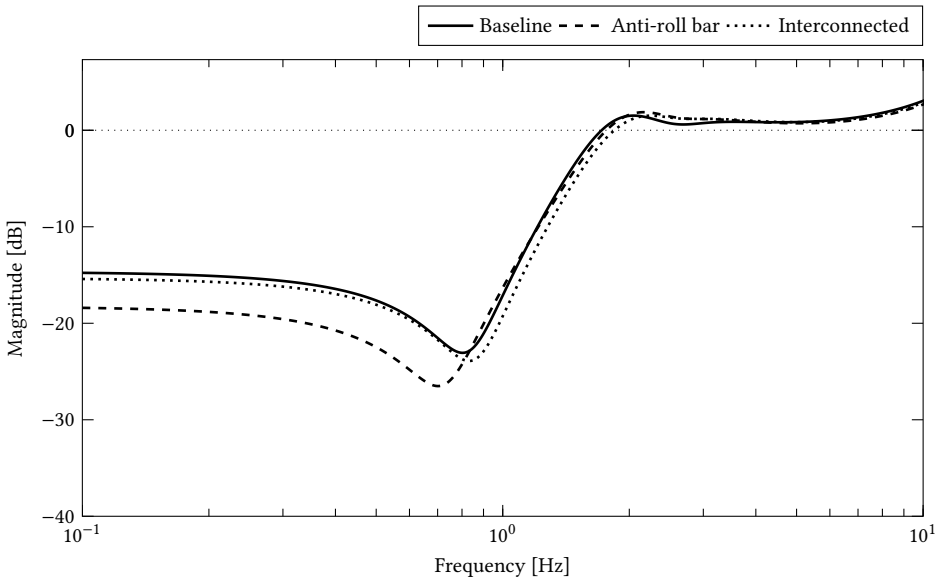

Figure 4.4: Frequency response showing suspension displacement at right front corner in response to road displacement

Figure 4.5 shows the comparison of tire compression for the three configurations. As the ability of the tire to absorb energy in the low frequency domain is almost negligible, only the plots in the midrange and high frequency domain are selected and compared. The distinction only appears in the 2 Hz to 3 Hz band, where the performance

of the configurations with modification can be considered as identical, but worse than the conventional suspension.

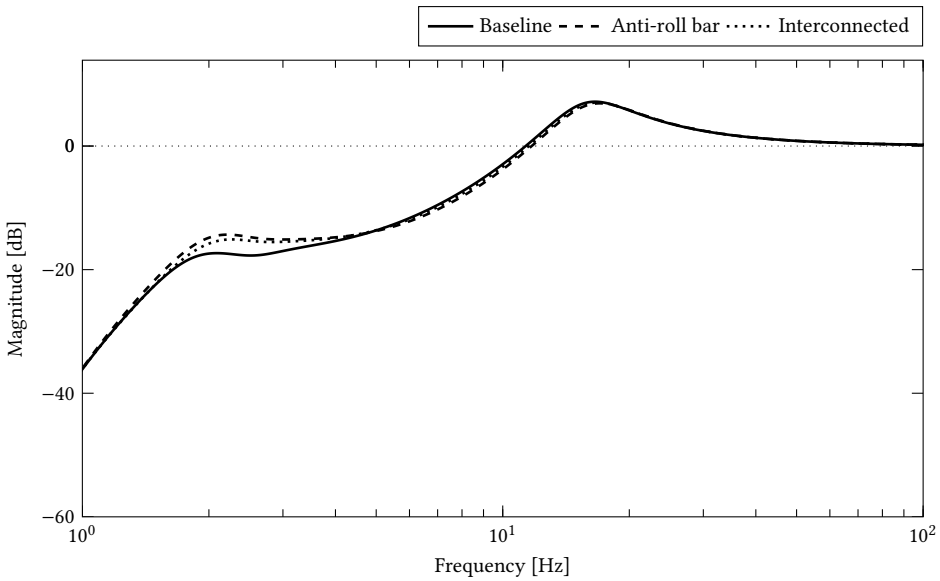

Figure 4.5: Frequency response showing tire compression at right front corner in response to road displacement

The frequency response of the three configurations to the rolling moment on the chassis offer little extra information, but are attached in Appendix B.1 for completeness.

Steady State Response

A steady state transfer function analysis is completed, and the results are shown in Tables 4.5, 4.6, and 4.7,

Table 4.5: Steady state results for the baseline configuration

No.	Output/Input	Gain
1	Front chassis motion/Front wheel bump	7.9772×10^{-1}
2	Front chassis motion/Roll moment	5.4709×10^{0}
3	Front suspension travel/Front wheel bump	-1.8457×10^{-1}
4	Front suspension travel/Roll moment	4.9940×10^{0}
5	Front tire compression/Front wheel bump	-1.7714×10^{-2}
6	Front tire compression/Roll moment	4.7687×10^{-1}
7	Rear tire compression/Front wheel bump	-9.7282×10^{-1}
8	Rear tire compression/Roll moment	6.4054×10^{-1}
9	Roll sensor/Front wheel bump	-7.4539×10^{-1}
10	Roll sensor/Roll moment	1.0942×10^{1}

Note: the roll motion and moment are scaled by characteristic values such that they are expressed in units of length, and thus all the steady state values are unitless ratios

The first noteworthy point is the comparison of the ratio of chassis rolling angle to the applied roll moment. The roll flexibility is particularly related to the cornering condition where a roll moment can be sustained.

Corresponding to the results obtained in the eigenvalue analysis, the roll stiffness increases in both the anti-roll bar and interconnected configurations. The ratio is 10.94 for the conventional configuration, 7.66 for the anti-roll bar configuration, and 8.04 for the interconnected configuration. Both the modified suspensions show increased roll stiffness, but the interconnected configuration provides a larger increase, even though the torsional stiffness of the anti-roll bar in the anti-roll bar configuration is twice as large.

Table 4.6: Steady state results for the interconnected configuration

No.	Output/Input	Gain
1	Front chassis motion/Front wheel bump	8.1043×10^{-1}
2	Front chassis motion/Roll moment	3.8304×10^{0}
3	Front suspension travel/Front wheel bump	-1.7141×10^{-1}
4	Front suspension travel/Roll moment	3.2971×10^{0}
5	Front tire compression/Front wheel bump	-1.8152×10^{-2}
6	Front tire compression/Roll moment	5.3334×10^{-1}
7	Rear tire compression/Front wheel bump	-9.7220×10^{-1}
8	Rear tire compression/Roll moment	5.6039×10^{-1}
9	Roll sensor/Front wheel bump	-7.1996×10^{-1}
10	Roll sensor/Roll moment	7.6609×10^{0}

Secondly, it is important to focus on the comparison of the ratio of chassis motion to wheel input, which can reflect the driving comfort directly. The results agree with the frequency response analysis. In the steady state analysis, the conventional suspension has the best performance to absorb the road disturbance with the ratio 0.798 compared with 0.810 for interconnected configuration and 0.855 for anti-roll bar configuration. This illustrates that the interconnected and anti-roll bar configurations both sacrifice some driving comfort compared with conventional suspension, but the penalty of the interconnected suspension is only 21.4% of the anti-roll bar model.

Table 4.7: Steady state results for front anti-roll bar configuration

No.	Output/Input	Gain
1	Front chassis motion/Front wheel bump	8.5456×10^{-1}
2	Front chassis motion/Roll moment	4.0235×10^{0}
3	Front suspension travel/Front wheel bump	-1.2209×10^{-1}
4	Front suspension travel/Roll moment	3.4031×10^{0}
5	Front tire compression/Front wheel bump	-2.3350×10^{-2}
6	Front tire compression/Roll moment	6.2042×10^{-1}
7	Rear tire compression/Front wheel bump	-9.6604×10^{-1}
8	Rear tire compression/Roll moment	4.6790×10^{-1}
9	Roll sensor/Front wheel bump	-6.3171×10^{-1}
10	Roll sensor/Roll moment	8.0470×10^{0}

Lastly, it is noteworthy to compare the front tire compression to rear tire compression in response to the roll moment. This is an important parameter for the roll stiffness distribution. The tables show that the conventional suspension makes this 0.477 : 0.641 or 43% : 57%. The anti-roll bar suspension has this ratio of 0.620 : 0.468 or 57% : 43% and the interconnected suspension has the ratio of 0.533 : 0.560 or 49% : 51%. The roll stiffness of the

conventional configuration is biased towards the rear while the anti-roll bar configuration is biased towards the front. It is close to being balanced in the interconnected configuration. This results show the anti-roll bar makes the roll stiffness have a forward tendency while the interconnected structure can ease this tendency and distribute the roll stiffness more evenly. This factor is important as the ratio of roll stiffness distribution can affect vehicle handling tendencies. Too much front stiffness leads to understeer, or poor cornering performance, while too much rear roll stiffness can lead to oversteer and yaw instability.

4.1.3 Results in Altair MotionView®

The results of obtained from linear simulation in EoM are compared with those developed in Altair MotionView®. The basic structures of the three configurations are almost same as those in EoM; all the bodies are effectively the same. For brevity, the eigenvalue results of Altair MotionView® are attached in Appendix B.2. Among the oscillatory motions, four high and three low frequency oscillatory modes appear, and the values very nearly the same as those predicted in EoM. This comparison improves confidence in the reliability and accuracy of the linear simulation.

4.2 Non-linear Simulation

To better explore the characteristics of the three configurations, a non-linear time history analysis, which is more consistent with the real condition, is also conducted.

First, a step input signal is applied on the vehicle. In response to this step signal, the static deflection of the vehicle is available after a drastic vehicle oscillation. The ratios of the motion of different vehicle components in response to the step signal are calculated to compare with the steady state gains predicted in EoM.

Through the frequency response of the three configurations in EoM, some obvious distinctions appear in some specific points in the frequency domain. So, some sinusoidal signals of differing frequency are next selected to be the road disturbance. The ratios of the motions of the vehicle components to those sinusoidal signals are compared to the frequency response in EoM. It is noticeable that the logarithmic data in EoM is required to be transformed from units of decibels back into percentages.

In addition, random road profiles are employed to test the vehicle performance when confronting different levels of road roughness, especially the off-road condition. The code that is used to generate the random road, attached in the Appendix A.1 at the end of this thesis, is prepared in MATLAB®.

4.2.1 Step Signal Results

Definition

In engineering applications, the step signal is a frequently encountered function whose value changes abruptly in the time domain. The unit step signal, also called the Heaviside step signal, can be considered as a specific example.

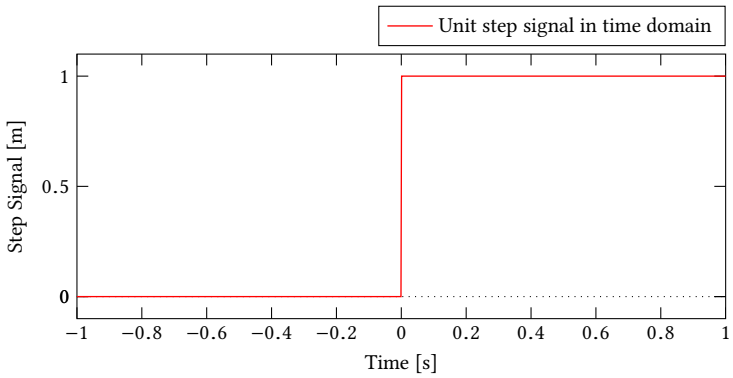

Figure 4.6: Unit step signal in time domain

As shown in Figure 4.6, the unit step signal $u(t)$ can be defined as:

$$u(t) = \begin{cases} 0, & t < 0 \\ 1, & t \geq 0 \end{cases} \tag{4.10}$$

where u is function of time t, and u has value of zero when time is negative (before 'flipping the switch'), and value of one when time is positive. With the Laplace transform function:

$$F(s) = \int_0^\infty e^{-st} f(t) dt \tag{4.11}$$

The expression of the unit step signal in the frequency domain can be expressed as:

$$\mathcal{L}(u(t)) = 1/s \tag{4.12}$$

where s is the complex frequency parameter.

Steady State Response to Step Signal

From Figure 4.7, the step signal can be considered as a continuous function in frequency domain, the ratios of vehicle ultimate static state to the amplitude of the step signal are compared with the steady state gains. In this

case, the forward velocity of the vehicle is modified to be 0 m/s in both softwares.

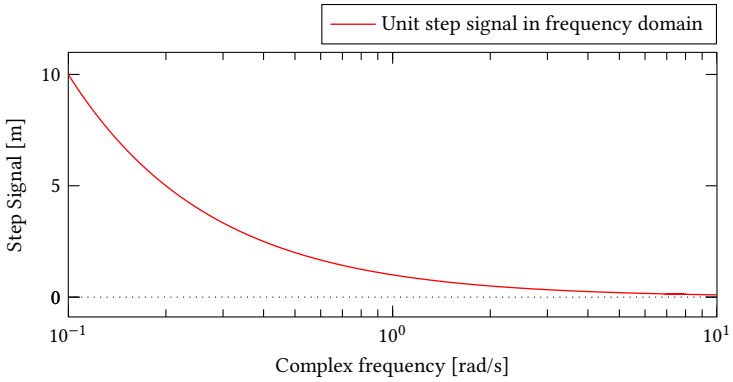

Figure 4.7: Unit step signal in frequency domain

Tables 4.8, 4.9, and 4.10 show the static ratio of chassis motion, suspension travel, and tire compression to the step signal applied on the right front wheel.

Table 4.8: The ratio of vehicle chassis motion to the step signal in the steady state

Software	Conventional	Anti-roll	Interconnected
Altair	8.4800×10^{-1}	9.0000×10^{-1}	8.4300×10^{-1}
EoM	8.2500×10^{-1}	8.7800×10^{-1}	8.2600×10^{-1}

Notes: measured with the sensor of the chassis located adjacent to the right front wheel.

Table 4.9: The ratio of vehicle suspension travel to the step signal in the steady state

Software	Conventional	Anti-roll	Interconnected
Altair	-1.5900×10^{-1}	-1.0400×10^{-1}	-1.5800×10^{-1}
EoM	-1.3800×10^{-1}	-8.0800×10^{-2}	-1.4400×10^{-1}

Notes: measured with the sensor of the chassis motion located in the center of the right front wheel.

Table 4.10: The ratio of vehicle tire compression to the step signal in the steady state

Software	Conventional	Anti-roll	Interconnected
Altair	-1.4800×10^{-2}	-1.8300×10^{-2}	-1.5000×10^{-2}
EoM	-1.3300×10^{-2}	-1.5700×10^{-2}	-1.3400×10^{-2}

Notes: measured with the sensor of the chassis motion located between the right front wheel and the ground.

To more clearly illustrate the difference between the three configurations, the ratios are plotted in the time domain in Figures 4.8, 4.9, and 4.10 for all configurations. The step input signals are used as a baseline.

From Figure 4.8 and Table 4.8, both the conventional and interconnected suspensions perform better than the anti-roll bar configuration with a ratio 90%; this result corresponds to the outcome predicted using EoM. A noteworthy point is that the results show the interconnected configuration even has a little advantage over the conventional suspension, which is not indicated in the linear EoM results, but there is little difference otherwise.

Based on Figure 4.9 and Table 4.9, the suspension travel, with a ratio 10.4%, has a relatively bad performance in anti-roll bar configuration, while the other two configurations are about the same. This result also agrees with that predicted in EoM. But, analogous to the analysis of the chassis vertical motion, the ratios of interconnected and conventional configurations appear to show little difference.

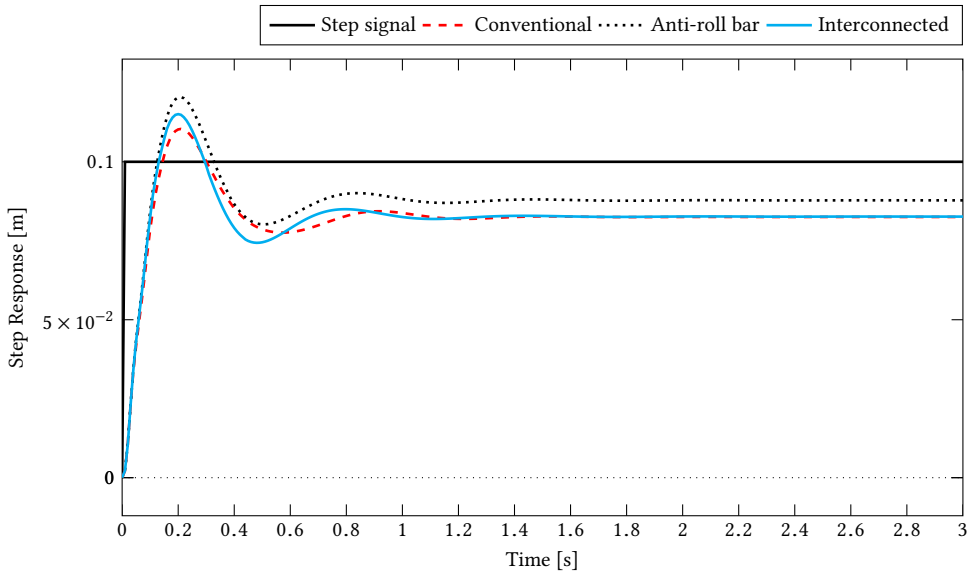

Figure 4.8: The chassis vertical motion in response to a step signal

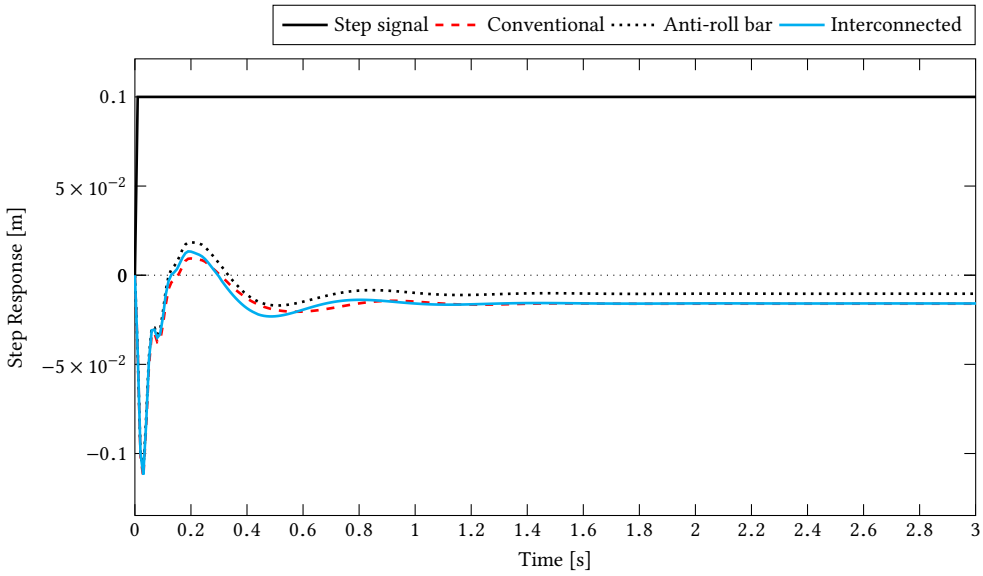

Figure 4.9: The suspension travel in response to a step signal

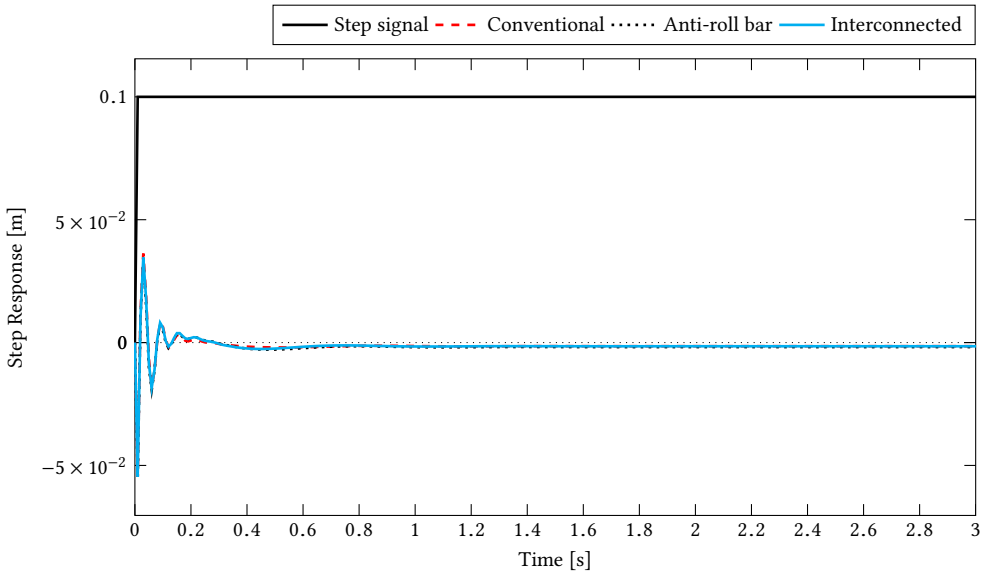

Figure 4.10: The tire compression in response to a step signal

At last, the results in Figure 4.10 and Table 4.10 show the ratio of tire compression to the step signal for the three configurations. The linear and non-linear results are very consistent. After a high frequency oscillation, the tire compression turns constant. The ratios of the final tire compression to the road displacement are in the range between 0.013 and 0.015 in all three configurations. No obvious difference appears between the three configurations, as expected, because the tire does not play an important role in the low and midrange frequency

domain.

4.2.2 Non-linear Frequency Response

With the widely used fast Fourier transform (FFT), it is possible to find a comprehensive description of a mathematical function or a signal in its frequency domain. As the frequency response analysis results from EoM show, the performance of different vehicle component motions responding to a road disturbance can be easily obtained in the frequency domain. In this section, a comparison is made between the linear and non-linear simulations in regards to the response to a sinusoidal input. Of course, it is not mathematically possible to conduct a frequency response analysis in the same manner in a non-linear set of equations. As a result, a time domain response to a sine wave input at a fixed frequency is computed for the non-linear model, and repeated with varying frequencies. After some initial transients have decayed, the maximum amplitude of the response signal is found from the time domain, and the ratio this amplitude to the input amplitude is compared with the appropriate point on the linear frequency response curves found in EoM.

Response to Sinusoidal Road

In the frequency analysis in EoM, the domain can be divided into three ranges: (a) low frequency, from 0 Hz to 1 Hz; (b) midrange, between 1 Hz and 10 Hz; (3) high frequency, 10 Hz to 100 Hz. Based on the outcomes in EoM, the distinctions between the three suspension configurations primarily happen in the low and midrange frequency regions. To compare with the frequency domain analysis, three signals with frequency 0.5 Hz, 1 Hz and 10 Hz are selected. In this test, the sinusoidal signals are applied as the motions of the ground under the right front wheel for the all three configurations.

In order to allow a comparison, the results of the linear frequency response analysis are transferred from a logarithmic scale to a percentage with the function:

$$y = \left(\frac{x}{20}\right)^{10} \tag{4.13}$$

where x, y are the numbers in the logarithmic scale and the equivalent percentage, respectively.

According to Table 4.12, both the conventional and interconnected configurations have a better performance than the anti-roll bar in response to a 0.5 Hz and 1 Hz sinusoidal signal. This result clearly shows that the interconnected structure can reduce the driving comfort penalty when compared with the anti-roll bar configuration. When the frequency reaches 10 Hz, the chassis motions of the three configurations show little difference, which can be explained as the energy of the road disturbance is absorbed by the tires in the high frequency range. As shown in Table 4.11, the results obtained in EoM also agree with the trends identified in the non-linear simulations.

Table 4.11: The ratio of vehicle chassis motion to sinusoidal input signal in EoM

Frequency [Hz]	Conventional	Anti-roll	Interconnected
5.0000×10^{-1}	9.1400×10^{-1}	9.6000×10^{-1}	8.9000×10^{-1}
1.0000×10^{0}	1.1300×10^{0}	1.1730×10^{0}	1.0920×10^{0}
1.0000×10^{1}	1.7200×10^{-1}	1.7300×10^{-1}	1.7200×10^{-1}

Table 4.12: The ratio of vehicle chassis motion to sinusoidal input signal in Altair

Frequency [Hz]	Conventional	Anti-roll	Interconnected
5.0000×10^{-1}	8.8500×10^{-1}	9.4100×10^{-1}	8.8300×10^{-1}
1.0000×10^{0}	1.0640×10^{0}	1.1350×10^{0}	1.0650×10^{0}
1.0000×10^{1}	1.7500×10^{-1}	1.7500×10^{-1}	1.7500×10^{-1}

Note: the time range is set to be 10 s and sampling frequency is 100 Hz

The ratios of the suspension travel for three configurations in response to the sinusoidal signal are listed in the Tables 4.13 and 4.14. As expected, when confronted with the 0.5 Hz road disturbance, both the interconnected and conventional suspensions have a longer suspension travel, which indicates a better capacity to absorb energy. When the frequency of input increases to 1 Hz, the suspension travel of interconenncted configuration decreases and is worse than the other two suspensions. The distinction amongst the three configurations grows smaller and smaller as the frequency increases. The ratios of the suspension travel are almost identical with a 10 Hz sinusoidal input signal.

Table 4.13: The ratio of suspension travel to sinusoidal input signal in EoM

Frequency [Hz]	Conventional	Anti-roll	Interconnected
5.0000×10^{-1}	8.9500×10^{-2}	4.5100×10^{-2}	9.8700×10^{-2}
1.0000×10^{0}	2.4000×10^{-1}	2.1600×10^{-1}	1.4400×10^{-1}
1.0000×10^{1}	1.4120×10^{0}	1.3500×10^{0}	1.3820×10^{0}

Table 4.14: The ratio of suspension travel to sinusoidal input signal in Altair

Frequency [Hz]	Conventional	Anti-roll	Interconnected
5.0000×10^{-1}	1.0600×10^{-1}	5.8300×10^{-2}	1.1300×10^{-1}
1.0000×10^{0}	1.9000×10^{-1}	1.7800×10^{-1}	1.1900×10^{-1}
1.0000×10^{1}	1.3750×10^{0}	1.3450×10^{0}	1.3740×10^{0}

Note: the time range is set to be 10 s and sampling frequency is 100 Hz

In Tables 4.15 and 4.16, the results show that the tire compression from the sinusoidal signal shows no significant difference amongst the three configurations. The result is reasonable because while the tire plays an important role to absorb road energy instead of generating chassis motion or suspension travel, significant tire compression usually occurs only as frequency increases.

Table 4.15: The ratio of tire compression to sinusoidal input in EoM

Frequency [Hz]	Conventional	Anti-roll	Interconnected
5.0000×10^{-1}	8.1700×10^{-3}	9.7600×10^{-3}	8.0100×10^{-3}
1.0000×10^{0}	2.8200×10^{-2}	3.1100×10^{-2}	2.5600×10^{-2}
1.0000×10^{1}	7.0600×10^{-1}	6.4100×10^{-1}	6.7200×10^{-1}

Table 4.16: The ratio of tire compression to sinusoidal signal in Altair

Frequency [Hz]	Conventional	Anti-roll	Interconnected
5.0000×10^{-1}	9.3800×10^{-3}	1.1680×10^{-2}	9.2720×10^{-3}
1.0000×10^{0}	2.5000×10^{-2}	3.0100×10^{-2}	2.2100×10^{-2}
1.0000×10^{1}	7.0000×10^{-1}	6.3500×10^{-1}	6.5000×10^{-1}

Notes: The time range is set to be 10 s and sampling frequency is 100 Hz

4.2.3 Random Road Response

To further explore the performance and make a more clear comparison of the three suspension models, simulations are conducted utilizing random road profiles, as have been introduced in Chapter 2. This simulation is done to examine the performance of the different models when confronted with a wide range of road roughness classes. Vehicle motions such as twist, roll, pitch and bounce, as presented in Chapter 2, are produced according to the combinations of random roads applied on the wheels. In this analysis, the compression forces between the tire and the ground, generated as a result of the random road disturbance, are extracted and analyzed for all three configurations.

In the previous analyses, both linear and non-linear simulations have been done. The analysis in Altair MotionView® in response to the step input signal and sinusoidal signal, shows consistency with the frequency response analysis and steady state gains in EoM. In this analysis, two short sample roads will be used to show the consistency of the linear and non-linear simulations using a single configuration. Following this comparison, the non-linear simulations only will be used to evaluate the performance of the three configurations to multiple random roads.

Grip, defined as the capacity of the vehicle to 'hold' the ground, is always considered as an important factor to describe the vehicle handling and control. When considering tire grip, it is important to recognize that the contact force contains both a fluctuating component due to disturbances, as well as a steady component due to vehicle weight. In general, large fluctuations in the tire compressive forces tend to reduce grip, as it reduces the value of the minimum contact force between the tire and the ground. As a result a mathematical tool called *standard deviation* is introduced to complete the comparison of grip for the three configurations. The frequency distributions of the force are plotted in response to the kinds of random road as well.

Random Road Generation

As introduced in Chapter 2, the classification of the longitudinal road profile, which shows the design grades and roughness, is based on the ISO 8606 standard, as determined by the power spectral density(PSD). In this thesis, a function is developed in MATLAB® to produce classes of random roads according to their PSD.

During the simulation, a road profile of length is 100 m is selected, a velocity of 10 m/s given to the vehicle model. The sampling frequency is set at 512 Hz. The road profile is classified by an integer from 3–9, which corresponds to the transitions between ISO classes A–H. For example, class 3 is equal to the transition between A and B class, which is smooth ($h_{\max} \approx \pm 15$ mm) and class 9 refers to the G-H transition, which is rough ($h_{\max} \approx \pm 100$ mm).

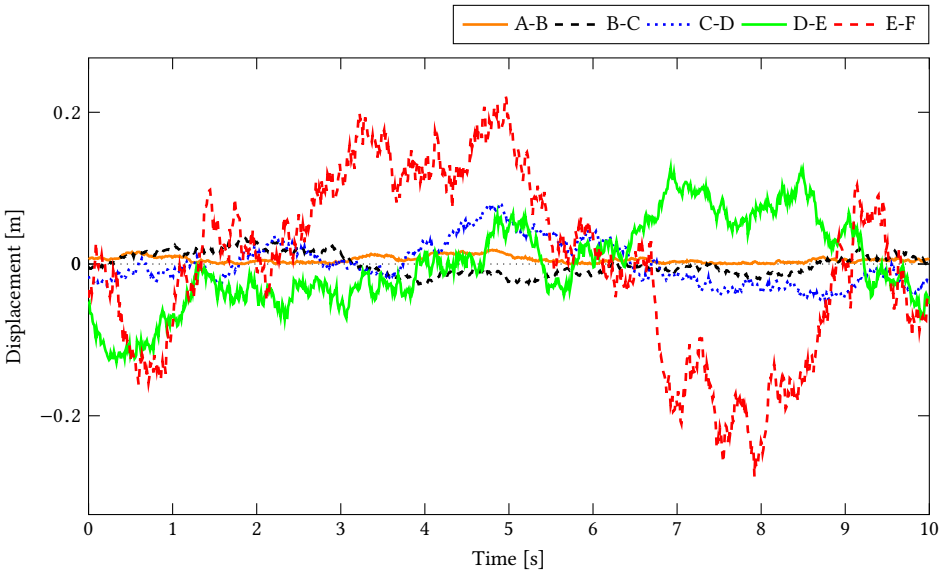

Figure 4.11: Random road time-history classification

The output of this random road function includes both the time history plots shown in Figure 4.11 and the PSD plot shown in Figure 4.12. These random roads are used as the inputs of the Baja full vehicle MotionView® model.

The PSD plot describes the strength of the variations (energy) as a function of frequency. Figure 4.12 shows that although the amplitude increases with the level of the random road, the main oscillations remain concentrated in the range 0.01 Hz to 1 Hz. In this analysis, only level 3–6 random roads are considered, as all three vehicle configurations begin to lose ground contact under the effect of level 7 or higher random road.

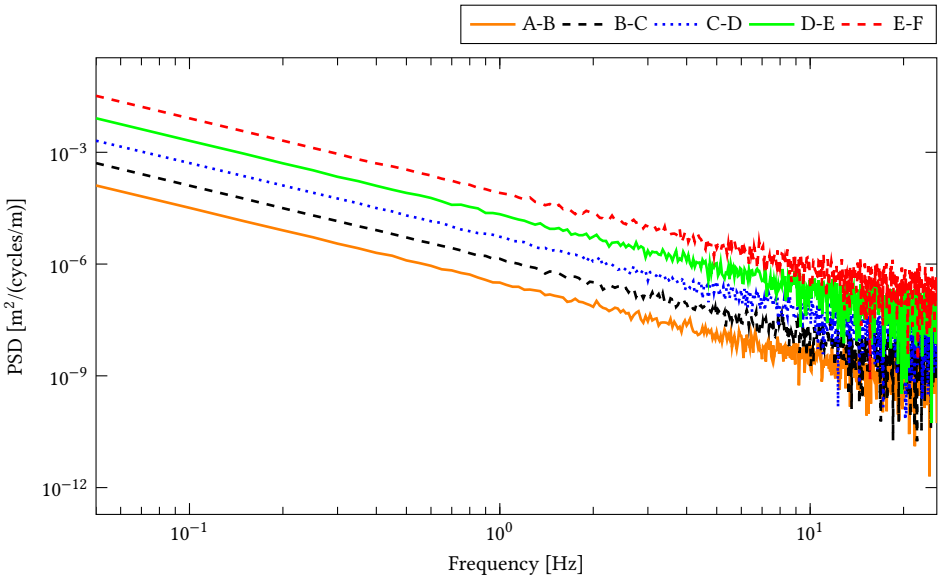

Figure 4.12: Random road frequency-domain classification

Comparison of Linear and Non-linear Simulations Time History

As noted by Sullivan[?], the response of a non-linear system to a sufficiently small input signal with will appear linear. To demonstrate the consistency of the linear and non-linear models in this project, a very smooth road is applied on the front right wheel in both the linear and non-linear interconnected models. The chassis response is shown in Figure 4.13, which clearly shows that, as expected, the linear and non-linear models behave almost identically in this scenario. As a comparison, a level 5 random road is also utilized to test the difference between the linear and non-linear models.

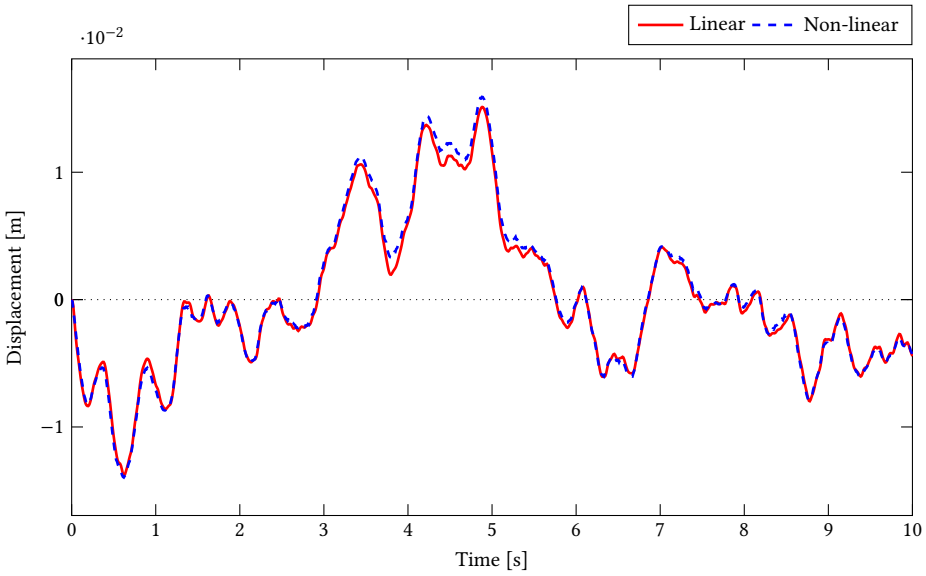

Figure 4.13: Chassis vertical displacement with level 1 random road

The displacement of the chassis vertical motion is shown in Figure 4.14. With the level 5 random road, although there is still a strong similarity, an obvious distinction now exists between the linear and non-linear model results. Contrasting the simulation results using the very smooth road illustrates the difference in behavior between the linear and non-linear models.

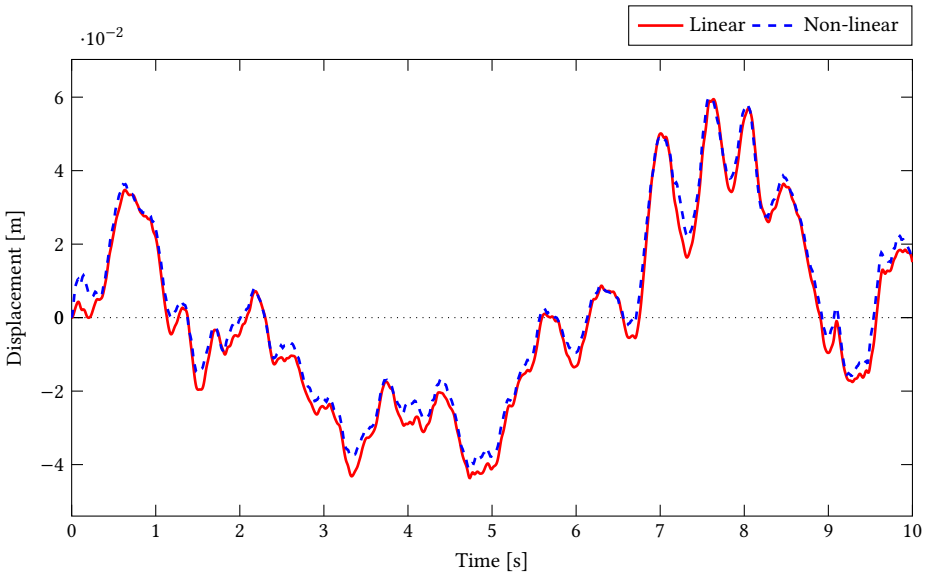

Figure 4.14: Chassis vertical displacement with level 5 random road

Standard Deviation

In statistics, the standard deviation can be used to quantify the amount of variation or dispersion of an array of data values. In this chapter, the tire force can be considered as a set of discrete data values, so the standard deviation can be expressed as:

$$\sigma_{\text{sd}} = \sqrt{\frac{1}{N}[(F_1 - F_0)^2 + (F_2 - F_0)^2 + \ldots + (F_N - F_0)^2]} \tag{4.14}$$

where:

$$F_0 = \frac{1}{N}(F_1 + F_2 + \ldots + F_N) \tag{4.15}$$

i.e., σ_{sd} is the standard deviation, N is the number of data samples, F_N is the Nth data point of the tire force, and F_0 is the mean value of all the samples.

In response to the random road, the tire force of the three configurations varies over time. The smaller the variation is, the larger the tire grip is. Based on the standard deviation, the grip of each configuration can be assessed.

Level 3 Random Road

As shown in Figure 4.15, the amplitude of the level 3 random road, applied on the right front wheel of the three configurations, is between -0.02 and 0.015 meters. Based on the PSD, the frequency is mainly concentrated in the range 0.01 Hz to 1 Hz. Compared with the other random roads, the level 3 random road is the mildest one. Ten seconds of the random road simulation are considered.

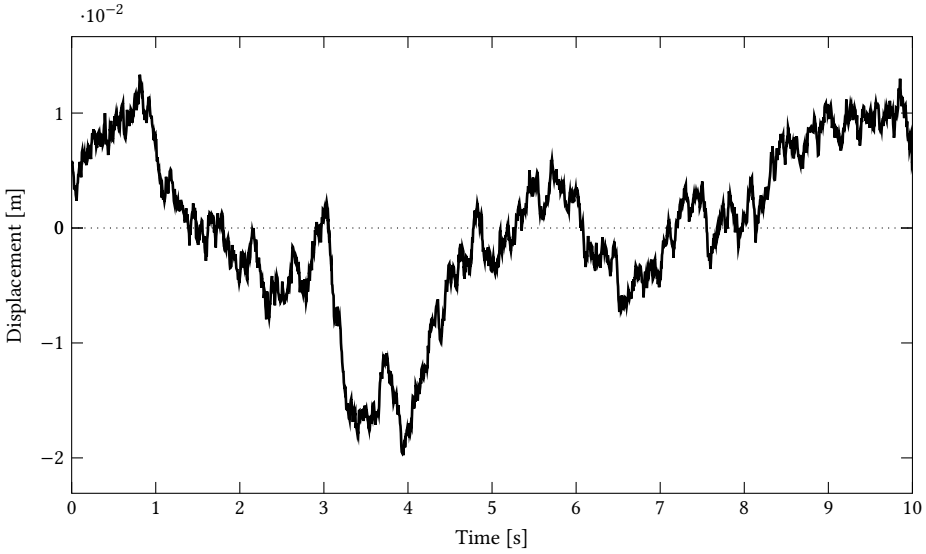

Figure 4.15: Level 3 random road

Figure 4.16 shows the force between front right tire and the ground for the three configurations. It clearly illustrates that all the models obtain ideal grip as the compression force, having an oscillation between 500 N and 700 N, can be considered as relatively stable. The smallest force value of about 350 N is reached around 8.3 s, and although this force strays from the regular values, it is reasonable because the contact between tire and ground is maintained.

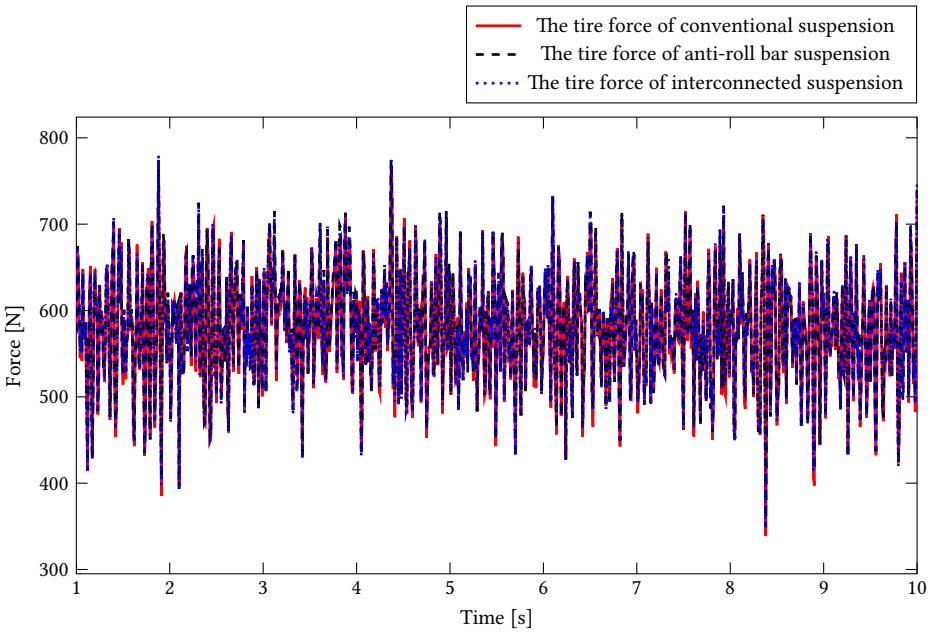

Figure 4.16: The tire force of three configurations in response to the level 3 random road

The standard deviations and mean values of the force between the front right tire and ground are shown in Table 4.17 for the three configurations. The mean values of the compression force are 578.99 N, 580.85 N and 581.03 N, for the conventional, anti-roll bar and interconnected configurations, respectively. The standard deviations are 64.561 N, 63.847 N and 64.303 N for the conventional, anti-roll bar and interconected suspensions. The interconnected suspension has a very slightly better performance to keep the wheel contacting the ground than the conventional suspension, while is not as good as anti-roll bar configuration.

Table 4.17: The standard deviations and mean values of the three configurations in response to the level 3 random road

Method	Conventional	Anti-roll	Interconnected
Standard deviation	6.4561×10^1	6.3847×10^1	6.4303×10^1
Mean value	5.7899×10^2	5.8085×10^2	5.8103×10^2

Level 4 Random Road

The level 4 random road is shown in Figure 4.17. The peak point of about 0.04 m is reached at around 7 s and the deep point of about −0.02 m around 5.2 s; the slope of this road increases evidently over that of the level 3 road.

The compression forces between the tire and the ground in response to a level 4 random road are shown in Figure 4.18 for the three configurations. They primarily oscillate in the range from 350 N to 800 N. At 7 s the smallest force of about 200 N occurs; it is consistent with the drastic bump leading to an upward motion in Figure 4.17. Overall, the three configurations never lose grip and keep ground contact when faced with level 4 random road.

Table 4.18 describes the mean values and standard deviations of the front right wheel force with ground. The mean values for the three configurations are almost identical (as expected). The difference in standard deviation for the level 4 random road reflects the same trend when compared with the results for the level 3 road. With the value 128.87 N, the anti-roll bar configuration shows its advantage over both the conventional and interconected ones, with values of 130.93 N and 129.51 N, respectively. In this case, the anti-roll bar also provides a more stable grip than the others and the interconnected configuration has a slight advantage over the conventional one.

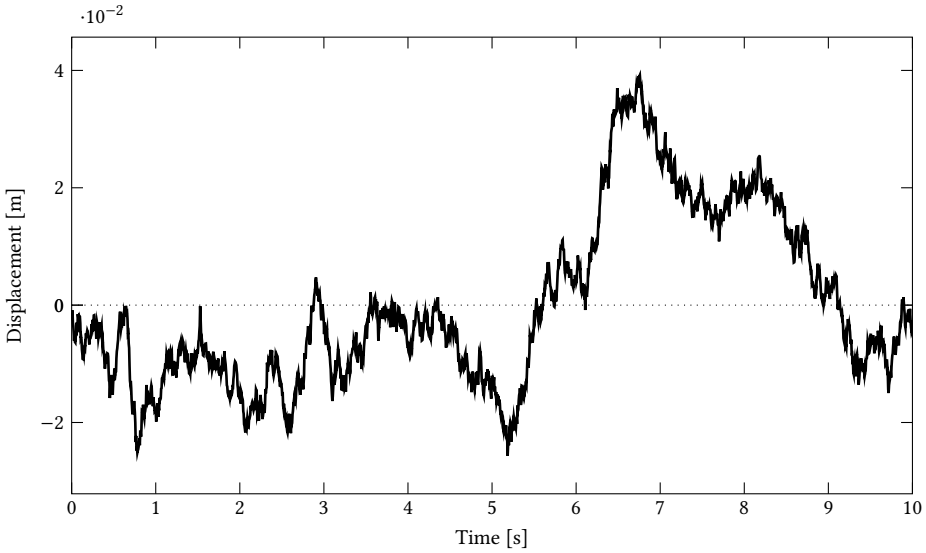

Figure 4.17: Level 4 random road

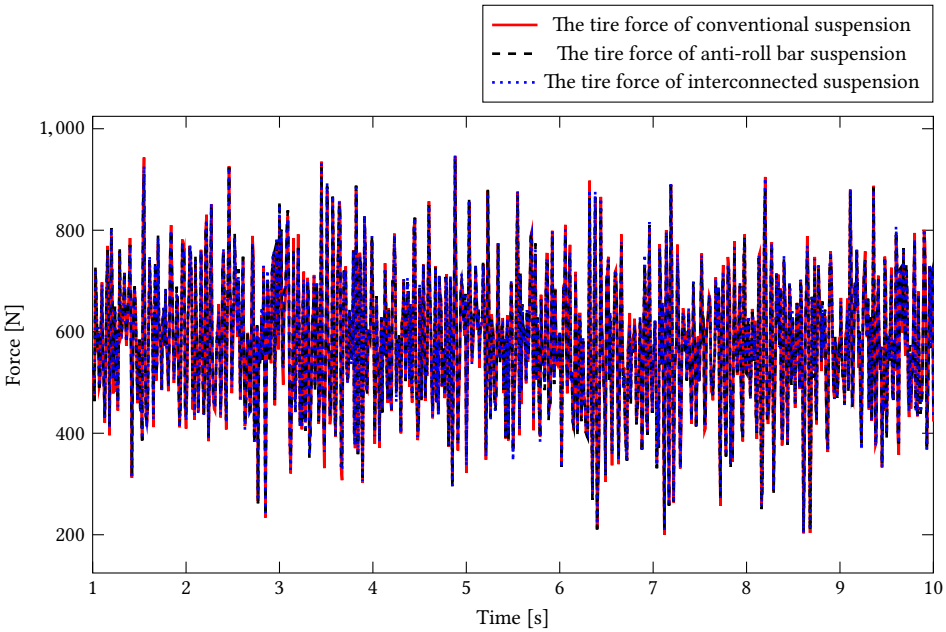

Figure 4.18: The tire force of three configurations in respond to the level 4 random road

Table 4.18: The standard deviations and mean values of the three configurations in response to the level 4 random road

Method	Conventional	Anti-roll	Interconnected
Standard deviation	1.3093×10^2	1.2887×10^2	1.2951×10^2
Mean value	5.7659×10^2	5.7760×10^2	5.7846×10^2

Level 5 Random Road

As shown in Figure 4.19, the amplitude of the level 5 random road applied on the right front tire varies from −0.08 m at 3.2 s to 0.05 m at 5.5 s. The resulting compression force between the tire and the ground for the three configurations is shown in Figure 4.20. When compared with the results in response to the level 3 and level 4 random roads, the compression force shows severe oscillations from about 200 N to 1000 N. It is noticeable that the forces reach zero at some points, which means the vehicle leaves the ground and loses grip; ideally this condition should be avoided. Figure 4.20 shows that most of the zero-force points happen on the conventional suspension, which indicates that the configurations with modification provide assistance to prevent the vehicle losing grip.

In Table 4.19, the standard deviation and mean value of force in response to the level 5 random road for the three configurations are listed. The standard deviation results of the level 5 random road correspond to the earlier results. The anti-roll bar configuration holds the first place with 128.87 N to offer a more stable grip, while

interconnected configuration shows a slight advantage over the conventional one.

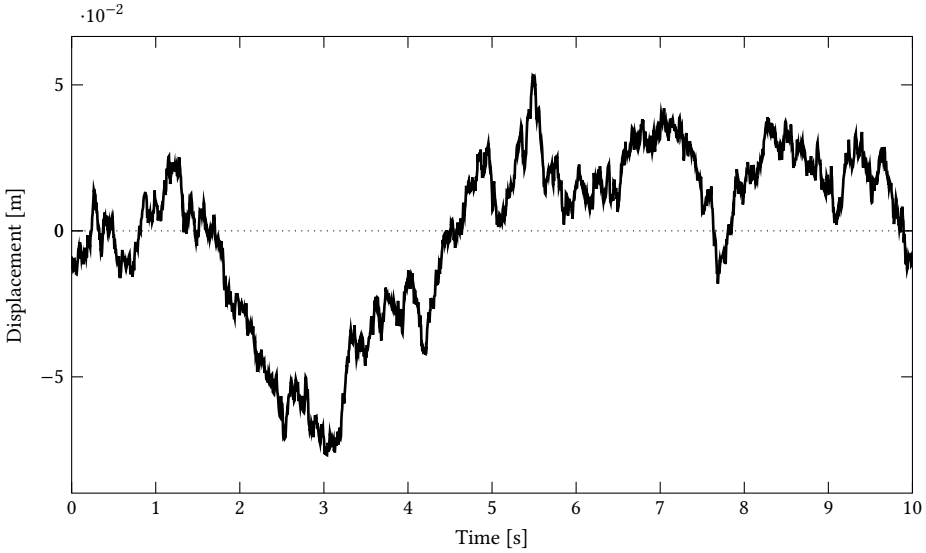

Figure 4.19: Level 5 random road

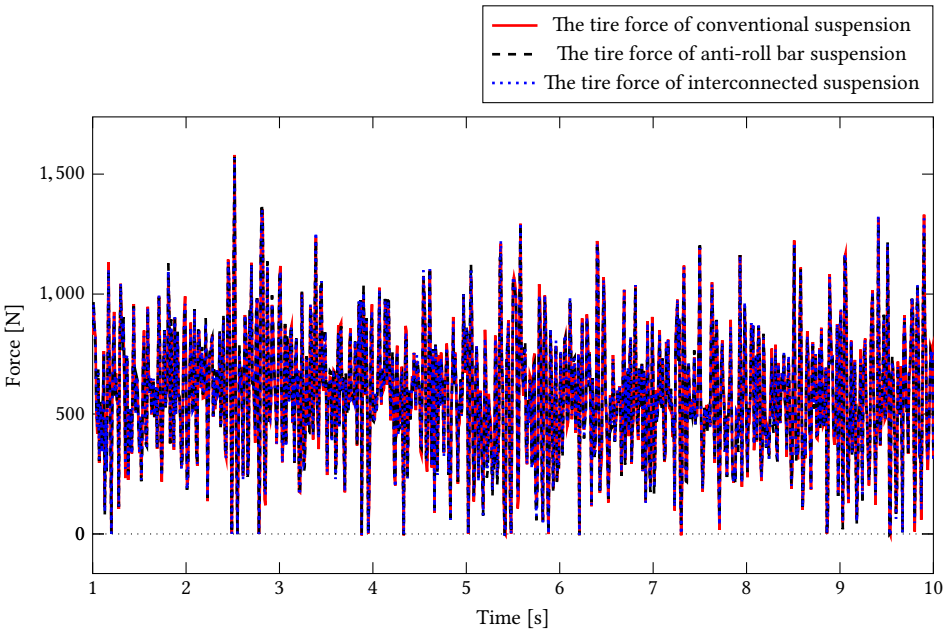

Figure 4.20: The tire force of three configurations in respond to the level 5 random road

Table 4.19: The standard deviations and mean values of the three configurations in reponse to the level 5 random road

Method	Conventional	Anti-roll	Interconnected
Standard deviation	2.6194×10^2	2.5898×10^2	2.6049×10^2
Mean value	5.8098×10^2	5.8156×10^2	5.8248×10^2

Level 6 Random Road

Compared with the level 3, 4 and 5 random roads, the amplitude of the level 6 random road increases substantially. The peak of 0.1 m and bottom of −0.18 m are reached at 4 s and 1 s, as shown in Figure 4.21.

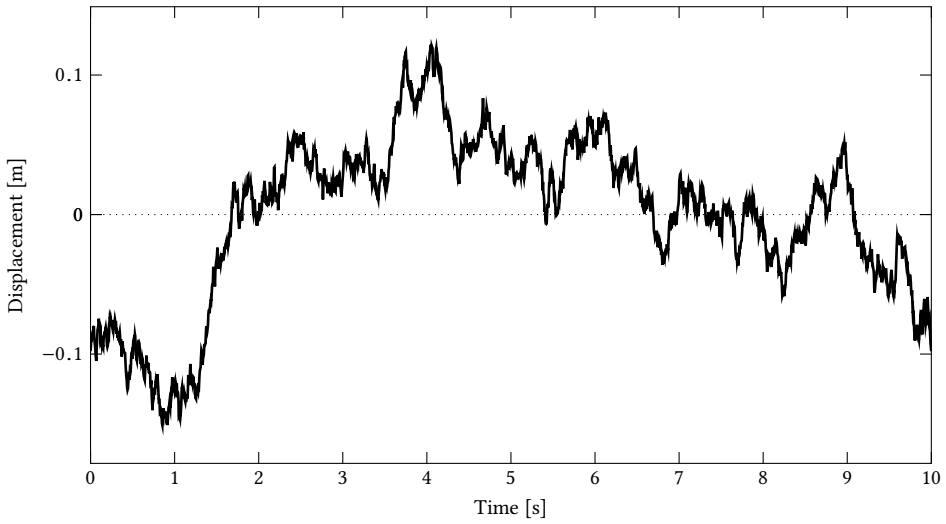

Figure 4.21: Level 6 random road

The compression force of the right front tire with ground is shown in Figure 4.22 for the three configurations. As a result of the rough road, drastic oscillations happen with several zero-force points and the largest forces are up to 2000 N, which means the vehicles have a significant wheel motions. In this case, all the three configurations tend to leave the ground and lose grip. It should be considered that the Baja vehicle is designed for severe off-road conditions, and it is quite important that it can overcome the most severe random road possible. Based on the dynamic animations generated by MotionView®, all the vehicle models can still maintain an upright condition on the level 6 road.

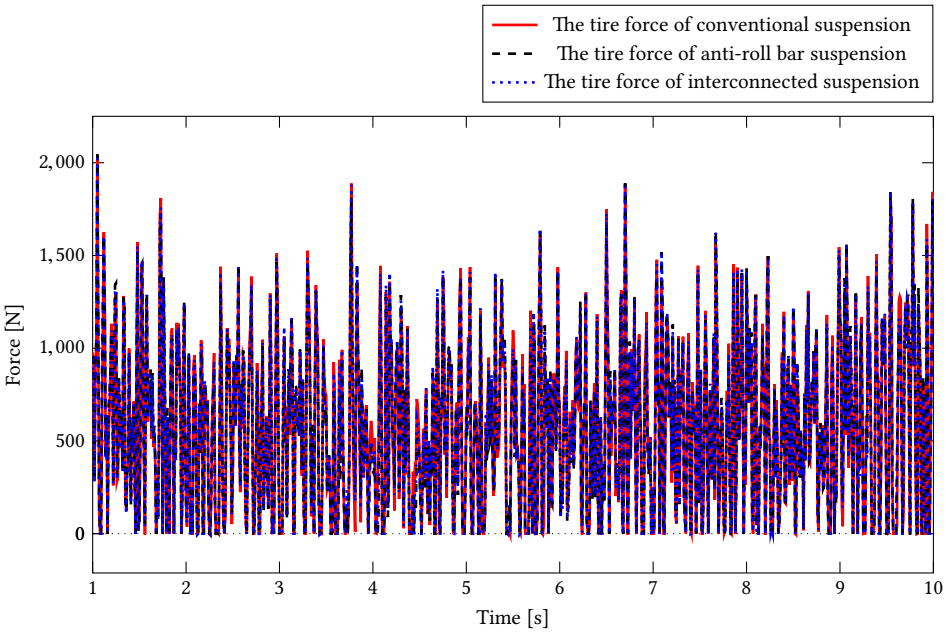

Figure 4.22: The tire force of the three configurations in response to the level 6 random road

As listed in Table 4.20, the mean values are 571.90 N, 568.82 N and 572.29 N for conventional, anti-roll bar and interconnected configurations, respectively. Compared with the results above, the mean values of tire forces decrease significantly. It is highly possible that the drastic wheel-hop leads to the results because of the loss of grip. The standard deviation still basically corresponds to the results in the lower level random road. The anti-roll bar suspension still performs the best in this comparison with a value 442.46 N while the others measure 447.90 N and 445.76 N for conventional and interconnected configurations, respectively.

Table 4.20: The standard deviations and mean values of the three configurations in response to the level 6 random road

Method	Conventional	Anti-roll	Interconnected
Standard deviation	4.4790×10^2	4.4246×10^2	4.4576×10^2
Mean value	5.7190×10^2	5.6882×10^2	5.7229×10^2

Finally, the dashed line charts of standard deviation and mean value of tire force are shown in Figure 4.23 and 4.24. It clearly illustrates that the standard deviations of three configurations all grow larger with the increasing level of random roads, and both the anti-roll bar and interconnected configurations do a better job than the conventional configuration.

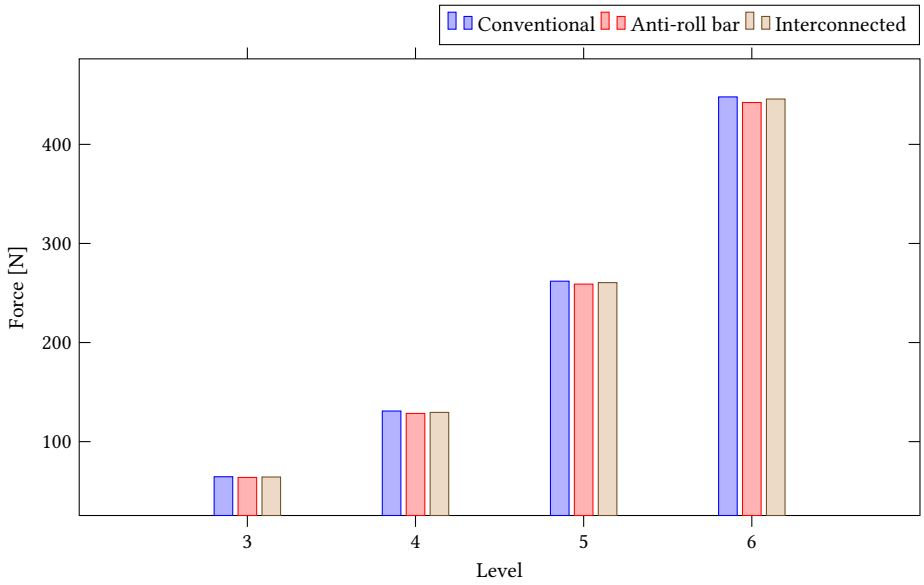

Figure 4.23: Standard deviation

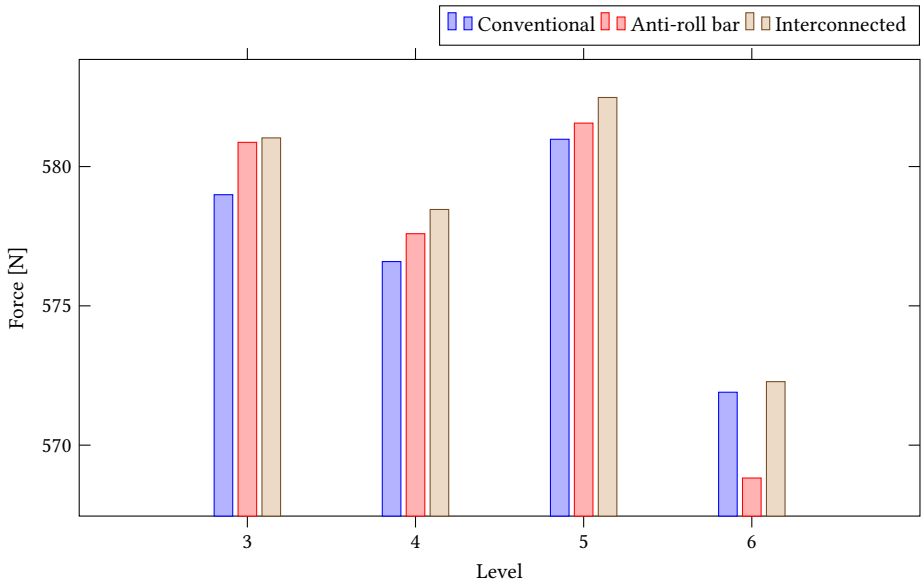

Figure 4.24: Mean value

The anti-roll bar suspension clearly provides a smaller deviation in the compression force than the others for the level 3, 4, and 5 random roads, but the distinction is unexpectedly small. For the level 6 road, the results appear consistent, but the large number of instances where the vehicle is not in contact with the road clouds the results somewhat.

Finally, as an alternative to using the standard deviation as a means of assessing the tire grip, an integration to

compute the area under the PSD curve of the resulting tire force was also explored. In general, the trends agree with the results obtained from the standard deviation calculations, but it was difficult to draw any meaningful conclusions from the PSD curves themselves. The results are shown in the Appendix B.3.

Frequency Distribution

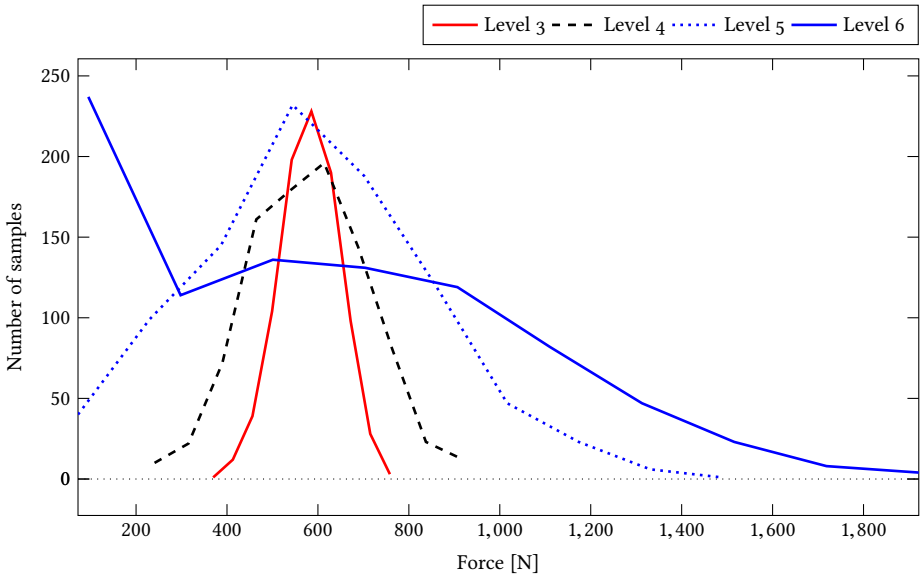

Figure 4.25: The frequency distribution of tire force for different random roads

The frequency distribution of tire compression force in response to the different random roads is shown in Figure 4.25, the force for the level 3 road mainly concentrates in the range of 400 N to 800 N and the most frequent force is around 590 N. Between 200 N and 900 N, the range for level 4 random road tends to be wider and the force frequency distribution becomes more dispersed. For the level 5 random road, the zero-force points begin to appear and the peak of the distribution happens around 560 N. Finally, the distribution becomes more scattered and the majority of the forces are zero-force points for the level 6 random road.

4.3 Summary

In this chapter, both linear and non-linear simulations of a conventional, an anti-roll bar and an interconnected suspension configuration are presented. Two softwares, Altair MotionView® and EoM are employed to complete the analysis. All the configurations use models with thirteen degrees of freedom.

In the linear simulation, based on the modal analysis in EoM, both the anti-roll bar and the interconnected suspension configurations demonstrate the predicted increased roll stiffness. The modal analysis shows little

distinction between the two modified configurations. With a road disturbance applied on the right front wheel, the frequency response result shows that the interconnected suspension can improve the roll stiffness and provide a longer suspension travel with less comfort penalty than the anti-roll bar configuration. In the steady state gain analysis, it is confirmed that the interconnected suspension can provide a larger roll stiffness even if the stiffness of its anti-roll bar is only half of that of anti-roll bar configuration. Meanwhile, the interconnected suspension can distribute the roll stiffness more evenly with the front and rear tire compression force ratio almost $1:1$. The modal analysis conducted in Altair MotionView® also supports the results obtained from EoM.

In the non-linear simulation completed in Altair MotionView®, a step signal disturbance is applied on the right front wheel. The time domain response is allowed to reach steady state, and the final values are retreived. The results are consistent with the results in linear steady state gain analysis; the interconnected suspension can increase the roll stiffness with less comfort penalty than the anti-roll bar configuration. Then three sinusoidal signal disturbances with 0.5 Hz, 1 Hz, and 10 Hz are employed. The magnitude of the time domain response is found after the transients have disappeared. The result is compared to the linear frequency response, and shows high agreement. At last, four random roads are considered and the results show the interconnected suspension can increase the tire grip, but less than the anti-roll configuration, according the standard deviation of the right front wheel compression force. However, only a very small difference was detected between the three configurations, in contrast to expectations.

Chapter 5

Conclusions, Contribution, and Recommendations

5.1 Conclusions

This project aimed to explore the properties of a novel interconnected suspension configuration, which could potentially improve suspension performance. The expectation was that the increase in roll stiffness without the accompanying increase in twist stiffness should theoretically offer an improvement in tire grip and less comfort penalty. However, the results do not reach the expectation.

Based on the results in the linear analysis, it appears that the interconnected suspension offers only a small performance advantage compared to the other configurations. By increasing the roll stiffness, the interconnected suspension can provide reduced roll motion with less comfort penalty when compared with the anti-roll bar model. However, the advantage disappears at high frequency, indicating that the interconnected suspension might be more suitable in off-road style application, where the disturbance would tend to be of larger amplitude and lower frequency. Additionally, based on the contact force acting between the tire and the ground predicted by a non-linear random road simulation, there is little to distinguish the performance of the conventional, anti-roll bar and interconnected models. To explore this lack of sensitivity, a second hypothesis is put forward: the twist mode stiffness of the conventional suspension configuration is already high enough before the anti-roll bar and interconnected configurations are added to mask the effects of the interconnection.

To make this issue clear, a final experiment designed to excite only the twist mode is conducted in MotionView®. A step signal with an amplitude of 0.1 m is applied on the right front and left rear wheels in all three models. The outputs are set to be the resulting steady state vertical force between the ground and the right front wheel. The results are shown as Table 5.1.

Table 5.1: Static twist mode tire force [N]

Conventional	Anti-roll	Interconnected
2.7938×10^2	3.3327×10^2	3.0204×10^2

Based on the equation:

$$k = \frac{\Delta f}{\Delta x} \tag{5.1}$$

where k is the effective twist stiffness, Δf is the variance of vertical force and Δx is the vertical displacement, the resulting stiffness ratio is $1.08 : 1.19 : 1$ for the interconnected, anti-roll bar and conventional models, respectively. In other words, the anti-roll bar only adds about 20% to the twist mode stiffness, while interconnected suspension adds about 8%. According to the results above, the interconnected suspension does increase the roll stiffness with minimal change in twist stiffness. However, the baseline value of the twist mode stiffness is high enough that the effect of the interconnnected configuration is minimal. This explains why the difference among the results of the three configuration is so small. One can conclude that the interconnection functions as envisioned, and does offer potential improvements, but these will not be significant unless accompanied by an alternate suspension configuration that reduces the baseline twist mode stiffness.

Other secondary conclusions from the work are:

- The modal analysis results generated in the EoM software are very consistent with those generated in Altair MotionView®.
- For very smooth road inputs, non-linear effects due to suspension mechanism geometry are not significant on the SAE Baja model. A linear model returned nearly identical results to the non-linear model for a time history solution in this case. However, the conclusion does not consider non-linear damping effects, as these were not explored.

5.2 Contribution

To the best of the author's knowledge, the mechanically interconnected suspension evaluated here has never been utilized in an SAE Baja vehicle, or indeed, in any production road vehicle. It does not appear in the literature. While many interconnected suspensions have been proposed, this configuration is unique in that it offers no variations in bounce or pitch stiffness, but focuses only on roll and twist stiffness. The mechanical implementation is relatively simple when compared to other designs. Any analytical evaluation of the design is a contribution to the body of knowledge on suspension design. Aside from the analytical models, the mechanical design shows that this configuration can fit in the small Baja off-road vehicle well, and could be a suitable choice, particularly given the primarily low frequency benefits that would be valuable in an off-road setting. Finally, the thesis offers

a substantial comparison between the results obtained from linear and nonlinear vehicle simulations that can offer experience and lessons for other researchers in the future.

5.3 Recommendations

Numerous uncertainties still exist and are avenues for future study.

- In the Altair MotionView® models in this work, the stiffness between the tire and the ground is set at the center of the tire instead of the ground, to avoid the unexpected vehicle 'rolling-down' motion. A more sophisticated tire contact model may alleviate this issue.
- Because of the missing tangent stiffness matrix, the linear simulation in Altair MotionView® does not consider the gravity effects. It is uncertain if this effect is significant.
- In the interconnected configuration, ground clearance may become an issue; the size of the bell-crank should be considered to avoid collision with the ground. The weight of the links and anti-roll bar could be included in a more elaborate vehicle model to explore their effect.
- More details of the vehicle model could be considered, especially in the non-linear region, such as a non-linear tire model, or non-linear damper model.
- Although the multibody solver used to generate the solution of the equations of motion is widely used in industry, and there is a high degree of confidence in its correctness and validity, experimental data to validate the multibody model would be interesting.
- The hydraulic and pneumatic suspension coupling might offer a better choice to improve the interconnected suspension. Alternate coupling designs could be investigated.
- At last, the interconnected structure no doubt adds complexity, and some small additional weight that should to be considered in the overall evaluation.

In summary, this thesis has presented an innovative suspension configuration for an off-road vehicle A thorough analytic study to predict its efficacy has been conducted. While the mechanical interconnection has been designed successfully and, to some extent, can increase the roll stiffness with less comfort penalty than a conventional anti-roll bar, several issues remain and further investigation is needed before the recommendation can be made to implement this design.

References

[1] Reza N. Jazar, 'Vehicle Dynamics: Theory and Applications', *Springer-Verlag New York, New York, USA, 2 edition.*, pp. 497, 2014.

[2] M. C. Smith. and G. W. Walker, 'Interconnected vehicle suspension', *Journal of Automobile Engineering*, 2005.

[3] Julian Edgar, Examining the natural frequencies of suspension pitch and roll. Retrieved from http://www.autospeed.com, 2012

[4] William D Allison, US Patent US3419101A. Washington, DC: U.S, 1968

[5] J. B. Hawley Jr, US Patent US1647518A. Washington, DC: U.S, 1927

[6] Wade A Smith, 'Recent developments in passive interconnected vehicle suspension', *Article in Frontiers of Mechanical Engineering in China*, 2009.

[7] Erik Zapletal, 'Balanced Suspension', *SAE Technical Paper 2000-01-3572*, 2000.

[8] Nong Zhang, Lifu Wang, Guangzhong Xu and Holger Roser, 'Experimental comparison of anti-roll bar with hydraulic interconnected suspension in articulation mode', *SAE International*, 2013.

[9] Basileios Mavroudakis and Peter Eberhard, 'Mode decoupling in vehicle suspensions applied to race cars', *III European Conference on Computational Mechanics: Solids, Structures and Coupled Problems in Engineering. Lisbon*, 2006.

[10] Wade A. Smith, Jeku Jeyakumaran, Nong Zhang, 'Hydraulically interconnected vehicle suspension: background and modelling', *Special Issue: Selected Papers from the 22nd International Congress of Theoretical and Applied Mechanics*, 2010.

[11] S. Rakheja, C.Y. Su, D. Cao, 'Roll and pitch-plane coupled hydro-pneumatic suspension', *Vehicle System Dynamics*, 2010.

[12] A.E. Moulton, 'Hydragas suspension', *SAE Paper SAE-790374*, 1979.

[13] Steven M. Karamihas, Michael W. Sayers, 'The little book of profiling', *Transportation Research Institute, University of Michigan*, pp. 1–2, 1998.

[14] J. Dixon, 'Suspension geometry and computation' John Wiley and Sons Ltd, pp. 65–82, 2009.

[15] B.R Devis, 'Power spectral density of road profile', *Vehicle System Dynamics*, 2001.

[16] Feng Tyan, Yu-Fen Hong, R.O.C. Shun, Wes S. Jeng, 'Generation of random road profile', *Journal of Advanced Engineering* , 2009.

[17] Yucheng Liu, 'Constructing equations of motion for a vehicle rigid body model', *SAE International Journal of Passenger Cars-Mechanical Systems*, 2008.

[18] Jun Feng, Xinjie Zhang, Konghui Guo, Fangwu Ma, Hamid Reza Karimi, 'A frequency compensation algorithm of four-wheel coherence random road', *Mathematical Problems in Engineering 2013*, 2013.

[19] Daniele Ardiri, Alessandro Cammarata, Rosario Sinatra, 'Simulation of roller test bench for fatigue validation of a scooter frame', *Italy: Piaggio Brand Unit Vehicle Mechanical System & CAE*, 2014

[20] B.P. Minaker, X. Yang, S. Li, 'Design optimazation of an SAE Baja vehicle using the EoM open source multibody dynamics code', *Processing of the Canadian Society for Mechanical Engineering International Congress*, 2014.

[21] B.P. Minaker, 'The tangent stiffness matrix in rigid multibody vehicle dynamics', *Mathematical and Computer Modelling of Dynamical Systems*,21:288–310, 2015.

[22] J.R. Ellis, 'Vehicle Dynamics, Business Book Limited', *London, UK*, 1969.

[23] Stephen L.Campbell, Vu Hoang Linh, Linda R. Petzold, 'Differential-algebraic equations', *Scholarpedia*, 2008.

[24] Charles Sullivan, 'Linearization of nonlinear systems, with fluid system examples', *Linearization and nonlinear fluid elements* , 2004.

Appendix A

A.1 MATLAB® Codes of Random Road

```
function z=road(varargin)
% class is an integer from 3 - 9, where class=3 is an A-B road (smooth), class=9 is G-H road (
    rough)
if(nargin==1)
        class=varargin{1};
else
        class=3;
end

if(class<3)
        class=3;
end

if(class>9)
        class=9;
end

global h;
global x;
global v;
v=5;    % forward speed [m/s], assume constant;
L=100;    % max wavelength [m], also equals road length
B=v/512;    % sampling distance, capture at 512 Hz
deltan=1/L    % frequency interval
N=L/B    % number of samples
x=0:B:L;    % road coordinate
n=(deltan:deltan:N*deltan);    % frequency span
n(1)    % max spatial frequency
n(N)
phi=rand(1,N)*2*pi; % random phase lag for each frequency
a=sqrt(deltan)*(2^class)*1e-3*(0.1./n); % amplitude of each frequency, based on psd content
```

```
a(1)
a(N)

h=zeros(size(x)); % road vertical

for i=1:length(n) % sum for each frequency included
        h=h+a(i)*cos(2*pi*n(i)*x+phi(i));
end

figure(1)
plot(x,h);
xlabel('Road Vertical Location [m]');
ylabel('Location [m]');

% compute the psd of the random road
% should be a straight line in log space, down to wl_min

sf=1/B;      % sampling frequency
N=length(x);     % number of samples
xdft=fft(h);     % fast Fourier transform
xdft=xdft(1:N/2+1);      % take only half results (symmetric)
psdx=(1/(sf*N))*abs(xdft).^2;    % compute power
psdx(2:end-1)=2*psdx(2:end-1);    % other half
freq=0:sf/N:sf/2;     % compute frequencies
wl=1./freq;  % compute wavelengths
figure(2)
loglog(freq,psdx)
xlabel('Freq [cycles/m]')
ylabel('Power/Frequency [dB m/cycle]')
```

A.2 MATLAB® Codes of Power Spectral Density

```
load tireforce.dat
fs=100
T=1/fs
time=tireforce(:,1)
chassis=tireforce(:,2)
plot(time,chassis)
title('time history response');
xlabel('Time (s)');
ylabel('force')
nfft=501
X=fft(chassis)
p2=abs(X/nfft)
p1=p2(1:nfft/2+1)
p1(2:end-1)=2*p1(2:end-1)
f=(0:nfft/2)*fs/nfft;
figure
semilogx(f,p1)
title('frequency history response');
xlabel('frequency(Hz)');
ylabel('power')
X=X(1:nfft/2+1)
psd=(1/(fs*nfft))*abs(X).^2
psd(2:end-1)=2*psd(2:end-1)
freq=0:fs/nfft:fs/2
figure
loglog(freq,psd)
title('Power spectral density');
xlabel('frequency(Hz)');
ylabel('power/frequency(dB/Hz)')
q=trapz(freq,psd)
hold on
```

Appendix B

B.1 Frequency Domain Analysis

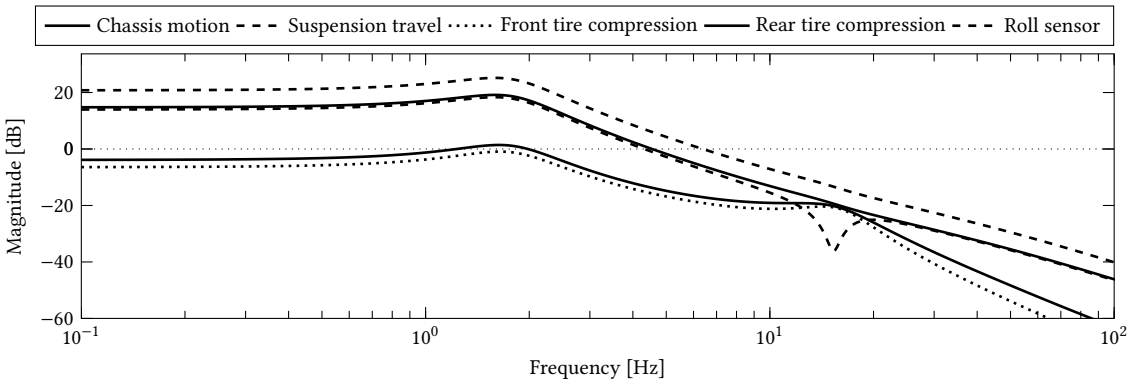

Figure B.1: Frequency response of conventional suspension to the roll moment

B.2 The Eigenvalues in Altair MotionView®

Table B.1: Modal analysis of conventional configuration

No.	Real [Hz]	Imaginary [Hz]	Natural Frequency	Damping Ratio
1	0.0000×10^{0}	0.0000×10^{0}	0.0000×10^{0}	1.0000×10^{0}
2	0.0000×10^{0}	0.0000×10^{0}	0.0000×10^{0}	1.0000×10^{0}
3	6.8435×10^{-17}	0.0000×10^{0}	0.0000×10^{0}	1.0000×10^{0}
4	8.3515×10^{-14}	0.0000×10^{0}	0.0000×10^{0}	1.0000×10^{0}
5	-3.8764×10^{-13}	0.0000×10^{0}	3.8764×10^{-13}	1.0000×10^{0}
6	-4.6024×10^{-8}	0.0000×10^{0}	4.6024×10^{-8}	1.0000×10^{0}
7	4.6025×10^{-8}	0.0000×10^{0}	0.0000×10^{0}	1.0000×10^{0}
8	-2.6402×10^{1}	0.0000×10^{0}	2.6402×10^{1}	1.0000×10^{0}
9	-4.2732×10^{1}	0.0000×10^{0}	4.2732×10^{1}	1.0000×10^{0}
10	-2.1747×10^{2}	0.0000×10^{0}	2.1747×10^{2}	1.0000×10^{0}
11	-2.2408×10^{2}	0.0000×10^{0}	2.2408×10^{2}	1.0000×10^{0}
12	-2.3104×10^{2}	0.0000×10^{0}	2.3104×10^{2}	1.0000×10^{0}
13	-5.5474×10^{-1}	1.5064×10^{0}	1.6053×10^{0}	3.4557×10^{-1}
13	-5.5474×10^{-1}	-1.5064×10^{0}	1.6053×10^{0}	3.4557×10^{-1}
14	-4.2951×10^{-1}	1.6533×10^{0}	1.7082×10^{0}	2.5144×10^{-1}
14	-4.2951×10^{-1}	-1.6533×10^{0}	1.7082×10^{0}	2.5144×10^{-1}
15	-8.8951×10^{-1}	2.2825×10^{0}	2.4497×10^{0}	3.6312×10^{-1}
15	-8.8951×10^{-1}	-2.2825×10^{0}	2.4497×10^{0}	3.6312×10^{-1}
16	-2.2463×10^{0}	1.3675×10^{1}	1.3858×10^{1}	1.6209×10^{-1}
16	-2.2463×10^{0}	-1.3675×10^{1}	1.3858×10^{1}	1.6209×10^{-1}
17	-5.0626×10^{0}	1.4290×10^{1}	1.5160×10^{1}	3.3394×10^{-1}
17	-5.0626×10^{0}	-1.4290×10^{1}	1.5160×10^{1}	3.3394×10^{-1}
18	-3.7569×10^{0}	1.5146×10^{1}	1.5605×10^{1}	2.4075×10^{-1}
18	-3.7569×10^{0}	-1.5146×10^{1}	1.5605×10^{1}	2.4075×10^{-1}
19	-3.7016×10^{0}	1.5517×10^{1}	1.5952×10^{1}	2.3204×10^{-1}
19	-3.7016×10^{0}	-1.5517×10^{1}	1.5952×10^{1}	2.3204×10^{-1}

Note: oscillatory roots appear as complex conjugates.

Table B.2: Modal analysis of anti-roll bar configuration

No.	Real [Hz]	Imaginary [Hz]	Natural Frequency	Damping Ratio
1	0.0000×10^{0}	0.0000×10^{0}	0.0000×10^{0}	1.0000×10^{0}
2	0.0000×10^{0}	0.0000×10^{0}	0.0000×10^{0}	1.0000×10^{0}
3	5.7819×10^{-16}	0.0000×10^{0}	0.0000×10^{0}	1.0000×10^{0}
4	-6.5442×10^{-15}	0.0000×10^{0}	6.5442×10^{-15}	1.0000×10^{0}
5	-8.0860×10^{-13}	0.0000×10^{0}	8.0860×10^{-13}	1.0000×10^{0}
6	-1.8606×10^{-7}	0.0000×10^{0}	1.8606×10^{-7}	1.0000×10^{0}
7	1.8606×10^{-7}	0.0000×10^{0}	0.0000×10^{0}	1.0000×10^{0}
8	-2.6374×10^{1}	0.0000×10^{0}	2.6374×10^{1}	1.0000×10^{0}
9	-4.2534×10^{1}	0.0000×10^{0}	4.2534×10^{1}	1.0000×10^{0}
10	-2.1747×10^{2}	0.0000×10^{0}	2.1747×10^{2}	1.0000×10^{0}
11	-2.2407×10^{2}	0.0000×10^{0}	2.2407×10^{2}	1.0000×10^{0}
12	-2.3101×10^{2}	0.0000×10^{0}	2.3101×10^{2}	1.0000×10^{0}
13	-4.2896×10^{-1}	1.6523×10^{0}	1.7071×10^{0}	2.5128×10^{-1}
13	-4.2896×10^{-1}	-1.6523×10^{0}	1.7071×10^{0}	2.5128×10^{-1}
14	-5.5435×10^{-1}	1.8496×10^{0}	1.9309×10^{0}	2.8710×10^{-1}
14	-5.5435×10^{-1}	-1.8496×10^{0}	1.9309×10^{0}	2.8710×10^{-1}
15	-8.8788×10^{-1}	2.2807×10^{0}	2.4475×10^{0}	3.6277×10^{-1}
15	-8.8788×10^{-1}	-2.2807×10^{0}	2.4475×10^{0}	3.6277×10^{-1}
16	-2.2460×10^{0}	1.3675×10^{1}	1.3858×10^{1}	1.6208×10^{-1}
16	-2.2460×10^{0}	-1.3675×10^{1}	1.3858×10^{1}	1.6208×10^{-1}
17	-5.0417×10^{0}	1.4287×10^{1}	1.5150×10^{1}	3.3278×10^{-1}
17	-5.0417×10^{0}	-1.4287×10^{1}	1.5150×10^{1}	3.3278×10^{-1}
18	-3.7573×10^{0}	1.5147×10^{1}	1.5606×10^{1}	2.4076×10^{-1}
18	-3.7573×10^{0}	-1.5147×10^{1}	1.5606×10^{1}	2.4076×10^{-1}
19	-3.7653×10^{0}	1.6160×10^{1}	1.6593×10^{1}	2.2692×10^{-1}
19	-3.7653×10^{0}	-1.6160×10^{1}	1.6593×10^{1}	2.2692×10^{-1}

Note: oscillatory roots appear as complex conjugates.

Table B.3: Modal analysis of interconnected configuration

No.	Real [Hz]	Imaginary [Hz]	Natural Frequency	Damping Ratio
1	0.0000×10^{0}	0.0000×10^{0}	0.0000×10^{0}	1.0000×10^{0}
2	0.0000×10^{0}	0.0000×10^{0}	0.0000×10^{0}	1.0000×10^{0}
3	-1.9333×10^{-15}	0.0000×10^{0}	1.9333×10^{-15}	1.0000×10^{0}
4	5.4739×10^{-15}	0.0000×10^{0}	0.0000×10^{0}	1.0000×10^{0}
5	2.4160×10^{-14}	0.0000×10^{0}	0.0000×10^{0}	1.0000×10^{0}
6	1.9383×10^{-7}	0.0000×10^{0}	0.0000×10^{0}	1.0000×10^{0}
7	-1.9383×10^{-7}	0.0000×10^{0}	1.9383×10^{-7}	1.0000×10^{0}
8	-2.6364×10^{1}	0.0000×10^{0}	2.6364×10^{1}	1.0000×10^{0}
9	-4.2436×10^{1}	0.0000×10^{0}	4.2436×10^{1}	1.0000×10^{0}
10	-2.1747×10^{2}	0.0000×10^{0}	2.1747×10^{2}	1.0000×10^{0}
11	-2.2407×10^{2}	0.0000×10^{0}	2.2407×10^{2}	1.0000×10^{0}
12	-2.3099×10^{2}	0.0000×10^{0}	2.3099×10^{2}	1.0000×10^{0}
13	-4.2842×10^{-1}	1.6513×10^{0}	1.7060×10^{0}	2.5113×10^{-1}
13	-4.2842×10^{-1}	-1.6513×10^{0}	1.7060×10^{0}	2.5113×10^{-1}
14	-5.4674×10^{-1}	1.9197×10^{0}	1.9960×10^{0}	2.7392×10^{-1}
14	-5.4674×10^{-1}	-1.9197×10^{0}	1.9960×10^{0}	2.7392×10^{-1}
15	-8.8799×10^{-1}	2.2809×10^{0}	2.4476×10^{0}	3.6279×10^{-1}
15	-8.8799×10^{-1}	-2.2809×10^{0}	2.4476×10^{0}	3.6279×10^{-1}
16	-2.2451×10^{0}	1.3672×10^{1}	1.3856×10^{1}	1.6204×10^{-1}
16	-2.2451×10^{0}	-1.3672×10^{1}	1.3856×10^{1}	1.6204×10^{-1}
17	-5.0951×10^{0}	1.4335×10^{1}	1.5214×10^{1}	3.3490×10^{-1}
17	-5.0951×10^{0}	-1.4335×10^{1}	1.5214×10^{1}	3.3490×10^{-1}
18	-3.7572×10^{0}	1.5147×10^{1}	1.5606×10^{1}	2.4075×10^{-1}
18	-3.7572×10^{0}	-1.5147×10^{1}	1.5606×10^{1}	2.4075×10^{-1}
19	-3.7267×10^{0}	1.5888×10^{1}	1.6320×10^{1}	2.2836×10^{-1}
19	-3.7267×10^{0}	-1.5888×10^{1}	1.6320×10^{1}	2.2836×10^{-1}

Note: oscillatory roots appear as complex conjugates.

B.3 The Integration of Power Spectral Density

Table B.4: Integration of PSD for the three configurations in different random roads

Level	Conventional	Anti-roll	Interconnected
3	1.2799×10^{-1}	1.2797×10^{-1}	1.2797×10^{-1}
4	1.3542×10^{-1}	1.3538×10^{-1}	1.3540×10^{-1}
5	1.3107×10^{-1}	1.3103×10^{-1}	1.3105×10^{-1}
6	1.4105×10^{-1}	1.4095×10^{-1}	1.4103×10^{-1}

Appendix C

C.1 EoM Item Type List and Description

Body A rigid body. The properties include name, location of the center of mass, mass, moment of inertia and cross products of inertia. All other items must be connected to a body, and the ground body is predefined.

Spring A two point elastic spring of which the properties include the location of each end, the names of the two bodies to which it is attached, stiffness, damping and inertance values. Models a tension spring by default, but if the spring is a torsional spring, the 'twist' field to can be set to 1. Known preloads can be set in indeterminate systems if desired, but otherwise the preload will be computed by EoM.

Link Similar to a spring, but not extensible. Preload depends on external loads, and cannot be specified.

Rigid_point A generic constraint. The properties include the number of forces that are carried, and the number of moments, the location, and the names of the two bodies to which it is attached. Acceptable choices for the number of forces and moments is 0, 1, 2, or 3. If 1 force or moment is applied, the 'axis' field defines the direction of the force and/or moment, for 2 forces or moments, the axis defines the normal to the plane in which the forces or moments lie. For 0 or 3 forces or moments, no axis field is required.

Flex_point A single point spring with translational and rotational stiffness and damping. The flex_point can be used to model bushings. The properties include the location, the names of the two bodies to which it is attached, the number of forces and moments passed, the axis, and the linear and torsional stiffness, and linear and torsional damping.

Beam A massless beam spring, where the area moments of inertia in both bending directions are the same and there is no cross product of area. It has bending and shear stiffness, but no tension or torsion. The properties include the location of each end, the names of two bodies to which it is attached, and the stiffness value; no damping is defined.

Load Constant forces and moments applied to the system. It is used to determine preloads in the connecting elements, and eventually to find the tangent stiffness matrix.

Actuator A linear actuator. The force is determined from an input. The properties includes location of each end, name of the two bodies to which it is attached, and the gain. By setting the 'twist' field to 1, the actuator can be turned to a torsional type.

Sensor A linear sensor that determines the outputs of a linear system. The properties include the location of each end, name of the two bodies to which it is attached, and the gain. It can measure position, velocity or acceleration, and the reference frame may be set to measure local rather than global velocities.

Vita Auctoris

Zheng Yao was born in Qingdao, Shandong, China in 1990. He graduated from Qingdao No. 2 High School in 2008. He then attended the Shandong University of Technology, where he earned a Bachelor's Degree of Instrument Control and Measurement in 2012. He obtained his Master of Engineering degree at the University of Windsor in 2014 and since that time, he worked under Dr. Minaker. He is presently a candidate for the Master of Applied Science in Mechanical Engineering degree at the University of Windsor, and is scheduled to graduate in December, 2016.